Development and application of *ab initio* methods for the study of electronic excitations in molecules and extended solids: GW approximation and constrained DFT

Miguel Angel Pérez Osorio

Tesi Doctoral

Ciència de Materials

Directors

Dr. Miguel Alonso Pruneda i Prof. Pablo Ordejón Rontomé

Departament de Química

Facultat de Ciències

2012

Acknowledgements

This thesis was supported by MICINN, project FIS2009-12721-C04. I thank Spanish Council for Scientific Research for the Jae-Pre093 grant to support my PhD. studies.

I would like to express my gratitude to my supervisors, Dr. Miguel Alonso Pruneda and Professor Pablo Ordejón Rontomé, for providing me with guidance and support during the last four years. I greatly appreciated their understanding, expertise, and tremendous patience, especially during the first year of my doctorate.

This thesis was developed at the Research Center on Nanoscience and Nanotechnology CIN2(CSIC-ICN) under the supervision of Dr. Miguel Alonso Pruneda and Professor Pablo Ordejón Rontomé.

Resumen

El objetivo principal de esta tesis fue la implementación dentro del código SIESTA de dos métodos de primeros principios para el estudio de excitaciones electrónicas en moléculas y sólidos extendidos. Los métodos son la aproximación GW y el 'constrained' DFT. Los métodos fueron implementados usando bases de orbitales extrictamente localizados generadas por SIESTA. El uso de este tipo de orbitales abre la posibilidad de estudiar sistemas que contienen miles de átomos.

La aproximación GW es un método derivado de la teoría de perturbaciones de muchos cuerpos para la funcin de Green de una partícula, que se usa para el cálculo de las energías de excitación de quasipartículas. En este trabajo, se implementó el método propuesto por F. Giustino et al. [3], que solo requiere el uso de los estados electrónicos ocupados para calcular los ingredientes de esta aproximación: la función de Green y el potencial de Coulomb apantallado.

En método de 'constrained' DFT se impone una ligadura sobre la densidad electrnica del sistema a través de un potencial apropiado. En esta tesis se implementó una versión modificada de la aproximación propuesta por Q. Wu and T. Van Voorhis [4] para encontrar el potencial de 'constraining' de manera eficiente. El método se extendió para el caso de sistemas periódicos. Como una aplicación del método, se estudiaron procesos de transferencia de carga en el conductor oránico TTF-TCNQ.

Una aplicación interesante de los métodos implementados es el estudio de los procesos electrónicos que tienen lugar en las celdas solares y dispositivos fotovoltaicos. El material ms ampliamente usado en la fabriacin de estos dispositivos es el TiO_2 en fase anatase dopada con impurezas de nitrógeno o sensibilizada con colorantes orgánicos. Como un paso previo al estudio de las excitaciones electrnicas de este material, se caracterizaron sus propiedades electrónicas, estructurales,

termodinámicas y vibracionales usando la teoría DFT. Además, se estudiaroon las energías 'binding' de los niveles de core de las diferentes especies químicas.

Abstract

The main aim of this thesis is the implementation in the SIESTA code (a widely used academic computational program based on the density functional theory DFT for the simulation of materials) [1, 2] of two powerful methods for the study of electronic excitations in molecules and extended solids. The methods are the so-called constrained density functional theory (CDFT) and the GW approximation and they are implemented within the strictly localized orbital formalism as defined in SIESTA. The use of local bases opens the possibility of calculating electronic excitations in systems containing thousands of atoms.

The GW approximation is a powerful method derived from many-body perturbation theory for the one-particle Green function to calculate quasiparticle excitation energies. We implement the approach proposed by F. Giustino et al. [3] that only requires the use of the occupied electronic states to compute the Green function and screened Coulomb interaction, and from which one constructs the self-energy operator, Σ. In this approach, the Green function is approximated to that of a non-interacting electron system and calculated using a inhomogeneous linear system, while the dynamically screened potential is calculated through the self-consistent linear-response Sternheimer equation. Since the original equations were stated within the plane waves formalism, here we rewrite these equations for basis sets of strictly localized orbitals. As an application of our approach for the dynamically screened potential, we calculate the dielectric function of several insulating and semiconducting materials: LiCl, diamond, silicon and germanium, comparing our results with plane-waves calculations.

In the constrained density functional theory, we impose a constraint upon the electronic density of a system through an appropriate potential (called constraining potential) to obtain a neutral excitation. We implement a modified version of the approach proposed by Q. Wu and T. Van Voorhis [4, 5, 6] to find the constraining potential efficiently. Moreover, we extend the method for the case of periodic solids. As an application of our CDFT method, we study the charge transfer between the TTF and TCNQ molecules in the TTF-TCNQ conducting organic salt, where it has been suggested from XPS experiments that the charge transfer process is dynamic, leading to the coexistence of TTF^{0}-$TCNQ^{0}$ and TTF^{1+}-$TCNQ^{1-}$ charge states [7, 8].

An interesting potential application of our implemented methods is the study of electronic excitations in semiconductor-based solar cells and photovoltaic devices to the efficient design and fabrication of such devices [9, 10, 11]. One of the most extensively used materials for the fabrication of these devices is the anatase TiO_2 whether doped with nitrogen impurities or sensitized with dye molecules. Using the DFT machinery we characterize this material as the first step before the calculation of their electronic excitations. We study native defects: oxygen vacancies and interstitial titanium, and nitrogen impurities at interstitial or substitutional position in the anatase matrix. The electronic, structural and thermodynamic properties of all these point defects with different charge states were calculated. Moreover, we study the lattice dynamic of defective anatase in order to determine how defects affect the vibrational modes of pristine anatase and what are the new features arising from defects. We calculate the binding energy shifts of the N 1s, O 1s and Ti 3p core levels to contribute to the full characterization of the defects. Our results of lattice dynamic and core level binding energy shifts are compared with experimental data from Raman and XPS spectroscopy, respectively.

Contents

List of Figures

Chapter 1

Introduction

In the last decades, the simulation of electronic excitations using first-principles computational methods has been one of the most attractive challenges in the field of condensed matter physics. In particular, optical spectra and photoemission processes, both in extended solids and in nanoscale systems, are the subject of widespread interest, due to the need for accurate tools to help understand and predict the experimental properties. In Quantum Chemistry, there is a plethora of well developed methods to compute electronic excitations, based on approximations to the many-body wave function [13]. However, these methods are too demanding computationally for systems with a large number of atoms, like in most problems of interest in nanoscience, and they are typically not feasible for the study of solids. These systems are only accessible to methods with a low computational workload, such as Density Functional Theory (DFT), which is by far the most widely used method for the simulation of materials and nanoscale systems. However, in principle DFT theory can only describe the properties related to the electronic ground state, such as the total energy and charge density, and the structural properties, such as the lattice parameters of the equilibrium crystal structure, elastic constants and vibrational modes. Excited electronic states are not accessible to DFT (except for a limited number of cases, such as first ionization potentials and electron affinities [14], and the lowest lying excitations with different spin symmetry than the ground state [15]). Being a ground state theory, there is no theoretical justification for the use of DFT to calculate excitations energies. However, although the Kohn-Sham orbitals and their eigenvalues are

only a mathematical tool to obtain the total ground-state energy of a system and do not have any physical meaning, they are often identified with the electronic excitations and used to construct the band structure and to estimate the band gap. This procedure typically leads to a serious underestimation of the band gap when compared with the experimental results, as it is shown in the Fig 1.1. As an example, the band gap of silicon using the local density approximation (LDA) is 0.63 eV smaller than the experimental value of 1.1 eV, while for GaAs there is a difference of 1.1 eV between theory and experiment.

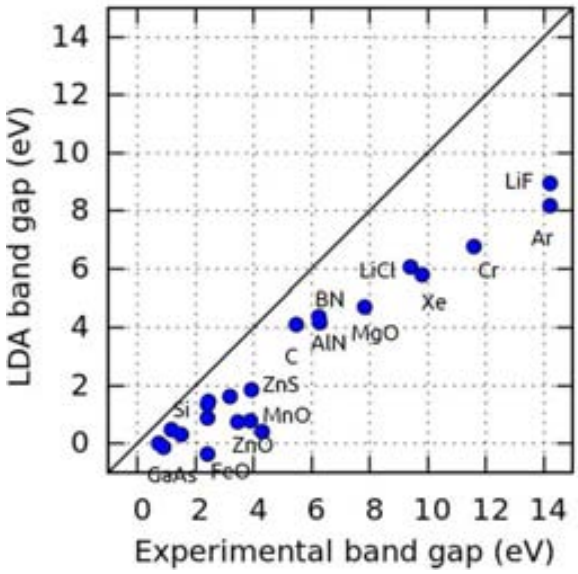

Figure 1.1: Band gaps of semiconductors and insulators from experiment and theory (LDA) [12].

Describing properly electronic excitations is computationally demanding. The increased computational resources and the development of new methods in the last two decades have enabled to do it. One of the earliest methods proposed to calculate the whole spectrum of excitation energies of a finite system, based on density functional theory, was the time-depending DFT (TDDFT) [16]. This method relies on the one-to-one mapping between the time-dependent density and the external potential. Even using the crude adiabatic local density approximation (ALDA) where the ground-state time-independent exchange correlation

functional is used in place of the time-dependent exchange correlation action, TDDFT calculations give excitation energies that in general agree well with experiments. In the context of time-independent DFT, we have the constrained-DFT (CDFT) method where, instead of calculating the whole set of excitations energies, one aims at the estimation of a particular excitation for which information on the electronic distribution is known a priori. The excitation energy (the difference between the total energy of the excited and ground state) is then obtained from the ground-state energy of the system with the appropriate constraint on its density. This is done, in practice, by making an appropriate choice of the external potential which leads to the desired constrained density distribution as its ground state. Various strategies have been proposed to find the constraint potential. Brute-force scanning on the potential until finding the value that satisfies the constraint density is one of the strategies to follow, but this technique is computationally inefficient and difficult in system with many independent constraints. Q. Wu and T. Van Voorhis [4, 5] have proposed an efficient method to study finite systems with a constraint on their density, using the Lagrange multipliers approach. This method has been applied successfully to the study of charge transfer (CT) processes in organic and organometallic molecules, also including long-range CT for which ALDA fails because of the local approximation in the exchange-correlation kernel [17]. In this thesis a modified version of this method was implemented and extended to periodic systems.

The GW approximation has emerged as one of the most powerful approaches for describing quasiparticles energies in a great variety of systems, including extended solids and nanoscaled systems, and is also a suitable starting point for Bethe-Salpeter calculations of two-particle neutral excitations, with a wide range of applications, such as the calculation of optical response of nanostructures, quantum transport in nanoscale junctions, pump-probe spectroscopy, and some strongly correlated systems. The GW approximation has proven to be successful in describing and predicting experimental photoemission and optical spectra with a remarkable accuracy. The band gaps of the majority of semiconductor crystals for which DFT fails are in good agreement with experimental values. The GW approximation is derived systematically from many-body perturbation theory. The method was first introduced by L. Hedin with his work on the electron-gas

problem in 1965 [18]. He established the fundamentals of the method showing in a systematic and rigorous way how the self-energy can be expanded in powers of the dynamically screened Coulomb interaction, with the main ingredient of the GW approximation being the first term of such a expansion. However, due to computational limitations, the application of the GW method in real materials was not possible until 1986, when M. S. Hybertsen and G. Louie published the application of the GW approximation on semiconductor materials with encouraging results [19]. Since then, many efforts have focused to the implementation of the method with plane waves or local bases, and to enhance its efficiency. On the other hand, the number of publications on the application of the method in a great variety a problems has increased considerably. Furthermore, the GW approximation is a powerful first-principles method as it is reasonably accurate, parameter-free, consistent across materials, not material-specific and a starting point for ab-initio optics. The majority of the GW implementations are based on a perturbative expansion based on Kohn-Sham orbitals, as we will see later. In the original equations of the method, all unoccupied and occupied electronic states are required to evaluated the self-energy operator Σ, which is the main ingredient of this approximation. Σ is constructed from the Green function and the screened Coulomb interaction. The drawback of using all the electronic states is that the convergence of quasiparticle excitation energies with the number of unoccupied states is rather slow. Hence, in the last years many efforts have been addressed to explore alternative solutions to the use of unoccupied electronic states. In the present thesis, we show the most recent progresses of the implementation of the GW approximation in the SIESTA code using an efficient method proposed by F. Giustino et al. [3], which only requires the use of occupied electronic states. This work is being done as a part of an intensive collaboration between our group lead by Prof. P. Ordejón and the group of Prof. F. Giustino at University of Oxford. Both CDFT and GW approximation are powerful methods for the efficient design and fabrication of photovoltaic devices and solar cells based on semiconductor materials, as these methods can be used for the rationalization and understanding of the electronic processes occurring at nanoscale. The material most extensively used for the fabrication of such devices is the titanium dioxide anatase (from now we call it anatase for simplicity) due to its interesting chemical and

physical properties. This materials is also applied in the degradation of organic molecules because of its interesting photocatalytic properties. The main drawback of anatase that limits its efficiency in all the applications previously mentioned is its band gap that falls in the ultraviolet region of the electromagnetic spectrum. To narrow its band gap two approaches has been explored in the last two decades, 1) doping the material with nonmetallic impurities like nitrogen and fluorine, and 2) sensitizing its surface with dye molecules. In the former approach, it has been experimentally found that doping the material with nitrogen results in a enhancement of the photocatalytic properties of the material under solar radiation. This effect is attributed to the reduction of the band gap by the nitrogen impurities, however, the experimental characterization of the nitrogen impurities is not straightforward. Hence, there is still questions related with the role that the nitrogen impurities play in the reduction of the band gap. For instance, there is no a consensus among experimentalist concerning the assignment of the different XPS peaks observed in the N 1s signal of N-doped anatase. One of the factor that contribute to this situation in that the features observed in the XPS spectra depend on the preparation method. New features are also observed in the Raman spectrum of N-doped anatase. Guillaume et al. have observed a shift of the lowest frequency Raman active phonon mode when nitrogen in implanted in the anatase matrix by pulsed laser deposition (PLD), however, there is not information about the role of the nitrogen impurities or native defects in this phenomenon. As a preliminary step to the study of electronic excitations of the N-doped anatase, in this thesis we proceed to characterize the electronic, structural and dynamical properties and the core level binding energies of the anatase with nitrogen impurities and native defects using the DFT machinery. We compare our results with experimental data.

This thesis is organized as follows. In the chapter 2 we give a brief background on the density functional theory as the final equations of both CDFT and GW approximation are evaluated using Kohn-Sham orbitals. We also show the main features of the SIESTA code, focusing on how SIESTA uses localized orbitals. The chapters 3 and 4 are devoted to present the CDFT and GW approximation methods, respectively, including their representation within the localized orbital formalism. In the chapter 5 we present a theoretical study of the N-doped anatase

using the DFT theory as implemented in the SIESTA code. We compare our results with experimental data. Finally, the chapter 6 is devoted for conclusions and final remarks.

General goals

The main aims of this thesis are:

- To implement two *ab initio* methods for the study of electronic excitations in molecules and extended solids in the SIESTA code using strictly localized orbitals. These methods are the so-called GW approximation and the constrained density functional theory.
- To apply these methods to the study of the dielectric properties of insulating and semiconducting materials calculated from the screened Coulomb potential, and the study of excited electronic states of the TTF-TCNQ organic semiconductor material using the constrained DFT.
- To study the electronic, structural and thermodynamic properties and core level binding energy shifts of point defects in TiO_2 anatase, and compare our results with experimental data.

Chapter 2

Background

2.1 Density Functional Theory (DFT)

The study of the electronic properties of molecules and solids from theory has been one of the most extensively explored topics in condensed matter since the birth of the quantum theory. The starting equation for calculating electronic properties is the time-independent Schrödinger equation, whose simplest form is given by

$$\hat{H}\Psi = E\Psi \tag{2.1}$$

Here, $\hat{H}$ is the Hamiltonian operator for a system of electrons and nuclei, $\Psi(\mathbf{r}_i, \mathbf{R}_I)$ is an eigenstate that depends on both electron and nuclei positions, $\mathbf{r}_i$ and $\mathbf{R}_I$, respectively (from now on, lower case indices run over electrons and upper case indices over ions), and E is the corresponding eigenvalue (energy of the state). The Hamiltonian operator has the form [20]:

$$\hat{H} = -\frac{\hbar}{2m_e}\sum_i \nabla_i^2 - \sum_I \frac{\hbar^2}{2M_I}\nabla_I^2 - \sum_{i,I}\frac{Z_I e^2}{|r_i - R_I|} + \frac{1}{2}\sum_{i\neq j}\frac{e^2}{|r_i - r_j|} + \frac{1}{2}\sum_{I\neq J}\frac{Z_I Z_J e^2}{|R_I - R_J|} \tag{2.2}$$

where the first term is the kinetic energy operator of the electrons, the second term is the kinetic energy operator of the nuclei with mass M_I and charge Z_I, and the last three terms describe the Coulomb interactions between electrons and nuclei, i.e., electron-nucleus, electron-electron and nucleus-nucleus, respectively.

In what follows, we adopt the Born-Oppenheimer approximation, which establishes that one can represent each wave function $\Psi(\mathbf{r}, \mathbf{R})$ as a product of a nuclear wave function $\chi(\mathbf{R})$ and an electron wave function $\psi(\mathbf{r}, \mathbf{R})$ that depends parametrically on the nuclear positions. Since the velocity of electrons is larger in comparison with the nucleus velocity, their motions can be separated and one can solve Ψ assuming $\mathbf{R}$ fixed (which is the adiabatic approximation). Additionally, we make a classical approximation to the ionic dynamics assuming that they follow Newton's equations of motion. In that case, one obtains a Schrödinger equation for the wave functions of the electrons, which reads:

$$[\hat{T}_e + \hat{V}_{ext} + \hat{V}_{int} + E_{II}]\psi(\mathbf{r}, \mathbf{R}) = E\psi(\mathbf{r}, \mathbf{R}). \tag{2.3}$$

Here, $\hat{T}_e$ is the kinetic energy of the electrons. The interaction between electrons and ions (third term in the r.h.s. of Eq. 2.2) is denoted as $\hat{V}_{ext}$, since the ions can now be considered as an external potential for the electrons. Other external potentials (electric and magnetic fields, etc.), can be added to $\hat{V}_{ext}$. The electron-electron interaction (forth term in the r.h.s. of Eq. 2.2 is denoted as $\hat{V}_{int}$. E_{II} is the (classical) Coulomb interaction between nuclei, and is a constant for fixed nuclear positions. Using the Dirac notation, the expression of the total energy E as the expectation value of the time-independent Hamiltonian operator defined as $\hat{H} = \hat{T}_e + \hat{V}_{ext} + \hat{V}_{int} + E_{II}$ is

$$E = \frac{\langle\psi|\hat{H}|\psi\rangle}{\langle\psi|\psi\rangle} = \langle\hat{H}\rangle = \langle\hat{T}_e\rangle + \int d\mathbf{r} V_{ext}(\mathbf{r}) n(\mathbf{r}) + \langle\hat{V}_{int}\rangle + E_{II} \tag{2.4}$$

where $n(\mathbf{r}) = |\psi(\mathbf{r}, \mathbf{R})|^2$ is the electronic density.

Solving Eq. 2.3 has been a major problem in condensed matter physics for calculating both ground-state electronic properties and electronic excitations. However, two critical problems arise when solving this equation for relative large systems. First, the many-body wave functions depend on a very large number of spatial variables, $3N_e$, which quickly results in a high demand of computational resources. The second problem is the appropriate description of the electron-electron Coulomb interaction term. Several methods have been developed using different approaches to describe the electron-electron interaction and many-body

wave functions. One of the earliest methods proposed for studying relative small systems was the Hartree-Fock approximation, where the many-body wave function is approximated by a Slater determinant [21] made from spin-dependent single-particle wave functions. In this approach the electron-electron interaction is described through the Hartree and exchange potentials. The Hartree potential (the classical Coulomb potential of the charge density) is local, while the exchange potential is non-local. The minimization of the resulting Schrödinger equation with respect to the single-particle states, under the orthonormality condition, yields a set of single-particle equations, which must be solved self-consistently because the Hartree and exchange potential depend on the contraventions.
All electron-electron interactions beyond the Hartree-Fock approximation are referred to as correlation. The correlation energy can be obtained by means of improving systematically the approximation of the many-body wave function beyond the single Slater determinant. The Configuration Interaction (CI) method [22] is the limit of that systematic expansion, in which the many-body wave function is described as a complete linear combination of Slater determinants. However, this method scales faster than exponentially with system size, so that applications to large molecules or solids are not feasible.

Kohn-Sham method

One of the first attempts to introduce the effects of the interaction between electrons in a simpler way to study large systems was made by Slater with his X_α method [23, 24]. In this method, the exchange potential is modelled by a local potential of the form $V_x = \alpha n^{1/3}$ (with n being the electronic density of the system) and scaled by a constant α to simulate the correlation effects. Although the X_α method is semi-empirical, it was the initial seed of the density functional theory (DFT), a first-principles method derived from the many-body theory for the charge density that incorporates exchange and correlation effects among the electrons. The original formulation of the method is due to P. Hohenberg and W. Kohn [25, 26]. They proved that ground-state energy of an interacting-N-electron system obeying the Hamiltonian 2.3 is a unique functional of electronic

density n and that the external potential V_{ext} of the system is uniquely determined by the ground state density. They showed that the ground-state energy can be obtained by minimizing the energy functional with respect to the electronic density. Therefore, to obtain the ground-state energy it is not necessary to know the many-body wave function: the knowledge of the electron density is sufficient. This is an enormous advantage, since the density is a much less complicated object than the wave function (it depends only on three variables, instead of $3N_e$).

In 1965 Kohn and Sham [20, 27] proposed an approach to obtain the ground-state total energy of the interacting many-body system obeying the Hamiltonian 2.3 within the DFT, that consists in using a fictitious system of non-interacting particles (more easily to solve) with the same ground state density than the interacting many-body system. This leads to independent-particle equations for the non-interacting system that can be considered exactly soluble with all the difficult many-body terms incorporated into an exchange-correlation functional of the density, whose exact form is unknown. By solving the equations one finds the ground state density and energy of the original interacting system with the accuracy limited only by the approximations in the exchange-correlation functional.

The Kohn-Sham energy functional is defined as

$$E_{KS} = T_s[n] + \int d\mathbf{r} V_{ext}(\mathbf{r}) n(\mathbf{r}) + E_{Hartree}[n] + E_{II} + E_{xc}[n] \tag{2.5}$$

where n is the electronic density of the system, T_s the independent-particle kinetic energy, V_{ext} the external potential, $E_{Hartree}$ the Hartree electron-electron interaction energy, E_{II} the nucleus-nucleus interaction energy, and E_{xc} denoting all effects beyond independent-particle kinetic energy and Hartree approximation. Thus, E_{xc} is defined as

$$E_{xc}[n] = \langle \hat{T}_e \rangle - T_s[n] + \langle \hat{V}_{int} \rangle - E_{Hartree}[n] \tag{2.6}$$

The electronic density of an non-interacting system is given by the sum of squares of the single-electron wave functions for each spin σ,

$$n(\mathbf{r}) = \sum_{\sigma} \sum_{i=1}^{N^{\sigma}} |\psi_i^{\sigma}(\mathbf{r})|^2 \tag{2.7}$$

The solution for the ground state energy of the auxiliary system is obtained by minimizing Eq. 2.6 with respect to the single-electron wave functions (subject to the orthonormality condition) as they are the basic ingredient of electronic density, leading to the Kohn-Sham Schrödinger-like equations:

$$H_{KS}^{\sigma}\psi_i^{\sigma}(\mathbf{r}) = \varepsilon_i^{\sigma}\psi_i^{\sigma}(\mathbf{r}) \tag{2.8}$$

where ε_i are the eigenvalues, and H_{KS} is the effective Hamiltonian (in atomic units)

$$H_{KS}^{\sigma}(\mathbf{r}) = -\frac{1}{2}\nabla^2 + V_{KS}^{\sigma}(\mathbf{r}) \tag{2.9}$$

with

$$V_{KS}^{\sigma}(\mathbf{r}) = V_{ext}(\mathbf{r}) + V_{Hartree}[n(\mathbf{r})] + V_{xc}^{\sigma}[n(\mathbf{r})] \tag{2.10}$$

with $V_{Hartree}$ and V_{xc} being the Hartree potential and the exchange-correlation potential, respectively. V_{KS}^{σ} is the effective potential that describes the independent particle system with the same electron density as the real interacting-particle system. The Kohn-Sham equations must be solved self-consistently with the resulting electronic density, Eq. 2.7, leading to the Kohn-Sham total energy E_{KS}, Eq. 2.6. Since no approximation is used in the derivation of the Kohn-Sham equations, one could access to the exact ground state density and total energy for the interacting system if the exact functional $E_{xc}[n]$ was known. Unfortunately, we have to approximate the $E_{xc}[n]$ functional, being a critical ingredient in the Kohn-Sham theory.

Exchange-correlation potential $\mathbf{V}_{xc}$

The most common approximations for the exchange-correlation functional are the local density approximation (LDA) and the generalized gradient approximations

(GGAs) [28]. In the former one, the exchange-correlation energy depends solely on the value of electronic density at each point in space and is given by

$$E_{xc}^{LDA}[n] = \int n(\mathbf{r})\epsilon_{xc}(n(\mathbf{r}))d\mathbf{r} \tag{2.11}$$

where $\epsilon_{xc}(n)$ is the exchange-correlation energy per particle of a uniform electron gas of density n. Although one could think that this functional is only accurate for systems with a nearly uniform electronic density, it has proved to be successful in describing systems with large variations in the electronic density. In the GGAs, the exchange-correlation functional includes the gradient of the density as well as the value of the density at each point. A simple representation of this functional is

$$E_{xc}^{GGA}[n] = \int n(\mathbf{r})\epsilon_{xc}(n(\mathbf{r}), \nabla n(\mathbf{r}))d\mathbf{r} \tag{2.12}$$

Among the most common GGA parametrizations we find PW91 (proposed by Perdew, Burke and Wang [28]) and PBE (proposed by Perdew, Burke and Enzerhof [29]).

Basis

Usually the Kohn-Sham single-particle wave functions ψ_i are expanded as a combination of basis functions ϕ_μ

$$\psi_i(\mathbf{r}) = \sum_\mu c_{i\mu}\phi_\mu(\mathbf{r}) \tag{2.13}$$

where the basis functions can be defined in many ways, with plane waves and atomic-like orbitals (including functions such as Slater-type orbitals, Gaussian, Bessels or strictly localized atomic orbitals) as the most common choices. Consequently, the problem of solving the Schrödinger equation for the wave functions becomes a tractable problem of solving linear equations for the coefficients c. By projecting the basis function ϕ_μ on both sides of Eq. 2.8 we obtain the linear

equation system in matrix representation

$$[\mathbf{H} - \varepsilon\mathbf{S}]\mathbf{c} = 0 \tag{2.14}$$

where the elements of the Kohn-Sham Hamiltonian $\mathbf{H}$ and overlap $\mathbf{S}$ are defined as

$$H_{\mu\nu} = \langle\phi_\mu|H|\phi_\nu\rangle \tag{2.15}$$

$$S_{\mu\nu} = \langle\phi_\mu|\phi_\nu\rangle \tag{2.16}$$

and $\mathbf{c}$ is the coefficient vector. The electronic density in the local basis is given by

$$n(\mathbf{r}) = \sum_{\mu\nu} \rho_{\mu\nu}\phi_\mu(\mathbf{r})\phi^*_\nu(\mathbf{r}) \tag{2.17}$$

with $\rho_{\mu\nu} = \sum_i^{occ} c_{i\mu}c^*_{i\nu}$. By solving the determinant of Eq. 2.14 we get the eigenvalues ε that are then used to obtain the coefficients of the wave functions. Since SIESTA uses strictly localized numerical atomic orbitals as basis set, in the next section we focus on describing the main features of this kind of orbitals and on how SIESTA generates them. Then, we discuss the concept and use of pseudopotentials (also used by SIESTA) because it allows to get rid of the core electrons as they are essentially inert.

2.2 Local basis sets

In SIESTA, the expansion of the KS wave functions with a basis set is performed as a linear combination of atomic orbitals (LCAO) [1]. The use of local bases allows some of the operations involved in DFT calculations to scale linearly with the number of atoms in the system because the Hamiltonian, overlap and density matrices have a sparse form due to the locality of the orbitals. It allows to use efficient computational techniques to store and process the matrices in such a way that the zero matrix elements are not required explicitly, reducing considerably the memory and CPU requirements. This is the main advantage of the local orbitals against plane waves. However, using strictly localized orbitals has a cost. The optimization of the local basis is not systematic as in the case of plane waves.

In spite of this, an efficient optimization of the local basis can yield results that have the plane waves accuracy.

For efficiency, the most important aspects to consider are the number of basis orbitals per atom, the range of localization of such orbitals and their shape [1, 30, 31]. The strictly localized numerical atomic orbitals used by SIESTA are constructed as products of a numerical radial function, that is strictly zero beyond a certain radius (cutoff radius), and a spherical harmonic

$$\phi_{Ilmn}(\mathbf{r}) = \phi_{Iln}(r_I) Y_{lm}(\hat{\mathbf{r}}_I) \tag{2.18}$$

with $\mathbf{r}_I = \mathbf{r} - \mathbf{R}_I$. Here $\mathbf{R}_I$ stands for the position of the atom I. l and m indicate the angular quantum numbers, which may be arbitrarily large, and determine the type of orbital, whether s, px, py, pz... The index n denotes the principal quantum number. Additionally, one can construct several orbitals with the same angular momentum but with different radial functions. The possibility of describing the local orbitals with a variety of both angular and radial functions makes them very versatile.

Thus, one can construct bases with different sizes depending on the number of radial functions used for each angular momentum of the valence orbitals of the atoms in the system. The minimal basis, which is called single-ζ, contains one radial function for each angular momentum. Subsequent bases are constructed using two or more radial functions with the same angular momentum and called multiple-ζ bases, namely double-ζ, triple-ζ and so on. These radial functions are constructed with the split-norm procedure [32]. Such procedure consists of supplementing each basis orbital, for instance each single-ζ of the minimal basis, $\phi_l^{1\zeta}(r)$, with a new basis function $\phi_l^{2\zeta}(r)$ that reproduces exactly the tail of the original basis orbital from a given matching radius r_m outwards. The inner part goes smoothly towards the origin as $r^l(a_l - b_l r^2)$, where a and b are chosen to ensure continuity of the function and its derivative at r_m. The radius r_m is set by fixing the norm of the original orbital, being usually of 0.15. The second-ζ is then defined as $\phi_l^{1\zeta} - \phi_l^{2\zeta}$. The next radial functions are constructed in the same way. This split-norm construction guarantees that the additional ζ's exhibit a smaller cutoff radius with reference to original radius, keeping the energy strictly varia-

tional. Also, one can include polarization orbitals that are the perturbed atomic orbitals of the isolated-atom Hamiltonian for the orbital with angular momentum l (so that $l+1$ is not a valence orbital) when this Hamiltonian is in presence of a small electric field. In such case, we name it as polarized multiple-ζ basis.
To build a minimal basis set, SIESTA calculates the radial function for each angular momentum ϕ_l by numerically solving the Kohn-Sham Hamiltonian (including the pseudopotential $V_l(r)$) of a isolated pseudo-atom within a spherical box confined by a potential $V(r)$. In SIESTA, two kind of potential $V(r)$ can be used. One of them has the following form

$$V(r) = V_o \frac{e^{-\frac{r_c - r_i}{r - r_i}}}{r_c - r} \tag{2.19}$$

where the parameters V_o, r_c and r_i are the amplitude of the confining potential, the cutoff radius and the width of the cutting function, respectively. The parameters of the confining potential must be specified for any calculation. Such potential, which was proposed by Junquera et al. [31], guarantees a continuous derivative of the radial function at the cutoff radius. Using this potential, the KS Hamiltonian of the isolated atom looks like

$$(-\frac{1}{2r}\frac{d^2}{dr^2}r + \frac{l(l+1)}{2r^2} + V_l(r) + V(r))\phi_l(r) = \varepsilon_l \phi_l(r) \tag{2.20}$$

and it is solved to obtain the radial wave function ϕ_l and eigenvalues ε_l of the isolated pseudo-atom. The other potential $V(r)$ is the hard-confinement potential proposed by Sankey et al. [33], $V(r) = 0$ for $r < r_c$ and ∞ for $r > r_c$. If this potential is used, SIESTA defines ε_l as $\varepsilon_l + \delta\varepsilon_l$ and we have to specify the value of $\delta\varepsilon_l$ for any calculation. Then, the Eq. 2.20 is solved to obtain the radial wave function ϕ_l and its cutoff radius. Using this potential we control the cutoff radius for each of the orbitals of each species in a consistent manner by specifying a single parameter, the so-called "energy-shift" $\delta\varepsilon_l$ [1]. The use of this confinement potential is particularly useful when we study convergence of electronic properties with basis orbitals because we reduce the number of parameters.

2.3 Pseudopotentials

The basic idea behind pseudopotentials is describing the strong Coulomb potential of the nucleus along with the screening effects of the core electrons as an effective ionic potential acting on the valence electrons. This procedure is valid since core states are associated to deep energy levels, so that they are chemical inert. The use of pseudopotentials reduces the cost of a DFT calculation because basis functions are not required to describe core states, and because the valence pseudo-wave functions are much smoother than the true wave functions (since they do not need to be orthogonal to the core wave functions, thus eliminating the rapidly varying node structure near the core). Appropriate first-principle pseudopotentials are generated form an all-electron calculation, usually with a semilocal or nonlocal form. In both cases, one computes a pseudopotential for each angular momentum l of the valence electrons. A semilocal pseudopotential is the sum over angular momenta l of products between a radial component $V_l(r)$ (which is local, but angular-momentum dependent) and an angular (nonlocal) component $\hat{P}_l$ (which is just the projector on the angular momentum l),

$$\hat{V}^{PS}_{semilocal} = \sum_l V^l_{ps} \hat{P}_l, \tag{2.21}$$

whereas a nonlocal pseudopotential is the sum of a radial component, which is local and behaves as Z_v/r for $r \to \infty$, and angular components, which are nonlocal and different for each lm,

$$\hat{V}^{PS}_{nonlocal} = V_{local}(\mathbf{r}) + \sum_{lm} D_l |\beta_{lm}\rangle\langle\beta_{lm}| = V_{local}(\mathbf{r}) + \sum_{lm} \hat{V}^{KB}_{lm} \tag{2.22}$$

In this case, $|\beta_{lm}\rangle\langle\beta_{lm}|$ are the so-called Kleinman-Bylander projectors. The basic principles in the construction of pseudopotentials are well established. However, with the objective of producing pseudopotentials with improved transferability and computational efficiency, several schemes have been proposed in the past. In this sense, norm-conserving pseudopotentials developed by Hamann et al. [34] satisfy normalization condition and are suitable for transferability, which allow accurate self-consistency calculations. This kind of pseudopotentials is constructed

satisfying the following conditions:

- Real and pseudo valence eigenvalues are equal for a chosen reference atomic configuration.
- Real and pseudo atomic wave functions agree beyond a chosen core radius r_c.
- The integrals from 0 to r of the real and pseudo charge densities agree for $r > r_c$ for each valence state (norm conservation).
- The logarithmic derivatives of the real and pseudo wave function and their first energy derivatives agree for $r > r_c$.

SIESTA uses norm-conserving pseudopotentials, generated by the atomic program ATOM in a semilocal form. Although several types of pseudopotentials can be used, the prescription proposed by Troullier and Martins [35] is typically used to optimize smoothness. Then, SIESTA transforms this semilocal form into a fully nonlocal form proposed by Kleinman-Bylander [36]. Thus, the Kohn-Sham Hamiltonian transforms into,

$$H^{\sigma}_{KS}(\mathbf{r}) = -\frac{1}{2}\nabla^2 + V_{local}(\mathbf{r}) + \sum_{lm} \hat{V}^{KB}_{lm} + V_{Hartree}[n(\mathbf{r})] + V^{\sigma}_{xc}[n(\mathbf{r})] \qquad (2.23)$$

2.4 SIESTA Tools

2.4.1 Lattice dynamics

The phonon modes are calculated using the force constant matrix obtained with the finite differences method [1, 20]. Using the force constant matrix, a secular equation is solved to get the normal mode frequencies ω and eigenvectors v. Formally, the elements of the force constant matrix are the variation in the force on the atom I caused by an infinitesimal displacements of the atom J

$$C_{IJ} = -\frac{dF_I}{dR_J} = \frac{d^2E}{dR_I dR_J} \qquad (2.24)$$

where the force in the atom I is defined as

$$F_I = -\frac{dE}{dR_I} \tag{2.25}$$

with E being the total energy around the equilibrium configuration of the atomic positions. The forces on the atoms for a given configuration can be obtained through the well-known Hellmann-Feynman theorem, which establishes that the force on a nucleus depends upon the electronic density $n(\mathbf{r})$ as

$$\mathbf{F}_I = -\frac{\partial E}{\partial \mathbf{R}_I} = -\int d^3r n(\mathbf{r}) \frac{\partial V_{ext}(\mathbf{r})}{\partial \mathbf{R}_I} - \frac{\partial E_{II}}{\partial \mathbf{R}_I} \tag{2.26}$$

where V_{ext} and E_{II} are the external potential and interaction between nuclei, respectively.

In SIESTA, the forces are calculated by direct differentiation of the expression for the Kohn-Sham total energy with respect to atomic positions, including the Pulay corrections [37, 38]. Once the forces are obtained, the elements of the force constant matrix are calculated by performing the numerical derivative of Eq. (2.24),

$$C_{I,\alpha;J\beta} \approx -\frac{\Delta F_{I,\alpha}}{\Delta \mathbf{R}_{J,\beta}} \tag{2.27}$$

where α and β stand to indicate the cartesian components of the force and displacement. In general, this direct approach for the force constant matrix allows quantitative calculations without requiring additional computational algorithms. The phonon frequencies are determined by solving the secular equation

$$det|\frac{1}{\sqrt{M_I M_J}} C_{I,\alpha;J,\beta} - \omega^2| = 0 \tag{2.28}$$

which is derived within the harmonic approximation. In this equation M_I is the mass of the atoms and ω is the vibrational frequency.

In polar materials, such as anatase, the force constant matrix needs a special treatment due to the long range dipole-dipole interactions between the ionic effective charges, which yields a LO-TO splitting of the IR active modes. The polarization caused by the effective charges leads to non-analytic terms in the

force constant matrix, which has the form

$$C_{s,\alpha;s',\alpha'}(\mathbf{k}) = C^N_{s,\alpha;s',\alpha'}(\mathbf{k}) + \frac{4\pi e^2}{\Omega}\left[\sum_\gamma \mathbf{k}_\gamma \hat{Z}^*_{I,\gamma\alpha}\right]^t \frac{1}{\epsilon(\mathbf{k})}\left[\sum_\gamma \hat{\mathbf{k}}_\gamma Z^*_{I,\gamma\beta}\right] \tag{2.29}$$

where C^N is the normal analytic part of C and $\epsilon(\mathbf{k})$ is the low-frequency electronic dielectric constant. $Z^*_{I,\alpha\beta}$ is a component of the Born effective charge tensor, which can be calculated using the finite difference method as in the case of the force constant matrix:

$$Z^*_{I,\alpha\beta}|e| = \frac{\Delta\mathbf{P}_\alpha}{\Delta\mathbf{R}_{I,\beta}} \tag{2.30}$$

where $\Delta\mathbf{P}_\alpha$ is the variation in the macroscopic polarization along the α direction due to a displacement $\Delta\mathbf{R}_{I,\beta}$ of the atom I in the direction β. In SIESTA the macroscopic polarization for periodic systems is calculated using the geometric Berry phase approach.

2.4.2 Core level binding energy (CLBE)

The x-ray photoemission spectroscopy is a experimental technique used for the characterization of the chemical species of materials. It measures core level binding energies (CLBE) of the different atoms in the sample. In this technique the specimen under study is irradiated with a monochromatic beam of X-rays with energy $h\nu$. Due to the high energy of the incident radiation, it can eject electrons of core levels of the atoms in the specimen, ionizing them. A portion of the photoemitted electrons is collected by a detector where their kinetic energy E_{kin} is measured. Considering that energy is conserved in the whole process, the total energy of the system before and after electron photoemission is written as

$$E_{ground}(A) + h\nu = E_{ionized}(A^+) + E_{kin} + e\phi_{detector} \tag{2.31}$$

where $E_{ground}(A)$ is the total energy of the sample before an electron is photoemitted, $E_{ionized}(A^+)$ is the total energy of the system with the atom A ionized, and $e\phi_{detector}$ is the potential energy of the electron at the detector (with $\phi_{detector}$ being the work function of the detector, i.e., the potential difference between the

Fermi level and the vacuum potential at the detector). Thus, CLBE is defined as the difference between the ionized and ground state energy.

$$BE = E_{ionized}(A^{+}) - E_{ground}(A) \tag{2.32}$$

Substituting this equation into Eq. (2.31), we can see that BE of core electrons is accessible through measured quantities.

$$BE = h\nu - E_{kin} - e\phi_{detector} \tag{2.33}$$

$h\nu$ is a known initial parameter as well as $e\phi_{detector}$ once the equipment is calibrated. The kinetic energy of the photoemitted electrons is measured by a detector. Since the binding energies are strongly determined by the environment around the atoms: bonds, spatial configuration and neighbouring atoms, the XPS spectra are used as "fingerprints" for local bond configuration of atoms in the material.

To contribute to the understanding and description of experimental XPS spectra of N-doped anatase, we calculate binding energies of the O 1s, N 1s and Ti 2p core levels from first principles using two approximations: the so-called initial state and the ΔSCF approximation, as implemented in the SIESTA code by S. García et al. [39]. However, we can not obtain absolute binding energies directly, since both initial and ΔSCF approximation use pseudopotentials. Hence, in both approximations we calculate the binding energies of a given core level for two atoms of the same specie with different environments. If we consider the binding energy of one of the atoms as the reference (BE_{ref}), then the CLBE shift for the atom of our interest (having a binding energy BE_A) with respect to the reference will be

$$\Delta(BE) = BE - BE_{ref} \tag{2.34}$$

In the following lines we describe briefly the main theoretical basis behind these approximations.

Initial state approximation

In this approximation any relaxation effect on the valence states of the system caused by the core hole created after electron emission, is neglected. Thus, the binding energy will be the energy required to remove the core electron, which is bound by the potential of the system in the core region. This energy is just minus the energy of the core level, $-\varepsilon_l^m$, which is estimated using first-order of perturbation theory from the all-electron core level wave functions ψ_n^{lm} obtained from an all-electron calculation and the potential $V(\mathbf{r})$ obtained in a pseudopotential calculation of the system (neglecting spin-orbit interactions), as

$$\varepsilon_l^m = \langle \psi_l^{m,AE}(\mathbf{r}) | V(\mathbf{r}) | \psi_l^{m,AE}(\mathbf{r}) \rangle \tag{2.35}$$

Although the total potential from pseudopotentials does not have the atomic component $1/r$ near the nuclei of the true all-electron potential, this deficiency does not affect the final result as this contribution is very local and cancels out when differences in energy between the system under study and the reference system.
Thus, the shift within the initial approximation is given by

$$\Delta(BE)_{init} = -\left(\langle \psi_l^{AE,m}(\mathbf{r}) | V(\mathbf{r}) | \psi_l^{AE,m}(\mathbf{r}) \rangle - \langle \psi_l^{AE,m}(\mathbf{r}) | V_{ref}(\mathbf{r}) | \psi_l^{AE,m}(\mathbf{r}) \rangle \right) \tag{2.36}$$

We can simply write,

$$\Delta(BE)_{init} = -(\varepsilon - \varepsilon^{ref}) \tag{2.37}$$

where we omit the quantum number indexes for simplicity.

ΔSCF approximation

The ΔSCF approximation lies on the assumption that the photoemission process is slower than the response of valence electrons to the presence of the created core hole. This assumption implies that all effects on the BE due to charge rearrangements must be included. To do that, S. García et al. follow the procedure described in [40]. They calculate the difference between the total energy of a given system with a hole core in the atom A, $E(A^+)$ and the total energy of the

ground state, E_0

$$BE_{\Delta SCF} = E(A^+) - E_0 \tag{2.38}$$

Here, $E(A^+)$ includes all effects due to electronic relaxations. In this approximation, one assumes there is no geometry changes due to the ionization. As in the initial state approximation, we calculate the binding energies of a given core level in two atoms of the same type under different environments, one of which is taken as the reference. Thus, the shift is given by

$$\Delta(BE)_{\Delta SCF} = [E(A^+) - E_0] - [E(A^+) - E_0]_{ref} \tag{2.39}$$

In SIESTA, to calculate the total energy of the system with the ionized atom, we have to generate a pseudopotential for the ionized atom with a hole in the core level we want to study. This is done using a new feature of the ATOM program. When SIESTA reads the pseudopotential for the ionized atom, it computes the local part as $(Z_v + 1)/r$ since one electrons has been removed. SIESTA does not include explicitly the local part of the pseudopotentials (that in the general case is Z_v/r) in the Kohn-Sham Hamiltonian because of its long-range character. Instead of that SIESTA introduces it implicitly through a short-range term, where the local part of the pseudopotential is screened by a potential behaving as $-Z_v/r$. Hence, we have to ensure that the local part of the pseudopotential for the ionized atom (where an electron has been removed) is screened correctly with a potential $(Z_v + 1)/r$. For a better understanding of how we introduce implicitly the local part of the pseudopotential, let us write the Hamiltonian used by SIESTA,

$$H = T + \delta V^H(\mathbf{r}) + V_{xc}(\mathbf{r}) + \sum_I V_I^{NA}(\mathbf{r}) + \sum_I V_I^{nl} \tag{2.40}$$

Here, T is the kinetic energy operator, δV^H is the Hartree potential term that contains the difference between the potential V^H generated by self-consistency charge density $\rho^{SCF}(\mathbf{r})$ and the potential V_I defined below, V_{xc} the exchange and correlation potential, V_I^{NA} is the neutral atom potential, which is the local part of the pseudopotential V_I^{local} screened by a charge distribution V_I (which has the same behaviour than the local potential but with opposite sign, $-Z_v/r$ and whose

integral is equal to the valence charge of the atom I), that is,

$$\sum_I V_I^{NA} = \sum_I V_I^{local} + \sum_I V_I \tag{2.41}$$

V^{NA} is strictly localized, being zero beyond a certain cutoff radius. Finally, V_I^{nl} the non local part of the pseudopotential with I being the atom index. The last two terms are of short range.

To ensure that SIESTA computes a neutral atom potential strictly localized for the atom with the core hole, one has to add an extra valence electron into this atom. This is done by defining a new $Z+1$ chemical species in the input file of SIESTA. It makes the calculated energy not to be equal to $E(A^+)$, because the simulation cell has one more electron that is at the Fermi level of the system. The calculated energy is thus $E^{Z+1}(A^+) = E(A^+) + \varepsilon_F$. Consequently, Eq. 2.39 transforms into

$$\Delta(BE)_{\Delta SCF} = [E^{Z+1}(A^+) - \varepsilon_F - E_0] - [E^{Z+1}(A^+) - \varepsilon_F - E_0]_{ref} \tag{2.42}$$

The extra electron should be removed from the system or not depending on the considered material. In the case of insulating systems and molecules in gas phase, since there are no available electrons to screen the core hole, the extra electron should be removed by imposing a net charge of +1.0 on the system. For metals, an electron coming from the bulk of the sample screens the core hole, therefore the extra electron should be left.

The reference level problem

To compare core level binding energies shifts obtained from theory with experimental XPS data, we have to use the same reference potential than in the experiments. This issue can be overcome in several ways depending on if the material is metallic, semiconductor or insulator.

For metallic samples, in the XPS experiment the detector is connected to the metallic sample and the ground, such that the Fermi energy levels of the different

connected parts align yielding a common Fermi energy level, which is measured through the work function of the detector $\phi_{detector}$ and used as the reference potential. Hence, combining Eqs. 2.33 and 2.34 the experimental core level binding energy shift in metals is given by

$$\Delta(h'\nu') = (h'\nu') - (h'\nu')^{ref} = -BE + BE^{ref} = -\Delta(BE) \tag{2.43}$$

Theoretically, in the initial approximation we align the Fermi energy levels of the reference ε_F^{ref} and the sample ε_F by inserting them into the Eq. 2.33, leading to

$$\Delta(BE)_F^{init} = -(\varepsilon - \varepsilon_F) + (\varepsilon - \varepsilon_F)^{ref} \tag{2.44}$$

This equation is applicable for the general case where the sample and reference are computed using different cells. For the metallic systems we study in this thesis, we calculate core level binding energy shifts for different and inequivalent atoms contained in the same cells, which means that ε_F^{ref} and ε_F have the same value. Therefore, Eq. 2.44 becomes

$$\Delta(BE)_F^{init} = -\varepsilon + \varepsilon^{ref}. \tag{2.45}$$

In the ΔSCF approximation, it is easy to see that Eq. 2.42 transforms into

$$\Delta(BE)_{\Delta SCF}^{F} = [E^{Z+1}(A^+) - E_0] - [E^{Z+1}(A^+) - E_0]_{ref} \tag{2.46}$$

where the calculation is reduced to the determination of the total energy of the sample and reference systems without a net charge: the system before the ionization (E_0), and the system after the core hole is created and an extra electron is added (E^{Z+1}). As we study systems with the reference and sample atom being in the same cell, the Eq. 2.46 is further reduced to

$$\Delta(BE)_{\Delta SCF}^{F} = E^{Z+1}(A^+) - E^{Z+1}(A^+)_{ref} \tag{2.47}$$

On the other hand, for semiconductor and insulator periodic systems, we can not use the Fermi level as reference potential, because experimentally it is not easy to determine it [39]. In the calculation, we have a similar problem since it can be

laid anywhere in the gap and hence is "ill-defined".
Considering we calculate CLBE for different and inequivalent atoms contained in the same cell (if other thing is done it will be specified), the reference potential is always the same (whichever it is) and therefore it cancels itself if we perform a CLBE shift. As a consequence, Eqs. 2.37 and 2.39 are valid to determine the CLBE shifts within the initial and ΔSCF approximation, respectively. Moreover, Eq. 2.39 is reduced to a simpler expression because the terms E_0 and E_0^{ref} are the same.

Chapter 3

GW approximation

3.1 Introduction

Electronic excitations in molecules and solids are experimentally measured by experimental techniques such as photoemission, optical absorption and electron-energy loss spectroscopies. The electronic properties that can be obtained from them are band gaps, density of states and absorption and optical spectra. They all are essential in the characterization and further applications of the materials. Among the theoretical methods developed for the study of electronic excitations in molecules and extended solids, the GW approximation and Bethe-Salpeter equation have emerged as the state-of-the-art first-principles computational methods [3, 41, 42, 43, 44]. They allow us to compute quasiparticle energies and two-particles excitations. They can reproduce and predict experimental data with remarkable accuracy.

To determine the band gap of a finite system containing N electrons, one performs direct and inverse photoemission experiments to measure the ionization potential and the electron affinity, respectively. The band gap is then defined as the difference between the electron affinity and ionization potential. To be more specific, in the direct photoemission the system is irradiated with a light beam with energy $\hbar\omega$ along a certain direction $\mathbf{k}$, so that an electron is ejected with energy E_{kin} from the system (leaving it with $N-1$ particles) to the vacuum. Considering that the ejected electron is completely decoupled from the system,

the total energy and momentum before and after the direct photoemission process are the same as they satisfy the energy and momentum conservation laws. Thus, the energy conservation equation is

$$E(N) + \hbar\omega = E(N-1) + E_{kin} \tag{3.1}$$

where $E(N)$ and $E(N-1)$ indicate the total energy of the system with N and $N-1$ particles, respectively. From this equation, the ionization potential (IP) is defined as

$$IP = E(N) - E(N-1) = E_{kin} - \hbar\omega \tag{3.2}$$

It is just the energy required to remove an electron from the system to the vacuum (the lowest of which corresponds to the first ionization potential, in which the system with $N-1$ electrons is in its ground state). On the other hand, in the inverse photoemission the system with N particles is irradiated with an electron beam with kinetic energy E_{kin} at certain momentum $\mathbf{k}$, such that an electron falls into an unoccupied electronic state of the system, emitting a photon $\hbar\omega$. As in the previous case, due to the energy conservation law the whole photoemission process satisfies the following equation

$$E(N) + E_{kin} = E(N+1) - \hbar\omega \tag{3.3}$$

where $E(N+1)$ is the total energy of the system with $N+1$ particles. Then, we define the electron affinity (EA) as

$$EA = E(N+1) - E(N) = E_{kin} + \hbar\omega \tag{3.4}$$

It gives the energy gained by a system when an electron is incorporated from the vacuum. Using Eqs. 3.2 and 3.3, we can write the band gap energy in terms of the total energies of the system with $N(\pm 1)$ particles,

$$\varepsilon_{gap} = (E_{N+1} - E_N) - (E_N - E_{N-1}) \tag{3.5}$$

where the energies correspond to the ground state of the system with the corresponding number of electrons. Obtaining the gap energy from theory implies de-

termining the total energy of the N-particle system before and after one electron is added or removed from the system. It can be directly obtained by calculating the ground-state total energy of the system containing $N(\pm 1)$ particles, since in each calculation the electrons are allowed to be relaxed due to the addition or removal of one electron. When the energies are computed by means of an effective, selfconsistent one-electron theory (such as DFT or Hartree-Fock), this procedure is known as the delta-self-consistent-field approach. The obtained band gap ε_{gap} does not correspond to the Kohn-Sham band gap ε_{gap}^{KS} of the N-particle system, because the Koopman's theorem establishes that one-electron orbitals are frozen upon changing the number of electrons. The Kohn-Sham eigenvalues are only the mathematical tool to obtain the total energy of the system, except for the highest occupied eigenvalue, which is the first ionization potential, according to the Janak's theorem [14]. The ε_{gap}^{KS} does not include the relaxation effects of the lowest unoccupied Kohn-Sham eigenvalue arisen from addition of one electron to the system. To include these effects, we add an energy correction term Δ, which is the energy difference of the lowest unoccupied Kohn-Sham eigenvalue between the excited and the neutral state, to the Kohn-Sham gap,

$$\varepsilon_{gap} = \varepsilon_{gap}^{KS} + \Delta \tag{3.6}$$

The correction Δ is related with the discontinuity in the exchange-correlation potential that arises when there is an infinitesimal variation in the electronic charge of a system with N-particles: $\Delta = \Delta_{xc} = V_{xc}(N+1) - V_{xc}(N)$.
The calculated band gaps through either Eq. 3.5 or Eq. 3.6 are in many cases in good agreement with the experimental values for molecular systems. However, they are not appropriate in the case of extended solids, where the addition or removal of one single electron results in an infinitesimal change of the electronic charge of the unit cell. Hence, there is the need of using a different physical model derived from many-body theory that allows us to describe one-particle electronic excitations originated by the addition or removal of electrons to or from a system. In this sense, the most appropriate practical approach is the GW approximation for the one-particle Green function [18, 19, 45]. This approximation is also the starting point of Bethe-Salpeter equations for the study of two-particle excitations

to simulate optical absorption spectra.

3.2 Derivation of the Green function method

We get back to the many-body Schrödinger equation defined by Eq. 2.3 with the many-body wavefunction $\Psi(\mathbf{r}_1, ..., \mathbf{r}_N)$, expressed as

$$\left[\sum_i h(\mathbf{r}_i) + \frac{1}{2}\sum_{i\neq j} v(\mathbf{r}_i, \mathbf{r}_j)\right]\Psi = E\Psi \tag{3.7}$$

with $h(\mathbf{r}) = \hat{T}_e + V_{ext}(\mathbf{r})$, and $v(\mathbf{r}, \mathbf{r}') = \frac{1}{|\mathbf{r}-\mathbf{r}'|}$ being the bare Coulomb potential. In Eq. 3.7 we do not include the constant E_{II} for simplicity. The second quantization from of the many-body Hamiltonian in terms of field operators results in

$$H = \int d\mathbf{r}\hat{\psi}^\dagger(\mathbf{r})h(\mathbf{r})\hat{\psi}(\mathbf{r}) + \frac{1}{2}\int d\mathbf{r}d\mathbf{r}'\hat{\psi}^\dagger(\mathbf{r})\hat{\psi}^\dagger(\mathbf{r}')v(\mathbf{r}, \mathbf{r}')\hat{\psi}(\mathbf{r}')\hat{\psi}(\mathbf{r}) \tag{3.8}$$

where $\hat{\psi}^\dagger(\mathbf{r})$ and $\hat{\psi}(\mathbf{r})$ are the creation and annihilation field operators, respectively.

The many-body Schrödinger equations of the system with N($\pm$1) particles are

$$H\Psi_0^N = E_0^N\Psi_0^N \tag{3.9}$$

$$H\Psi_i^{N+1} = E_i^{N+1}\Psi_i^{N+1} \tag{3.10}$$

$$H\Psi_i^{N-1} = E_i^{N-1}\Psi_i^{N-1} \tag{3.11}$$

In this set of equations, Ψ_0^N is the groud-state many-body wavefunction of N-particle system and $\Psi_i^{N(\pm1)}$ represent the many-body wavefunction of excited state i of the system with $\pm$1 electrons. E_0^N and $E_i^{N\pm1}$ are the corresponding total energies. Solving this set of equations is precisely solving the many-body problem. We invoke the one-particle Green function, corresponding to the Hamiltonian of a N-particle system, Eq. 3.8, which describes the propagation of one electron (or one hole) in the system. The Green function contains all excited and ground state properties of the system including excitation energies, excitation lifetimes,

ground state density and expectation values of one-particle operators.
The one-particle Green function is defined as

$$G(\mathbf{r}t, \mathbf{r}'t') = -i\langle\Psi_0^N|T[\hat{\psi}(\mathbf{r}t)\hat{\psi}^\dagger(\mathbf{r}'t')]|\Psi_0^N\rangle \tag{3.12}$$

where $\mathbf{r}$ and t indicate position and time, respectively. T is the time-ordering operator and $\hat{\psi}(\mathbf{r}t)$ is the annihilation time-dependent field operator, which is defined (in the Heisemberg representation) as

$$\hat{\psi}(\mathbf{r}, t) = e^{iHt}\hat{\psi}(\mathbf{r})e^{-iHt}, \tag{3.13}$$

and similarly for the creation operator. T rearranges a series of field operators in order of ascending time arguments from right to left with a factor (-1) for each permutation.
For the propagation of one electron in a N-particle system, $t > t'$, an electron is created at $\mathbf{r}'t'$ and propagated to $\mathbf{r}t$ where it is then annihilated. The Green function describing this process is

$$G^e(\mathbf{r}t, \mathbf{r}'t') = -i\langle\Psi_0^N|\hat{\psi}(\mathbf{r}t)\hat{\psi}^\dagger(\mathbf{r}'t')|\Psi_0^N\rangle\theta(t - t') \tag{3.14}$$

where $\theta(t - t')$ is the Heaviside step function defined by

$$\theta(t - t') = \begin{cases} 1, & \text{if } t > t' \\ 0 & \text{if } t < t'. \end{cases} \tag{3.15}$$

Similarly, for the hole propagation, $t < t'$, an hole is created at $\mathbf{r}t$ and then propagated to $\mathbf{r}'t'$ where it is then annihilated

$$G^h(\mathbf{r}'t', \mathbf{r}t) = i\langle\Psi_0^N|\hat{\psi}^\dagger(\mathbf{r}'t')\hat{\psi}(\mathbf{r}t)|\Psi_0^N\rangle\theta(t' - t) \tag{3.16}$$

Thus, Green function gives the probability amplitude to detect and electron (hole) at $\mathbf{r}t$ ($\mathbf{r}'t'$) when an electron (hole) has been added to the system at $\mathbf{r}'t'$ ($\mathbf{r}t$). Since the whole Green function involves both the electron and hole propagation, we can

rewrite it as

$$G(\mathbf{r}t, \mathbf{r}'t') = G^e(\mathbf{r}t, \mathbf{r}'t') + G^h(\mathbf{r}'t', \mathbf{r}t) \tag{3.17}$$

Now, using the definition of the field operator of Eq. 3.13 and $\tau = t - t'$, the Green function adopts the form

$$\begin{aligned} G(\mathbf{r}, \mathrm{r}', \tau) = -i\langle\Psi_0^N|\hat{\psi}(\mathbf{r})e^{i(H-E_0^N)(\tau)}\hat{\psi}^\dagger(\mathbf{r}')|\Psi_0^N\rangle\theta(\tau) + \\ i\langle\Psi_0^N|\hat{\psi}^\dagger(\mathbf{r}')e^{-i(H-E_0^N)(-\tau)}\hat{\psi}(\mathbf{r})|\Psi_0^N\rangle\theta(-\tau) \end{aligned} \tag{3.18}$$

If we insert the closure relations $\sum_i |\Psi_i^{N\pm1}\rangle\langle\Psi_i^{N\pm1}| = 1$ in the middle of each term on the right side of the above equation and use the following definitions:

$$\psi_i^{N-1}(r) = \langle\Psi_i^{N-1}|\hat{\psi}(r)|\Psi_0^N\rangle \qquad \varepsilon_i^{N-1} = E_0^N - E_i^{N-1} \tag{3.19}$$

$$\psi_i^{N+1}(r) = \langle\Psi_0^N|\hat{\psi}(r)|\Psi_i^{N+1}\rangle \qquad \varepsilon_i^{N+1} = E_i^{N+1} - E_0^N, \tag{3.20}$$

where $\varepsilon_i^{N\pm1}$ are the electronic excitation energies and $\psi_i^{N\pm1}$ the amplitudes of the Green function, we get

$$\begin{aligned} G(\mathbf{r}, \mathrm{r}', \tau) = -i\sum_i \psi_i^{N+1}(\mathbf{r})\psi^{*N+1}i(\mathbf{r}')e^{-i\varepsilon_i^{N+1}(\tau)}\theta(\tau) \\ + i\sum_i \psi_i^{N-1}(\mathbf{r})\psi_i^{*N-1}(\mathbf{r}')e^{-i\varepsilon_i^{N-1}(-\tau)}\theta(\tau) \end{aligned} \tag{3.21}$$

The sums run over the ground state and all excited states of the $(N \pm 1)$-particle system, respectively. The Fourier transformation of Eq. 3.21 to the frequency domain using the Fourier transform of the Heaviside step function

$$\theta(\omega) = \frac{1}{2\pi}\int_{-\infty}^{\infty}\theta(\tau)e^{i\omega\tau-\eta|\tau|}d\tau = \frac{i}{2\pi(\omega+i\eta)} \tag{3.22}$$

yields the Lehmann representation of the Green function

$$G(\mathbf{r}, \mathbf{r}', \omega) = \sum_i \frac{\psi_i^{N+1}(\mathbf{r})\psi_i^{*N+1}(\mathbf{r}')}{\omega - \varepsilon_i^{N+1} + i\eta} + \sum_i \frac{\psi_i^{N-1}(\mathbf{r})\psi_i^{*N-1}(\mathbf{r}')}{\omega - \varepsilon_i^{N-1} - i\eta} \tag{3.23}$$

with η being a small positive number. As we can observe, the Green function has poles at the many-particle excitation energies, $\varepsilon_i^{N\pm1}$. These energies correspond to the excitations of the $(N \pm 1)$-particle system and hence to those processes measured in direct and inverse photoemission processes.
Eq. 3.5 to calculate the band gap of a finite system can be rewritten in terms of excitation energies as

$$\varepsilon^{gap} = \mathbf{min}(\varepsilon_i^{N+1}) - \mathbf{min}(\varepsilon_i^{N-1}) \tag{3.24}$$

In what follows, we omit the superscritps $N \pm 1$, rewritting the Eq. 3.23 as

$$G(\mathbf{r}, \mathbf{r}', \omega) = \sum_i \frac{\psi_i(\mathbf{r})\psi_i^*(\mathbf{r}')}{\omega - \varepsilon_i + i\eta} \tag{3.25}$$

where η is positive for the electronic excitations of $(N+1)$-particle system, and negative for the excitations of $(N-1)$-particle system.
An additional useful representation of the Green function is

$$G(\mathbf{r}, \mathbf{r}', \omega) = \int_{-\infty}^{\infty} \frac{A(\mathbf{r}, \mathbf{r}', \omega')}{\omega - \omega' + i\eta} d\omega' \tag{3.26}$$

where A is the spectral function defined as the imaginary part of the Green function, that is,

$$A(\mathbf{r}, \mathbf{r}', \omega) = \frac{1}{\pi} |\mathbf{Im} G(\mathbf{r}, \mathbf{r}', \omega)| \tag{3.27}$$

The spectral function yields the density of states of the excited states that contribute to the electron or hole propagation. For a finite system, it is represented as a sum of delta functions weighted by the products of the excitation amplitudes,

$$A(\mathbf{r}, \mathbf{r}', \omega) = \sum_i \psi_i(\mathbf{r})\psi_i^*(\mathbf{r}')\delta(\omega - \varepsilon_i) \tag{3.28}$$

When we change from a finite to an extended system, the delta functions merge and form a series of smooth peaks with finite width lines instead of delta resonances. If the resulting spectral features are of the Lorentzian form, the repre-

sentation of the spectral function is

$$A(\mathbf{r},\mathbf{r}',\omega)=\sum_i \psi_i(\mathbf{r})\psi_i^*(\mathbf{r}')\frac{\Gamma_i}{(\omega-\xi_i)^2+\Gamma_i^2} \tag{3.29}$$

where ξ_i are the peak position, representing some average energy of a group of excited states, and Γ are the corresponding peaks widths, describing the spread in energy of exited states, which is related with lifetimes of the average excitations. Let us now derive the equations from which we can obtain a practical solution for the Green function. From the Heisenberg equation of motion for the field operator

$$i\frac{\partial\hat{\psi}(\mathbf{r}t)}{\partial t}=[\hat{\psi}(\mathbf{r}t),H] \tag{3.30}$$

where $\hat{H}$ is the Hamiltonian given in Eq. 3.8, we can obtain the equation of motion of the Green function:

$$\left[i\frac{\partial}{\partial t}-h(\mathbf{r})\right]G(\mathbf{r}t,\mathbf{r}'t') + i\int d\mathbf{r}''v(\mathbf{r}',\mathbf{r}'')\langle N|T\{\hat{\psi}^\dagger(\mathbf{r}''t)\hat{\psi}(\mathbf{r}''t)\hat{\psi}(\mathbf{r}t)\hat{\psi}^\dagger(\mathbf{r}'t')\}|N\rangle=\delta(\mathbf{r}t,\mathbf{r}'t') \tag{3.31}$$

where $\langle N|T\{\hat{\psi}^\dagger(\mathbf{r}''t)\hat{\psi}(\mathbf{r}''t)\hat{\psi}(\mathbf{r}t)\hat{\psi}^\dagger(\mathbf{r}'t')\}|N\rangle$ is the two-particle Green function G_2, which describes the propagation of two particles like a hole-electron pair. For simplicity, in the Fourier frequency space, Eq. 3.31 transforms into

$$[\omega-h]G(\omega)-i\int vG_2(\omega)=1 \tag{3.32}$$

As the next step, instead of dealing with the two-particle Green function, we use the concepts of the perturbation theory to the one-particle Green function. We express the Fourier transform of the inverse of the one-particle Green function in terms of inverse of the one-particle Green function G_H (corresponding to the Hartree Hamiltonian H^H which can be solved as it is a one-particle Hamiltonian) and the perturbation Σ, which is called the "self-energy operator" and assumed

to include all exchange and correlations effects beyond the Hartree potential,

$$G^{-1}(\mathbf{r},\mathbf{r}';\omega) = \delta(\mathbf{r},\mathbf{r}')[\omega - H^H(\mathbf{r})] - \Sigma(\mathbf{r},\mathbf{r}';\omega) \tag{3.33}$$

where $G_H^{-1} = \omega - H^H(\mathbf{r})$. From Eq. 3.33, the self-energy operator is given by $\Sigma = G_H^{-1} - G^{-1}$. Inserting the definition of Σ into Eq. 3.32, we arrive to so-called Dyson equation for the Green function:

$$[\omega - h(\mathbf{r}) - V_H(\mathbf{r})]G(\mathbf{r},\mathbf{r}';\omega) - \int d\mathbf{r}''\Sigma(\mathbf{r},\mathbf{r}'';\omega)G(\mathbf{r}'',\mathbf{r}';\omega) = \delta(\mathbf{r},\mathbf{r}') \tag{3.34}$$

Here, V_H is the Hartree potential. $\Sigma(\mathbf{r},\mathbf{r}'';\omega)$, is a nonlocal (it depends on two spatial variables), non-hermitian and energy dependent operator. Alternatively, we can rewrite the Dyson equation in the form of a geometrical series as

$$G = G_0 + G_0\Sigma G_0 + G_0\Sigma G_0\Sigma G_0 + ... \tag{3.35}$$

which is completely equivalent to Eq. 3.34. G_0 represents the Green function of the one particle Hamiltonian $h+V_H$. Now, if we insert the Lehman representation of the Green function into Eq. 3.34, multiply both sides of the latter equation by $\omega - \varepsilon_j$ and take the $\omega \to \varepsilon_j$ limit, we get the Dyson equation for the electronic excitations ε_j and amplitudes ψ_j:

$$[h(\mathbf{r}) + V_H(\mathbf{r})]\psi_j(\mathbf{r}) + \int d\mathbf{r}'\Sigma(\mathbf{r},\mathbf{r}';\varepsilon_j)\psi_j(\mathbf{r}') = \varepsilon_j\psi_j(\mathbf{r}) \tag{3.36}$$

Supposing we know the form of Σ, since energy is one of its arguments, the above equation has to be solved self-consistently together with the Green function, Eq. 3.25, so that the ε_j's from 3.36 must correspond to the poles of the Green function, where the amplitudes ψ_j form, in general, a set of nonorthogonal functions.
To solve Eq. 3.36, we have to know the form of the self-energy operator or a good approximation for it. In the simplest way, the self-energy operator can be expanded in a power series the bare Coulomb potential v. However, it is well known that such an expansion diverges for metals or that the convergence becomes poor when the polarizabilty of the system increases. An alternative way is expanding it in terms of the screened potential W introduced first by Hubbard

[46],

$$W(12) = v(12) + \int d(34)v(42)P(34)W(13) \tag{3.37}$$

where the kernel P can be expanded as

$$P(12) = -iG(12)G(21) + \int G(13)G(41)W(34)G(24)G(32)d(34) + ... \tag{3.38}$$

Here, we adopt the compressed notation $1 \equiv (\mathbf{r}, t, \sigma)$, $2 \equiv (\mathbf{r}', t', \sigma)$, etc. $W(12)$ essentially gives the potential at point 1 due to the presence of a test charge at point 2, including the effect of the polarization of the electrons. The physical meaning of the kernel $P(12)$ is that it is the polarization propagator that contains the response of the system to the additional particle or hole. The first two terms of the expansion of Σ are

$$\Sigma(12) = iG(12)W(1^+2) - \int G(13)G(34)G(42)W(14)W(32)d(34) + ... \tag{3.39}$$

In the used notation, 1^+ means that $t \to t + \delta$ where δ is a positive infinitesimal. Now, we have to know how many terms of the expansions should be considered for a good description of Σ and P, i.e. the Green function. With this purpose, Hedin [18] rewrote the expansions of Σ, W and P as a set of exact self-consistent equations for the Green function by means of demanding that total energy be stationary with respect to variations in the Green function and introducing a local time-dependent source term Γ (called vertex correction) in the Hamiltonian which directly couples to the particle density. Thus, the Hedin's equations are

$$\Sigma(12) = i \int d(34)G(14)W(1^+3)\Gamma(432) \tag{3.40}$$

$$W(12) = v(12) + \int d(34)v(42)P(34)W(13) \tag{3.41}$$

$$P(12) = -i \int d(34)G(23)G(42)\Gamma(341) \tag{3.42}$$

$$\Gamma(123) = \delta(12)\delta(13) + \int d(4567)\frac{\delta\Sigma(12)}{\delta G(45)}G(46)G(75)\Gamma(673) \tag{3.43}$$

These equations go together with the Dyson equation for the Green function, Eq. 3.35, which links G and Σ. The solution of this set of equations means that the Green function used to calculate the self-energy operator must coincide with the Green function from the Dyson equation with the same self-energy operator. As it can be recognized, the self-consistent solution is difficult to obtain, so we have to approximate it. Solving this set of equation iteratively generates essentially perturbation terms in the screened potential. Hedin proposed to consider only the first iteration to generate the first order perturbation term of W neglecting further terms that are assumed not to be important. It is done by setting $\Gamma(123) = \delta(12)\delta(13)$, where vertex corrections are neglected. Thus, we get

$$\Sigma(12) = iG(12)W(1^+2) \tag{3.44}$$

$$W(12) = v(12) + \int d(34)v(42)P(34)W(13) \tag{3.45}$$

$$P(12) = -iG(12^+)G(21) \tag{3.46}$$

$$\Gamma(123) = \delta(12)\delta(13) \tag{3.47}$$

This is the so-called Hedin's GW approximation, in which the self-energy operator is given as a direct product between the single-particle Green function and the screened potential. Furthermore, usually the irreducible polarizability is replaced by the random-phase approximation (RPA) for the dielectric matrix. By performing carefully the Fourier transform to the energy domain we get:

$$\Sigma^{GW}(\mathbf{r}, \mathbf{r}'; \omega) = \frac{i}{2\pi} \int G(\mathbf{r}, \mathbf{r}'; \omega + \omega')W(\mathbf{r}, \mathbf{r}'; \omega)e^{i\omega\eta}d\omega' \tag{3.48}$$

$$W(\mathbf{r}, \mathbf{r}'; \omega) = v(\mathbf{r}, \mathbf{r}') + \int d\mathbf{r}''W(\mathbf{r}, \mathbf{r}'; \omega) \int d\mathbf{r}'''P(\mathbf{r}'', \mathbf{r}'''; \omega)v(\mathbf{r}''', \mathbf{r}') \tag{3.49}$$

$$P(\mathbf{r}, \mathbf{r}'; \omega) = 2\sum_{ij} \frac{f_i - f_j}{\varepsilon_i - \varepsilon_j - \omega}\psi_i(\mathbf{r})\psi_j^*(\mathbf{r})\psi_i^*(\mathbf{r}')\psi_j(\mathbf{r}') \tag{3.50}$$

$$G(\mathbf{r}, \mathbf{r}', \omega) = \sum_i \frac{\psi_i(\mathbf{r})\psi_i^*(\mathbf{r}')}{\omega - \varepsilon_i + i\eta} \tag{3.51}$$

Here, the expression for the Green function has been included. The sums of the polarization propagator P runs over the ground state and all excitations of the system. f_i indicates the occupation of the amplitudes.

The GW equations imply a self-consistent calculation of the many body Green function G. However, in practice, most GW calculations use the non-interacting Green function G_0 from the Kohn-Sham Hamiltonian, with the Kohn-Sham eigenstates and eigenvalues representing the amplitudes and excitations energies. The screened potential can be evaluated through its relation with bare Coulomb potential,

$$W(\mathbf{r}, \mathbf{r}'; \omega) = \int d\mathbf{r}'' v(\mathbf{r}, \mathbf{r}'') \epsilon^{-1}(\mathbf{r}'', \mathbf{r}; \omega) \tag{3.52}$$

where ϵ^{-1} is the inverse of the dielectric matrix which is given by

$$\epsilon(\mathbf{r}, \mathbf{r}'; \omega) = \delta(\mathbf{r}, \mathbf{r}') - \int d\mathbf{r}'' v(\mathbf{r}, \mathbf{r}'') P(\mathbf{r}'', \mathbf{r}'; \omega) \tag{3.53}$$

Within the RPA approximation, P is that of a noninteracting-particle system defined from G_0: $P = P_0 = G_0(12)G_0(21)$. Thus, to evaluate the inverse of the dielectric function, first we evaluate all matrix elements of the dielectric matrix, in real space, and then calculate the inverse of it. This procedure is usually referred to as $\Sigma = G_0W_0$ since both G and W are not obtained self-consistently through their Dyson equations, but in general it gives acceptable results [19]. Additionally, we have the $\Sigma = GW$ and $\Sigma = G_0W$ approximations where in the first one both G and W are obtained self-consistently and in the last one only W is obtained in this way.

Once the self-energy operator is calculated, the next step would be solving the amplitudes ψ_i in Eq. 3.36 self-consistently. However, in practice, that is not necessary: M. Hybertsen and S. Louie [19] found that, if we expand the amplitudes in terms of the wavefunctions from a density functional theory calculation ψ_n^{KS} and project them on both sides of the self-consistent equation, the resulting amplitudes surprisingly have an overlap 99.99 % with the corresponding one-particle wavefunction from the density functional theory calculation. Also, they found that matrix elements other than the diagonal of the self-energy operator $\langle n|\Sigma|n\rangle$ can be neglected, as the contribution of the non-diagonal matrix elements $\langle n'|\Sigma|n\rangle$

results in errors of 0.01 eV in the excitation energies. The conclusions of the work of S. Louie and M. Hybertsen show that these energies can be obtained by means of correcting the Kohn-sham eigenvalues by the term $\langle\psi_i^{KS}|\Sigma(\varepsilon_i)-V_{xc}|\psi_i^{KS}\rangle$, that is

$$\varepsilon_i \approx \varepsilon_i^{KS} + \langle\psi_i^{KS}|\Sigma(\varepsilon_i) - V_{xc}|\psi_i^{KS}\rangle \tag{3.54}$$

The exchange-correlation contribution is subtracted from the KS eigenvalues because the self-energy operator includes all effects beyond the Hartree approximation. It was stated above that the self-energy operator must be evaluated at the excitation energy. To do this, the operator is expanded to first order in $\varepsilon_i - \varepsilon_i^{KS}$

$$\Sigma(\mathbf{r},\mathbf{r}';\omega) \approx \Sigma(\mathbf{r},\mathbf{r}';\varepsilon_i^{KS}) + (\varepsilon_i - \varepsilon_i^{KS})\frac{\partial\Sigma(\mathbf{r},\mathbf{r}';\omega)}{\partial\omega}|_{\varepsilon_{KS}} \tag{3.55}$$

Thus, the energy is then

$$\varepsilon_i \approx \varepsilon_i^{KS} + Z_i\langle\psi_i^{KS}|\Sigma(\varepsilon_i^{KS}) - V_{xc}|\psi_i^{KS}\rangle \tag{3.56}$$

where Z is a normalization factor

$$Z_i = \left(1 - \langle\psi_i^{KS}|\frac{\partial\Sigma(\mathbf{r},\mathbf{r}';\omega)}{\partial\omega}|_{\varepsilon_i^{KS}}|\psi_i^{KS}\rangle\right)^{-1} \tag{3.57}$$

In the approximation of a noninteracting-particle system, we usually interpret the amplitudes and electronic excitation energies as the wavefunctions and energies of quasiparticles, respectively, which are created when an electron is added (or removed) to (from) an N-particle system. If an electron is added to the system, the strong Coulomb repulsion causes the formation of a hole (with positive charge) around the added electron. These dressed electrons (what we call quasiparticles) form an ensemble in which the $N+1$ quasiparticles interact with each other through the screened Coulomb potential. Similarity, we obtain an ensemble of $N-1$ quasiparticles when we remove an electron.

3.3 Unoccupied electronic states

The evaluation of the irreducible polarizability P [47, 48] and Green function through the Eqs. 3.50 and 3.51 has the disadvantage of having to compute sums over all unoccupied as well as occupied electronic states. The use of all unoccupied states for the evaluation of the polarizability makes the calculation of this physical quantity scale as $A \times O(N^4)$, N being the number of atoms in the system and A a very large prefactor [3]. If such calculation is performed within the plane waves formalism, the computational cost increases considerably because of the large size of the basis sets, making intractable the study of quasiparticle excitations in systems containing more than 100 atoms. Additionally, the convergence of quasiparticle energies with the number of unoccupied states is found to be slow. In order to make further progresses for improving the efficiency in GW calculations, several methods have been explored with the purpose of removing the need of the explicit use of unoccupied electronic states [3, 49]. The use of only occupied states makes the prefactor be smaller than in the case of using all electronic states. Moreover, the use of local orbital bases leads to a much smaller prefactor when compared with planewaves. These facts are particularly relevant when we consider large systems. In this work, we follow the method proposed by F. Giustino et al. [3] which requires only computing the occupied electronic states to evaluate the screened potential and the Green function. We adapt it to the formalism of strictly localized basis orbitals since the equations were originally implemented using plane waves and empirical pseudopotentials.

In this method, the screened potential W is solved self-consistency in the spirit of density functional perturbation theory through the frequency-dependent Sternheimer equation, instead of iteratively as indicated in the original Hedin's equations 3.49 and 3.50. The Sternheimer equation is derived from the time-dependent Kohn-Sham equations

$$i\frac{\partial}{\partial t'}\psi_i(\mathbf{r}'t') = H^{KS}(\mathbf{r}'t')\psi_i(\mathbf{r}'t') \tag{3.58}$$

Here, $\psi_i(\mathbf{r}'t') \equiv \psi_i^{KS}(\mathbf{r}'t')$ and the time-dependent Kohn-Sham Hamiltonian is represented as

$$H^{KS}(\mathbf{r}'t') = -\frac{\nabla^2}{2} + V_{ext}(\mathbf{r}'t') + V_{Hartree}(\mathbf{r}'t') + V_{xc}(\mathbf{r}'t') \tag{3.59}$$

with the last two terms being time dependent as they are functionals of the time-dependent density,

$$n(\mathbf{r}'t') = \sum_{v}^{occ} |\psi_i(\mathbf{r}'t')|^2 \tag{3.60}$$

Considering that the external potential has two components: one of them created by the nuclei and the other one by a monochromatic electric field $V_{field}(\mathbf{r}'t') = \lambda r' cos(\omega t')$ with the magnitude λ being small, the time-dependent Kohn-Sham wavefunctions can be expanded in power of λ by means of using the perturbation theory as follows

$$\psi_i(\mathbf{r}'t') = e^{-i(\varepsilon_i + \lambda\Delta\varepsilon_i)t'}\{\psi_i^{(0)}(\mathbf{r}') + \frac{1}{2}[\lambda e^{i\omega t}\Delta\psi_i(\mathbf{r}', \omega) + \lambda e^{-i\omega t'}\Delta\psi_i(\mathbf{r}', -\omega)]\} \tag{3.61}$$

where $\psi_i^{(0)}(\mathbf{r}')$ and $\varepsilon_i^{(0)}$ are wavefunctions and eigenvalues from the static Kohn-Sham Hamiltonian. In what follows we use the notation $\psi_i^{(0)}(\mathbf{r}') \equiv \psi_i(\mathbf{r}')$ and $\varepsilon_i^{(0)} \equiv \varepsilon_i$. $\Delta\psi_i(\mathbf{r}', \omega)$ and $\Delta\varepsilon_i$ are the first-order variations of the time-dependent Kohn-Sham wavefunctions and eigenvalues, respectively. Thus, inserting Eq. 3.61 into Eq. 3.60, we get:

$$n(\mathbf{r}'t') = n^{(0)}(\mathbf{r}') + \frac{1}{2}[\lambda e^{i\omega t'}\Delta n(\mathbf{r}', \omega) + \lambda e^{-i\omega t'}\Delta n(\mathbf{r}', -\omega)] \tag{3.62}$$

with the following definition of the first order variation of the density:

$$\Delta n(\mathbf{r}', \omega) = \sum_{v}\{\psi_v^*(\mathbf{r}')\Delta\psi_v(\mathbf{r}', \omega) + \Delta\psi_v^*(\mathbf{r}', -\omega)\psi_v(\mathbf{r}')\} \tag{3.63}$$

By replacing the expansion of the wave functions Eq. 3.61 in the time-dependent Kohn-Sham equation, Eq. 3.58 and picking up the first order terms in λ, we

arrive at a Sterheimer equation for the variations of the valence wavefunctions

$$[H^{KS}(\mathbf{r}') - \varepsilon_v \pm \omega]\Delta\psi_v^{\pm}(\mathbf{r}', \omega) = -[1 - \hat{P}_{occ}]\Delta V(\mathbf{r}', \omega)\psi_v(\mathbf{r}') \tag{3.64}$$

Here, $H^{KS}(\mathbf{r}')$ is the static Hamiltonian, $\hat{P}_{occ} = \sum_v |\psi_v\rangle\langle\psi_v|$ is the projector on the occupied states manifold and $\Delta V(\mathbf{r}', \omega)$ is the first order variation of the time-dependent Kohn-Sham Hamiltonian.

We aim at using the previous equation to describe the response of the occupied wavefunctions of a system due to a perturbation given by the screened Coulomb potential $W(\mathbf{r}, \mathbf{r}', \omega)$. In order to evaluate this response, we regard W as a function of the second spatial variable $\mathbf{r}'$, while the the first spatial variable $\mathbf{r}$ and the frequency ω are kept as parameters, $\Delta V_{[\mathbf{r},\omega]}(\mathbf{r}') = W(\mathbf{r}, \mathbf{r'}; \omega)$, so that Eq. 3.64 transforms into

$$[H^{KS} - \varepsilon_v \pm \omega]\Delta\psi^{\pm}_{v[\mathbf{r},\omega]} = -[1 - \hat{P}_{occ}]\Delta V_{[\mathbf{r},\omega]}\psi_v \tag{3.65}$$

We use the notation $f_{[\mathbf{r},\omega]}(\mathbf{r}') = f(\mathbf{r}, \mathbf{r}'; \omega)$ to indicate the parametrization of the frequency and the first spatial variable when required.

The first-order variation of the electronic density due to the variation on the occupied wavefunctions can be rewrite as

$$\Delta n_{[\mathbf{r},\omega]} = 2\sum_{v\sigma} \psi_v \Delta\psi^{*\sigma}_{v[\mathbf{r},\omega]} \tag{3.66}$$

where $\sigma = \pm$ stands for the positive and negative components of the frequency and the factor 2 is introduced to account for spin degeneracy. The screening Hartree potential caused by the induced charge $\Delta n_{[\mathbf{r},\omega]}$ is calculated as usual through

$$\Delta V^H_{[\mathbf{r},\omega]}(\mathbf{r}') = \int d\mathbf{r}'' \Delta n_{[\mathbf{r},\omega]}(\mathbf{r}'') v(\mathbf{r}'', \mathbf{r}') \tag{3.67}$$

Finally, the screened Coulomb interaction in the RPA is calculated as

$$W(\mathbf{r}, \mathbf{r}'; \omega) = \Delta V_{[\mathbf{r},\omega]}(\mathbf{r}') = v(\mathbf{r}, \mathbf{r}') + \Delta V^H_{[\mathbf{r},\omega]}(\mathbf{r}') \tag{3.68}$$

Eqs. (3.65-3.68) must be solved self-consistently and they are completely equivalent to Eqs. (3.49-3.50), but the Sterheimer equation method does not require computing the unoccupied electronic states. The self-consistency is started by initializing W using only the bare Coulomb interaction v, Eq. 3.68.
Additionally, it is possible to modify the Eq. 3.65 to get directly the inverse dielectric matrix $\epsilon^{-1}(\mathbf{r}, \mathbf{r}'; \omega)$. This is done by replacing W by ϵ^{-1}, whose definition in RPA is

$$\epsilon^{-1}_{[\mathbf{r},\omega]}(\mathbf{r}') = \delta(\mathbf{r}, \mathbf{r}') + \Delta V^{H}_{[\mathbf{r},\omega]}(\mathbf{r}') \tag{3.69}$$

In this case the inverse dielectric matrix is initialized with the delta function δ. This procedure is completely equivalent to obtaining ϵ^{-1} from the self-consistent W using Fourier transform techniques.
For the Green function a similar procedure to the Sternheimer equation is followed to solve it without requiring explicitly the unoccupied electronic states. Let us recall the expression Green function given by equation 3.25

$$G(\mathbf{r}, \mathbf{r}'; \omega) = \sum_n \frac{\psi_n(\mathbf{r})\psi_n^*(\mathbf{r}')}{\omega - \varepsilon_n - i\eta} \tag{3.70}$$

Approximating G to G_0 (Kohn-Sham Green function), n runs over all unoccupied as well as occupied electronic states, ψ_n are the single particle wavefunctions with eigenvalues ε_n. The infinitesimal η is negative for occupied states and positive otherwise. Although, this equation looks straightforward to evaluate, it contains a sum over all electronic states. In order to get a more efficient procedure to evaluate the Green function, we proceed breaking it into two terms according to the values that η can take

$$G(\mathbf{r}, \mathbf{r}'; \omega) = \sum_v \frac{\psi_v(\mathbf{r})\psi_v^*(\mathbf{r}')}{\omega - \varepsilon_v - i\eta} + \sum_c \frac{\psi_c(\mathbf{r})\psi_c^*(\mathbf{r}')}{\omega - \varepsilon_c + i\eta} \tag{3.71}$$

where the first sum goes over the valence states and the second one over the conduction states. Now, we add and subtract the term $\sum_v \psi_v\psi_v^*/(\omega - \varepsilon_v + i\eta)$ to the latter equation, to obtain

$$G(\mathbf{r}, \mathbf{r}'; \omega) = \sum_n \frac{\psi_n(\mathbf{r})\psi_n^*(\mathbf{r}')}{\omega - \varepsilon_n + i\eta} + \sum_v \frac{\psi_v(\mathbf{r})\psi_v^*(\mathbf{r}')}{\omega - \varepsilon_v - i\eta} - \sum_v \frac{\psi_v(\mathbf{r})\psi_v^*(\mathbf{r}')}{\omega - \varepsilon_v + i\eta} \tag{3.72}$$

By performing the sum of the last two terms using the Lorentzian representation of Dirac's delta function for a small η, which is defined as $\pi\delta(x) = \eta/(x^2+\eta^2)$, we get

$$G(\mathbf{r},\mathbf{r}';\omega) = G^A(\mathbf{r},\mathbf{r}';\omega) + G^N(\mathbf{r},\mathbf{r}';\omega) \tag{3.73}$$

with

$$G^A(\mathbf{r},\mathbf{r}';\omega) = \sum_n \frac{\psi_n(\mathbf{r})\psi_n^*(\mathbf{r}')}{\omega - \varepsilon_n + i\eta} \tag{3.74}$$

$$G^N(\mathbf{r},\mathbf{r}';\omega) = 2i\pi \sum_v \delta(\omega - \varepsilon_v)\psi_v(\mathbf{r})\psi_v^*(\mathbf{r}') \tag{3.75}$$

$G^A(\mathbf{r},\mathbf{r}';\omega)$ is analytical in the upper half of the complex energy plane as its poles lies below the real axis. $G^N(\mathbf{r},\mathbf{r}';\omega)$ vanishes whenever the frequency ω is above the chemical potential. For frequencies below the chemical potential, it introduces the poles associated to the occupied electronic states. We should notice that $G^N(\mathbf{r},\mathbf{r}';\omega)$ has the desirable form as it only contains occupied states. That does not happen with the analytical part because a sum over all states remains. Following the same ideas of Sternheimer's approach, $G^A(\mathbf{r},\mathbf{r}';\omega)$ is regarded as a function only of the first spatial variable $\mathbf{r}$ while the second one $\mathbf{r}'$ and the frequency ω are kept as parameters. Then, we project the operator $[\hat{H}+\omega+i\eta]$, which depends on the variable $\mathbf{r}'$, on both sides of Eq. 3.74 and use the closure relation $\delta(\mathbf{r},\mathbf{r}') = \sum_n \psi_n(\mathbf{r})\psi_n^*(\mathbf{r}')$ to finally get an inhomogeneous linear system for G^A

$$[\hat{H}^{KS}(\mathbf{r}') - \omega + i\eta]G^A_{[\mathbf{r},\omega]}(\mathbf{r}') = -\delta_{[\mathbf{r}]}(\mathbf{r}') \tag{3.76}$$

This linear equation does not require explicitly the unoccupied electronic states, but it is completely equivalent to Eq. 3.74.

In the next section we rewrite the equations to compute the screened Coulomb potential and Green function using the method presented above within the strictly localized orbital formalism.

3.4 GW approximation in local basis set

As discussed in chapter 2, in the formalism of local orbital bases, each Kohn-Sham wavefunction ψ_i is expanded as a linear combination of the atomic orbitals

in the basis

$$\psi_i(\mathbf{r}') = \sum_\mu c_{i\mu}\phi_\mu(\mathbf{r}') \tag{3.77}$$

where $c_{i\mu}$ are the coefficients of the expansion. The Hilbert space defined by the atomic orbital basis is a subspace of the complete Hilbert space. In that subspace the resulting wavefunctions form a complete orthogonal set $\{\psi_i\}$ that satisfies the following closure relation

$$\sum_i |\psi_i\rangle\langle\psi_i| = 1. \tag{3.78}$$

Assuming that the wave functions of the system perturbed by the screened potential W can be well described with the same basis of local orbitals, the expansion of the first-order variation of the wavefunctions is given by

$$\Delta\psi_{v[\mathbf{r},\omega]}(\mathbf{r}') = \sum_i \Delta c_{vi[\mathbf{r},\omega]}\phi_i(\mathbf{r}') \tag{3.79}$$

with $\Delta c_{vi[\mathbf{r},\omega]}$ being the changes in the coefficients of the wavefunctions. Unless the basis set is very complete, however, the perturbed wavefunctions will in general have components outside of the Hilbert subspace defined by the basis set, and therefore Eq. 3.79 will be an approximation to the true perturbed wavefunctions. The approximation will be better as the basis set is more complete.
After we replace Eqs. 3.79 into the Eq. 3.65 and project both sides onto $\phi_j(\mathbf{r}')$ we obtain the Sternheimer equations in matrix representation

$$[\mathbf{H} - (\varepsilon_v \pm \omega)\mathbf{S}]\Delta\mathbf{c}^{\pm}_{v[\mathbf{r},\omega]} = -[\mathbf{1} - \mathbf{S}\boldsymbol{\rho}^T]\Delta\mathbf{V}_{[\mathbf{r},\omega]}\mathbf{c}_v \tag{3.80}$$

where $\mathbf{H}$, $\mathbf{S}$ and $\boldsymbol{\rho}$ are the Kohn-Sham Hamiltonian, overlap and density matrix, respectively, which come from a standard DFT, ground state calculation. The expressions of their corresponding matrix elements were given in chapter 2. The vectors $\mathbf{c}_\nu$ and $\Delta\mathbf{c}^{\pm}_{v[\mathbf{r},\omega]}$ contain the coefficients of the valence wavefunction ψ_ν. The matrix elements of $\Delta\mathbf{V}_{[\mathbf{r},\omega]}$ are evaluated as

$$\Delta V_{ij[\mathbf{r},\omega]} = \langle\phi_i|\Delta V_{[\mathbf{r},\omega]}|\phi_j\rangle \tag{3.81}$$

In our implementation of the present method in SIESTA, we evaluate the term $\Delta V_{[\mathbf{r},\omega]}$ defined by Eq. 3.68 on the real-space grid in order to avoid the expansion of the bare Coulomb potential in the local orbital basis, which would require the function products $\phi_i(\mathbf{r})\phi_j(\mathbf{r}')$ and result in the need of evaluating four-center and three-center integrals in the Sternheimer equation. Thus, the solution of the Eq. 3.80 yields $\Delta c_{vi[\mathbf{r},\omega]}$ which is then used to obtain the variation in the density matrix

$$\Delta n_{ij[\mathbf{r},\omega]} = 2 \sum_{v,\sigma=\pm} c^*_{vi} \Delta c^*_{vi[\mathbf{r},\omega]} \tag{3.82}$$

In order to evaluate the integral in Eq. 3.67 on the real-space grid, one has to explicitly calculate $\Delta n(\mathbf{r}, \mathbf{r}'; \omega)$ on such grid, that is

$$\Delta n_{[\mathbf{r},\omega]}(\mathbf{r}') = \sum_{ij} \Delta n_{ij[\mathbf{r},\omega]} \phi^*_i(\mathbf{r}') \phi^*_j(\mathbf{r}') \tag{3.83}$$

Then, the term $\Delta V^H_{[\mathbf{r},\omega]}(\mathbf{r}')$ is added to the bare Coulomb potential to update the screened Coulomb potential. In the case of the inverse dielectric function, $\Delta V^H_{[\mathbf{r},\omega]}(\mathbf{r}')$ is added to the delta function in the Eq. 3.80. Finally, $\Delta V_{[\mathbf{r},\omega]}$ in Eq. 3.68 (or $\epsilon^{-1}_{[\mathbf{r},\omega]}(\mathbf{r}')$ in Eq. 3.69) is then replaced by the new value obtained previously and the procedure is repeated again until the self-consistency is reached. Within this scheme the self-consistency is performed independently for each value of the parameters $\mathbf{r}$ and ω. This allows to use a rougher grid for the spatial variable $\mathbf{r}$ than the one used for $\mathbf{r}'$ and the real-space integrals. The optimal fineness of the grid for operations in $\mathbf{r}'$ is determined by the accuracy needed for describing the Kohn-Sham Hamiltonian because $\mathbf{H}$ and $\mathbf{S}$ are included in the parametrized Sterheimer equation. For $\mathbf{r}$ the fineness of the grid depends on the accuracy required to represent the screened Coulomb potential.
In the case of the Green function, the expression of its non-analytical part is straightforward to expand in the local atomic orbitals

$$G^N(\mathbf{r}, \mathbf{r}'; \omega) = 2\pi i \sum_{vij} \delta(\omega - \varepsilon_v) c_{vi} c^*_{vj} \phi_i(\mathbf{r}) \phi^*_j(\mathbf{r}') \tag{3.84}$$

The evaluation of the above equation does not require explicitly the parametrization of variables $\mathbf{r}$ and ω, but in order to hold the same accuracy as in the

screened Coulomb potential, the spatial variables $\mathbf{r}$ and $\mathbf{r}'$ of the components of the Green function are calculateds on the same grids as those used for evaluating the screened Coulomb interaction. For the analytic part, the parametrization of variables $\mathbf{r}$ and ω gives

$$G^A(\mathbf{r},\mathbf{r}';\omega) = \sum_i \phi_i(\mathbf{r}') G^A_{[\mathbf{r},\omega]i} \tag{3.85}$$

with

$$G^A_{[\mathbf{r},\omega]i} = \sum_{nj} \frac{c_{ni}c^*_{nj}}{\omega - \varepsilon_n + i\eta}\phi^*_j(\mathbf{r}) \tag{3.86}$$

Inserting the Eq. 3.85 into the inhomogeneous linear system, Eq. 3.76 and projecting ϕ^*_j on both sides of this equation, we obtain the matrix representation of the linear system

$$[\mathbf{H} - (\omega + i\eta)\mathbf{S}]\mathbf{G}^A_{[\mathbf{r},\omega]} = -\boldsymbol{\phi}^*_{[\mathbf{r}]} \tag{3.87}$$

where the closure relation Eq. 3.78 in r-representation has been used to operate the right hand side of the linear system. The completeness of the closure relation is ensured since the expansion of the wavefunctions is performed on a Hilbert subspace. The demonstration of this fact is given in Appendix [**]. The vector $\boldsymbol{\phi}^*_{[\mathbf{r}]}$ contains the values of the local orbitals at the parametrized $\mathbf{r}$. The solution of the linear system yields the vector $\mathbf{G}^A_{[\mathbf{r},\omega]}$ which is then used to calculate $G^A(\mathbf{r},\mathbf{r}';\omega)$ through Eq. 3.85. With this procedure, we do not need to calculate Eq. 3.74 where all electronic states are required, instead we solve a liner system that does not require explicitly the electronic states.

With the purpose of verifying the results obtained from the linear system, we perform the calculation of the analytical part of the Green function employing all electronic states. Both calculations must give the same results. Another useful test for the validation of the Green function is the calculation of the density of states from the spectral function $A(\mathbf{r},\mathbf{r};\omega)$ defined by Eq. 3.27, where the ψ_i's correspond to the Kohn-Sham wavefunctions as we are employing the non-interacting Green function. The density of states is obtained by integrating the

diagonal elements of the spectral function over the spatial variable, that is,

$$D(\omega) = \int d\mathbf{r} A(\mathbf{r}, \mathbf{r}; \omega) = \frac{1}{\pi} \int d\mathbf{r} \mathbf{Im} |G(\mathbf{r}, \mathbf{r}; \omega)| \tag{3.88}$$

The maxima of the resonances of density of states calculated through the above equation must be centred at the Kohn-Sham eigenvalues.

The equations we give above to calculate the ingredients of the self-energy operator using localized orbitals are applicable only to finite systems. In order to extend the method for periodic systems, we have to rewrite the equations considering the eigenfunctions $\psi_{nk}(\mathbf{r})$ of the one-electron Hamiltonian with a periodic potential. As dictated by Bloch's theorem, such eigenfunctions are described as a periodic function $u_{nk}(\mathbf{r})$ (with the periodicity of the Bravais lattice) modulated by a plane wave:

$$\psi_{nk}(\mathbf{r}) = \frac{1}{\sqrt{V}} e^{i\mathbf{k}\cdot\mathbf{r}} u_{nk}(\mathbf{r}) \tag{3.89}$$

An alternative way of presenting this theorem is in terms of the relative phase of the wavefuction at points separated by a vector $\mathbf{R}$ of the Bravais lattice, namely

$$\psi_{nk}(\mathbf{r} + \mathbf{R}) = e^{i\mathbf{k}\cdot\mathbf{R}} \psi_{nk}(\mathbf{r}) \tag{3.90}$$

Thus, the one-particle Schrödinger equation can be rewritten as

$$e^{-i\mathbf{k}\cdot\mathbf{r}'} \hat{H} e^{i\mathbf{r}'\cdot\mathbf{k}} u_{n\mathbf{k}}(\mathbf{r}') = \varepsilon_{n\mathbf{k}} u_{n\mathbf{k}}(\mathbf{r}') \tag{3.91}$$

in terms of the periodic functions $u_{n\mathbf{k}}(\mathbf{r}')$ where the Hamiltonian is defined as $e^{-i\mathbf{k}\cdot\mathbf{r}'} \hat{H} e^{i\mathbf{r}'\cdot\mathbf{k}}$. This equation simplifies the problem of obtaining the wavefunctions $\psi_{n\mathbf{k}}(\mathbf{r})$ and their corresponding eigenvalues since it can be solved considering only the unit cell. In fact, this is what we do in a DFT calculation and even in the GW approximation as we will see later. Now we move to the formalism of localized orbitals.

In a localized orbital basis the periodic part of the Schrödinger wavefunctions is expanded as a linear combination of cell-periodic functions $\phi^k_\mu(\mathbf{r})$

$$u_{nk}(\mathbf{r}') = \sum_\mu c^k_{n\mu} \phi^k_\mu(\mathbf{r}') \tag{3.92}$$

where $c^k_{n\mu}$ are the coeficients of the expansion and the cell-periodic functions $\phi^k_\mu(\mathbf{r})$ are given by

$$\phi^k_\mu(\mathbf{r}) = \sum_{\mathbf{R}} e^{i\mathbf{k}\cdot(\mathbf{R}-\mathbf{r})}\phi_\mu(\mathbf{r}-\mathbf{R}) \tag{3.93}$$

with $\phi_\mu(\mathbf{r}-\mathbf{R})$ being a localized orbitals of the unit cell traslated by the lattice vector $\mathbf{R}$. The sums in Eq. 3.92 and 3.93 run over the orbitals in the unit cell and lattice vectors of the Bravais lattice, respectively. Here, we use the index k to indicate a implicit dependence with respect to wavevector $\mathbf{k}$. Inserting the Eqs. 3.92 and 3.93 into Eq. 3.89, it is straightforward to demonstrate that the resulting wavefunctions satisfy the Bloch theorem. The coefficients $c^k_{n\mu}$ and eigenvalues are obtained by solving the Schödinger equation for $u_{n\mathbf{k}}(\mathbf{r}')$ in the matrix representation for each k (which one can easily derive from Eq. 3.91 using Eqs. 3.92 and 3.93)

$$[\mathbf{H}^k - \varepsilon^k\mathbf{S}^k]\mathbf{c}^k = 0 \tag{3.94}$$

where the matrix elements of the Hamiltonian and the overlap matrix depending on $\mathbf{k}$ are defined as

$$H^{\mathbf{k}}_{ij} = \sum_{\mathbf{R}} e^{i\mathbf{k}\cdot\mathbf{R}} \int \phi^*_i(\mathbf{r}')\hat{H}\phi_j(\mathbf{r}'-\mathbf{R})d\mathbf{r}' \tag{3.95}$$

$$S^{\mathbf{k}}_{ij} = \sum_{\mathbf{R}} e^{i\mathbf{k}\cdot\mathbf{R}} \int \phi^*_i(\mathbf{r}')\phi_j(\mathbf{r}'-\mathbf{R})d\mathbf{r}' \tag{3.96}$$

The solution of Eq. 3.94 is obtained in a standard SIESTA calculation where the integrals included in the matrix elements of the Hamiltonian and the overlap are evaluated using a real-space grid.

In analogy with Eq. 3.79, the first-order variation of the periodic part of the wavefunctions $u_{v\mathbf{k}}(\mathbf{r}')$ of the valence states is given by

$$\Delta u_{v\mathbf{k}[\mathbf{q},\mathbf{r},\omega]}(\mathbf{r}') = \sum_i \Delta c_{v\mathbf{k}[\mathbf{q},\mathbf{r},\omega]}\phi_{i\mathbf{k}+\mathbf{q}}(\mathbf{r}') \tag{3.97}$$

where $\mathbf{q}$ is the wavevector of the perturbation, which is represented together with $\mathbf{k}$ in the first Brillouin zone. In this case, the variables $\mathbf{r}$, ω and $\mathbf{q}$ are parametrized as indicated above except that the wavevector is parametrized in

the first Brillouin zone. Now, we can write the Sternheimer equation for periodic systems. For that, we use the k-Hamiltonian $e^{-i\mathbf{k}\cdot\mathbf{r}'}\hat{H}e^{i\mathbf{r}'\cdot\mathbf{k}}$, replace $\psi_v(\mathbf{r}')$ and $\Delta\psi_v(\mathbf{r}')$ by $u_{v\mathbf{k}}(\mathbf{r}')$ and $\Delta u_{v\mathbf{k}[\mathbf{q},\mathbf{r},\omega]}(\mathbf{r}')$, respectively, and project the cell-periodic function $\phi_{i\mathbf{k}}(\mathbf{r}')$ on both right sides of Sternheimer equation, to finally obtain

$$[\mathbf{H}_{\mathbf{k}+\mathbf{q}} - (\varepsilon_{v\mathbf{k}} \pm \omega)\mathbf{S}_{\mathbf{k}+\mathbf{q}}]\Delta\mathbf{c}^{\pm}_{v\mathbf{k}[\mathbf{q},\mathbf{r},\omega]} = -[\mathbf{1} - \mathbf{S}_{\mathbf{k}+\mathbf{q}}\boldsymbol{\rho}^{T}_{\mathbf{k}+\mathbf{q}}]\Delta\mathbf{V}_{\mathbf{k}[\mathbf{q},\mathbf{r},\omega]}\mathbf{c}_{v\mathbf{k}} \tag{3.98}$$

Here, the matrix elements of $\mathbf{H}_{\mathbf{k}}$ and $\mathbf{S}_{\mathbf{k}}$ are calculated through Eqs. 3.95 and 3.96. The elements of the density matrix depending on $\mathbf{k}$ are given by

$$\rho_{\mathbf{k}ij} = \sum_{n} c^{*}_{\mathbf{k}in} f_{\mathbf{k}n} c_{\mathbf{k}nj} \tag{3.99}$$

with $f_{\mathbf{k}n}$ being the occupations. The expression to calculated the elements of perturbation matrix is

$$\Delta V_{ij\mathbf{k}[\mathbf{q},\mathbf{r},\omega]} = \sum_{\mathbf{R}} e^{i\mathbf{k}\cdot\mathbf{R}} \int d\mathbf{r}'\phi_i(\mathbf{r}')\Delta v_{[\mathbf{q},\mathbf{r},\omega]}(\mathbf{r}')e^{i\mathbf{q}\cdot\mathbf{r}'}\phi_j(\mathbf{r}'-\mathbf{R}), \tag{3.100}$$

where $\Delta v_{[\mathbf{q},\mathbf{r},\omega]}(\mathbf{r}')$ is the cell-periodic component of the perturbation with wavevector $\mathbf{q}$

$$\Delta V_{[\mathbf{r},\omega]}(\mathbf{r}') = \frac{1}{N_q}\sum_{q} e^{i\mathbf{q}\cdot(\mathbf{r}-\mathbf{r}')}\Delta v_{[\mathbf{q},\mathbf{r},\omega]}(\mathbf{r}') \tag{3.101}$$

The integral in Eq. 3.100 is evaluated in the same way as the one included in the Hamiltonian matrix elements (Eq.3.95) . For the calculation of the self-consistent potential in Eq. 3.98 we analyze the density variation in Bloch components as

$$\Delta n_{[\mathbf{r},\omega]}(\mathbf{r}') = \frac{1}{N_{\mathbf{q}}}\sum_{\mathbf{q}} e^{i\mathbf{q}\cdot\mathbf{r}}\Delta n_{[\mathbf{q},\mathbf{r},\omega]}(\mathbf{r}') \tag{3.102}$$

and calculate the periodic part $\Delta n_{[\mathbf{q},\mathbf{r},\omega]}$ on the real space grid through

$$\Delta n_{[\mathbf{q},\mathbf{r},\omega]}(\mathbf{r}') = \frac{2}{N_{\mathbf{k}}}\sum_{v\mathbf{k}\sigma=\pm}\sum_{ij} c^{*}_{vi\mathbf{k}}\Delta c^{\sigma}_{vj\mathbf{k}[\mathbf{q},\mathbf{r},\omega]}\sum_{\mathbf{R}\mathbf{R}'} e^{-i\mathbf{k}\cdot(\mathbf{R}-\mathbf{R}')}e^{-i\mathbf{q}\cdot\mathbf{R}'}e^{-i\mathbf{q}\cdot\mathbf{r}'}\phi_i(\mathbf{r}'-\mathbf{R})\phi_j(\mathbf{r}'-\mathbf{R}') \tag{3.103}$$

In the case of the Green function, the cell-periodic part of its analytical and non-analytical component are

$$G^A_{\mathbf{k}}(\mathbf{r},\mathbf{r}';\omega) = \sum_n \frac{u_{n\mathbf{k}}(\mathbf{r}')u^*_{n\mathbf{k}}(\mathbf{r})}{\omega - \varepsilon_{n\mathbf{k}} + i\eta} \tag{3.104}$$

and

$$G^N_{\mathbf{k}}(\mathbf{r},\mathbf{r}';\omega) = 2\pi i \sum_v \delta(\omega - \varepsilon_{v\mathbf{k}})u_{v\mathbf{k}}(\mathbf{r}')u^*_{v\mathbf{k}}(\mathbf{r}), \tag{3.105}$$

respectively. They have to be evaluated for each $\mathbf{k}$ point. Expanding the functions $u_{n\mathbf{k}}(\mathbf{r})$ in the second equation and their corresponding cell-periodic functions we immediately obtain the following expression

$$G_{\mathbf{k}[\mathbf{r},\omega]}(\mathbf{r}') = 2\pi i \sum_{vij} \delta(\omega - \varepsilon_{\mathbf{k},v})c^*_{vi\mathbf{k}}c_{vj\mathbf{k}}e^{-i\mathbf{kr}}\phi_i(\mathbf{r}) \sum_{\mathbf{R}} e^{i\mathbf{k}(\mathbf{R}+\mathbf{r}')}\phi_j(\mathbf{r}'-\mathbf{R}) \tag{3.106}$$

On the other hand, to obtain the linear system for the nonanalytical component we follow the same procedure used for non-periodic systems. We first expand the functions $u_{n\mathbf{k}}(\mathbf{r})$ in terms of the cell-periodic functions, then define all terms that do not depend on $\mathbf{r}'$ as $G^A_{\mathbf{k}[\mathbf{r},\omega]i}$. Thus, we obtain

$$G^A_{\mathbf{k}[\mathbf{r},\omega]}(\mathbf{r}') = \sum_i \phi_{\mathbf{k}i}(\mathbf{r}')G^A_{\mathbf{k}[\mathbf{r},\omega]i} \tag{3.107}$$

Finally, we insert this equation into Eq. 3.76 and project both right hand sides by the cell-periodic function $\phi_{\mathbf{k}j}(\mathbf{r})$ to obtain the linear system

$$[\mathbf{H}_{\mathbf{k}} - \omega^+\mathbf{S}_{\mathbf{k}}]\mathbf{G}^A_{\mathbf{k}[\mathbf{r},\omega]} = -\boldsymbol{\phi}^*_{\mathbf{k}[\mathbf{r}]} \tag{3.108}$$

where $\boldsymbol{\phi}_{\mathbf{k}[\mathbf{r}]}$ is a vector containing the values of all cell-periodic functios that are nonvanishing at $\mathbf{r}$. As for non-periodic systems, the solution of this equation yields the vector $\mathbf{G}^A_{\mathbf{k}[\mathbf{r},\omega]}$ which is then used to obtain $G^A_{\mathbf{k}}(\mathbf{r},\mathbf{r}';\omega)$ through Eq. 3.107. Also, for testing purposes, we calculate the analytical part of the Green function using both all electronic states and only occupied states, and compare each other as a way of verifying our results.

3.5 Real-space grid

In this section we describe how the ingredients of the GW approximation are evaluated in the real-space grid of SIESTA. The grid used in a standard calculation with SIESTA is defined in the fundamental unit cell and its fineness is controlled by the mesh-cutoff parameter (the maximum kinetic energy of the plane waves that can be represented in that real space grid) which has energy units (E_{cut}) and must be defined in the SIESTA input file. The optimal value for E_{cut} is determined by convergence of the Kohn-Sham total energy with respect to this parameter.

To evaluate the cell-periodic part of both the screened potential W and the Green function G in which one of their spatial variables is parametrized ($f_{[\mathbf{r}]}(\mathbf{r}') = f(\mathbf{r},\mathbf{r}')$ with f being W or G or ε^{-1}), we use two independent real-space grids. Both of them defined in the fundamental unit cell. The first of these grids is used to evaluate the integrals to obtain the matrix elements of the Hamiltonian, overlap and density matrices, which appear in the corresponding equations to evaluate W and G. This grid is the same than that used in a standard DFT calculation. The second grid is used to define the points where W and G are evaluated in the real space.The accuracy required for G and W in the real space is usually obtained using a coarser sampling points for the second grid than the one of the first grid.

3.6 Computational details

As a preliminary application of our approach, we calculate the dielectric function and the macroscopic dielectric constant for different prototype materials, ranging from insulators to semiconducting materials: lithium chloride (LiCl), silicon, diamond and germanium. These quantities can be evaluated in two alternative ways. The first one is using Eq. 3.68 to define the screened Coulomb potential, which is calculated self-consistently from Eq. 3.65. The selfconsistent procedure is started using as the initial perturbation the $\mathbf{G}$ component of the bare, static Coulomb potential: $\Delta V_{[\mathbf{r},\omega]}(\mathbf{r}') = exp[i(\mathbf{q}+\mathbf{G})\cdot\mathbf{r}']$, and by taking the Fourier component of the resulting self-consistent potential corresponding to the wavevector

G'. The inverse of the dielectric matrix easily, using Eq. 3.52 transformed to Fourier space. In the second method, we solve directly the inverse of the dielectric matrix, by using Eq. 3.69 to define the potential entering in the Sternheimer Equation 3.65, which has the advantage of the need of inverting Eq. 3.52. We have used both method to compute the dielectric function and macroscopic dielectric constant with the purpose of validating our results since these method should be completely equivalent. As we, indeed, obtain the same results, we will only show those obtained using the second method. The dielectric function is obtained as $\epsilon(\mathbf{q},\omega) = 1/\epsilon^{-1}_{00}(\mathbf{q},\omega)$ and the macroscopic dielectric constant as $\epsilon_0 = \epsilon(\mathbf{q} \to 0, \omega = 0)$.

Our calculations are performed within the local-density approximation (LDA) to density-functional theory, and with norm-conserving pseudopotentials. The inverse dielectric matrices are calculated by sampling the Brillouin zone using a shifted $12 \times 12 \times 12$ grid for diamond, silicon and germanium, and a shifted $10 \times 10 \times 10$ grid for LiCl. The lattice parameters are 5.43, 3.56, 5.65 and 5.13 $\mathring{A}$ for silicon, diamond, germanium and LiCl, respectively. Using a standard triple-ζ polarized (TZP) basis we obtain direct band gaps of 2.55 eV (Si), 5.61 eV (diamond), 0.016 eV (Ge), and 6.08 eV (LiCl), in good agreement with standard LDA results. In order to generate basis sets for silicon with a large number of ζ's we use an energy-shift parameter of 10 meV. This shift leads to localization radii of 4.9 $\mathring{A}$ (Si), 3.9 $\mathring{A}$ (C) and 5.0 $\mathring{A}$ (Ge), which is slightly larger that those adopted in standard ground-state calculations in SIESTA. We compare our results with plane-wave calculations performed using the ABINIT [50] and YAMBO [51] software packages, with the same pseudopotentials and Brillouin-zone sampling for consistency. In particular we adopt a pseudopotential format which allows us to use identical local and nonlocal components as in ABINIT and YAMBO. Plane-wave calculations are carried out using kinetic energy cutoffs of 20 Ry for Si and Ge, and 60 Ry for diamond and LiCl. In the plane wave calculations, dielectric matrices are obtained within the random-phase approximation using the Adler-Wiser formulation [52, 53], and we use 92 conductions bands and kinetic energy cutoffs of 6.9 Ry for silicon, germanium and LiCl, and 12 Ry for diamond. Within SIESTA, the long-wavelength limit $\mathbf{q} \to 0$ is obtained by considering a small but finite wavevector of $q = 0.012\pi/a$, a being the lattice parameter, while

with plane-waves this limit is calculated analytically.

3.7 Results and Discussion

In this section, we present the results of the study of the convergence of the macroscopic dielectric constant as a function of the basis set size, comparing systematically this convergence with the results obtained from plane waves. We follow the procedure showed in chapter 2 for the generation of the strictly localized orbitals, including polarized orbitals, to increase the size of the basis set.

3.7.1 Dielectric constant

Silicon

Figure 3.1 (a) shows the variation of the calculated macroscopic dielectric constant of silicon with the size of the basis set (given in terms of the number of orbitals per atom), for an energy shift and split norm of 10 meV and 0.15, respectively. The minimal basis set, which is the single-ζ basis, contains four orbitals per atom (one $3s$ orbital and three $3p$ orbitals). Clearly, we can see that the basis sets not including polarized orbitals converges to a value that is $\approx$ 10.0 % away from the plane-waves value indicated by the horizontal line. Including polarized orbitals in the basis set improves considerably the quality of the basis and the convergence. With the TZP basis (17 orbitals per atom), the value of the dielectric constant is 12.02, which is within 2 % of our plane-waves results ($\epsilon = 12.25$). For comparison, the minimal polarized basis set SZP (9 orbitals per atom) is within 10 % of the convergence value.
In the Fig. 3.1 (b), we present the convergence of the dielectric constant using only polarized basis sets, for two values of the split norm parameter. By increasing its value, the dielectric constant converges to the the plane-waves value more rapidly. We assign this trend to the fact that a larger split norm leads to a wider range of localization radii spanned by the additional basis functions, and hence improves the completeness of the basis set.

Diamond

Figure 3.2 (a) shows the macroscopic dielectric constant for diamond as a function of the basis set size, for a energy shift and split norm of 10 meV and 0.15, respectively. As in the case of Silicon, the convergence value with the basis set size trends to two different values depending on whether polarized orbitals are used or not. Increasing the basis size without including polarized orbitals results in a slower convergence rate and a converged value slightly smaller than the value from plane waves. With polarized orbitals convergence trends to the value from plane-waves $\epsilon_0 = 5.39$. The converged value for the polarized basis set is $\epsilon_0 = 5.45$ for the 4Z4P basis, which includes 36 orbitals per atom. As in the case of silicon a reasonably converged value of ($\epsilon_0 = 5.40$) is already obtained using the TZP basis.

Figure 3.2 (b) shows the convergence of the dielectric constant with respect to the polarized basis size for two different values of split norm. As for silicon, a similar conclusion can be obtained: by increasing the split norm (i.e. by reducing the cutoff radii of the subsequent ζ's beyond the first-ζ radius) the converged value is reached more rapidly, which can be attributed to the fact that orbitals are more compressed.

Germanium

Figure 3.3 (a) shows the calculated macroscopic dielectric constant of germanium as a function of the basis set size, given in terms of orbitals per atom. As in the previous cases, the basis sets with and without localized orbitals converge to different asymptotic values. However, in both cases the converged value is larger than the value from plane waves. Similarly to the case of silicon and diamond the polarized basis sets converge to a higher dielectric constant $\epsilon_0 = 19.23$. This value is 8 % larger than the reference plane waves result of $\epsilon_0 = 17.71$. Also, we find that the TZP basis set gives a dielectric constant close to the full converged value ($\epsilon_0 = 18.9$). Fig. 3.3 (b) shows the convergence of the dielectric constant with respect to the basis set size for two different values of split norm. As observed in the case of silicon and diamond, convergence is reached more rapidly when the cutoff radii of the subsequent ζ's beyond the single-ζ are shorter.

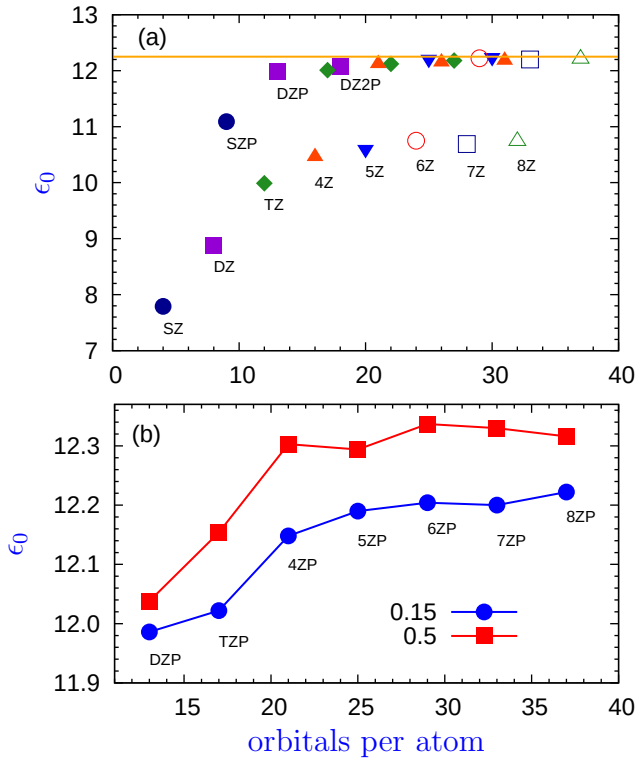

Figure 3.1: (a): Calculated macroscopic dielectric constant of silicon as a function of basis size, given in terms of orbitals per atom. The reference planewaves calculation is indicated by the horizontal line. The datapoints cluster around two distinct curves: the upper curve corresponds to basis sets including polarized orbitals, and the lower curve to basis sets which are not polarized. The number of ζ functions included is indicated by the labels SZ, DZ, TZ etc. The number of polarization orbitals for a given number of ζ functions increases towards the right-hand side, has indicated for the case of the DZ basis. The energy shift is 10 meV and the split norm is 0.15. (b): Calculated macroscopic dielectric constant of silicon as a function of basis size, for two different values of the split norm.

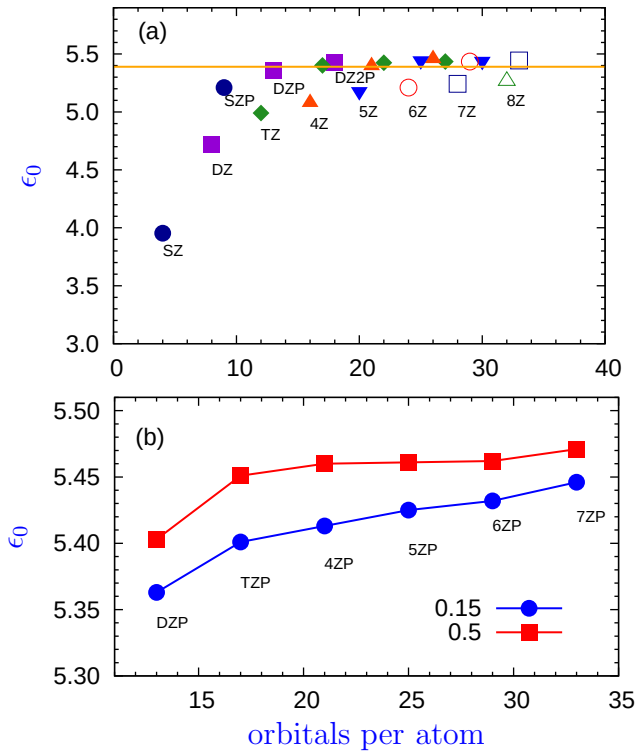

Figure 3.2: (a): Calculated macroscopic dielectric constant of diamond as a function of basis size, given in terms of orbitals per atom. The reference planewaves calculation is indicated by the horizontal line. The datapoints cluster around two distinct curves: the upper curve corresponds to basis sets including polarized orbitals, the lower curve to basis sets without polarization. The number of ζ functions included is indicated by the labels SZ, DZ, TZ etc. The number of polarization orbitals for a given number of ζ functions increases towards the right-hand side, has indicated for the case of the DZ basis. The energy shift is 10 meV and the split norm is 0.15. (b): Calculated macroscopic dielectric constant of silicon as a function of basis size, for two different values of the split norm.

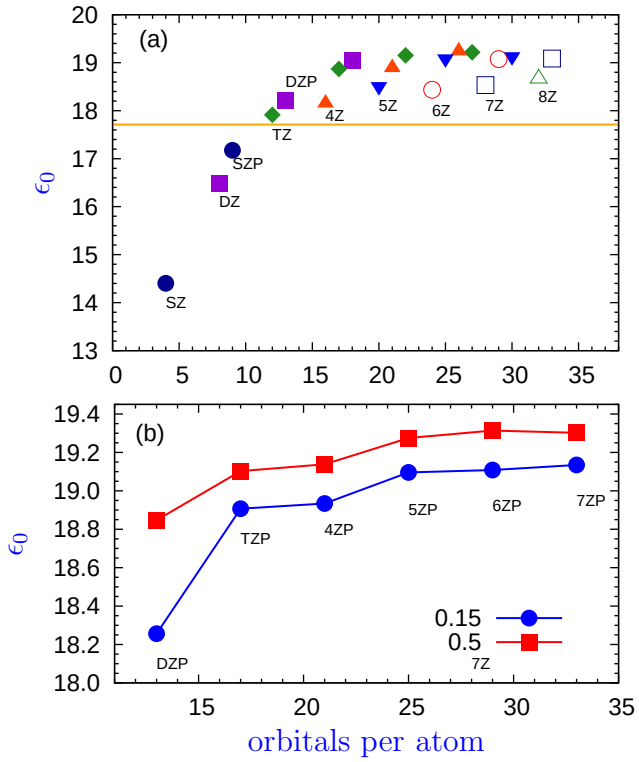

Figure 3.3: (a): Calculated macroscopic dielectric constant of germanium as a function of basis size, given in terms of orbitals per atom. The reference planewaves calculation is indicated by the horizontal line. The datapoints cluster around two distinct curves: the upper curve corresponds to basis sets including polarization orbitals, the lower curve to basis sets without polarization. The number of ζ functions included is indicated by the labels SZ, DZ, TZ etc. The number of polarization orbitals for a given number of ζ functions increases towards the right-hand side, has indicated for the case of the DZ basis. The energy shift is 10 meV and the split norm is 0.15. (b): Calculated macroscopic dielectric constant of silicon as a function of basis size, for two different values of the split norm.

In order to demonstrate the generality of our approach we present in Table 3.1 our calculated dielectric constants for germanium, diamond, and LiCl. The values shown in Table 3.1 are obtained by using the default SIESTA values for the parameters defining the basis set. Table 3.1 provides further support to our

previous finding by showing that the TZP basis provides results which lie within $1\% - 5\%$ of those of the reference plane-wave calculations. We expect further improvement upon designing basis sets specifically optimized for the Sternheimer scheme proposed in this work. In particular the use of numerical diffuse orbitals deserves a systematic assessment.

Table 3.1: Dielectric constant of Si, Ge, diamond and LiCl calculated using our Sternheimer approach and compared to the reference plane-wave calculations and experimental data. We report our results obtained using both the minimal SZ basis and the TZP basis, as generated using the default SIESTA values for the basis set parameters (energy shift of 200 meV and split norm of 0.15)

	SZ	TZP	PW	Expt.
Si	8.32	12.12	12.25	11.9
Ge	15.52	18.74	17.71	16.2
Diamond	3.96	5.38	5.39	5.7
LiCl	1.69	2.71	2.83	2.8

Fig. 3.4 shows the frequency-dependent dielectric function of silicon $\epsilon(\omega)$ for the minimal SZ basis set, the TZP basis set, and the reference planewaves calculation. The SZ basis performs very poorly, the spectral weight being incorrectly transferred from the main absorption peak to higher energy. This is consistent with the small value of the macroscopic dielectric constant obtained with the SZ basis in Fig. 3.1.

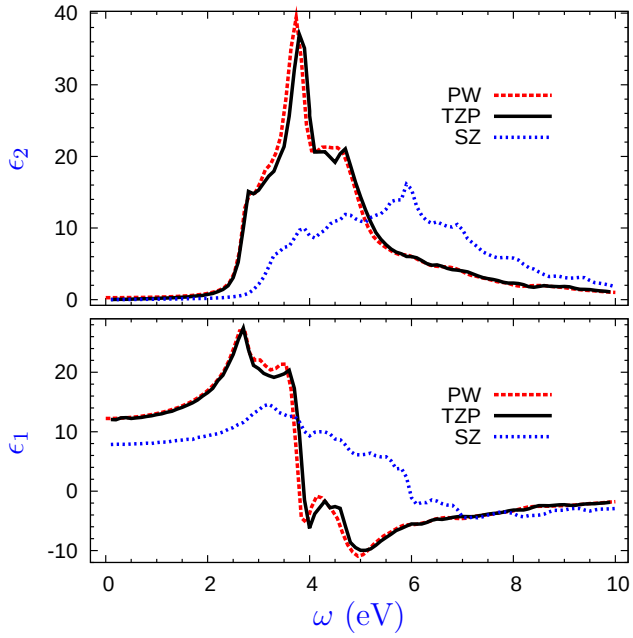

Figure 3.4: Calculated dielectric function of silicon: calculations using the SZ basis (dashed line), the TZP basis (solid line), and the reference planewaves result (dotted line). A Gaussian smearing of width 0.1 eV is used.

The TZP basis yields results in very good agreement with our reference planewaves result. The location and intensity of the main peaks and shoulders are correctly reproduced. We note, however, a very slight blueshift of the hight-energy peaks.

Figures 3.5 and 3.6 show frequency-dependent dielectric functions of diamond and germanium, respectively. Also in these cases we compare the performance of the SZ basis and the TZP basis with the reference planewaves calculation. Conclusions similar to the case of silicon can be drawn: the SZ basis misses the main peak and yields a blueshift of the other peaks, while the TZP basis is in better agreement with the reference planewaves calculation.

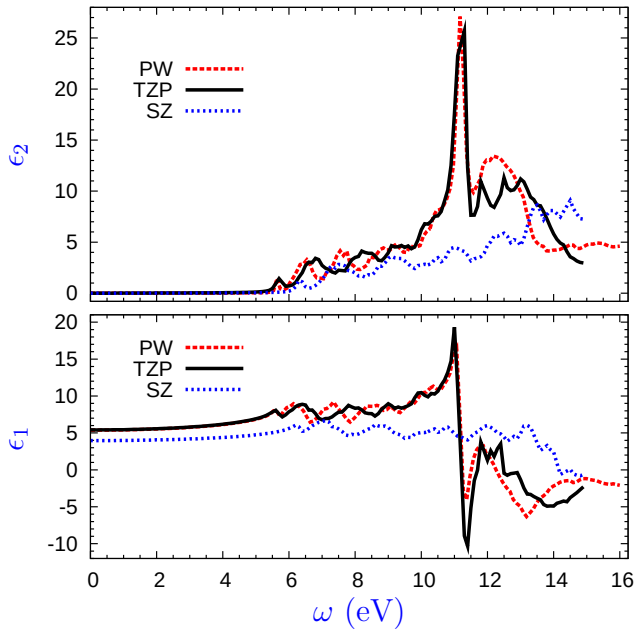

Figure 3.5: Calculated dielectric function of diamond: calculations using the SZ basis (dashed line), the TZP basis (solid line), and the reference planewaves result (dotted line). A Gaussian smearing of width 0.1 eV is used.

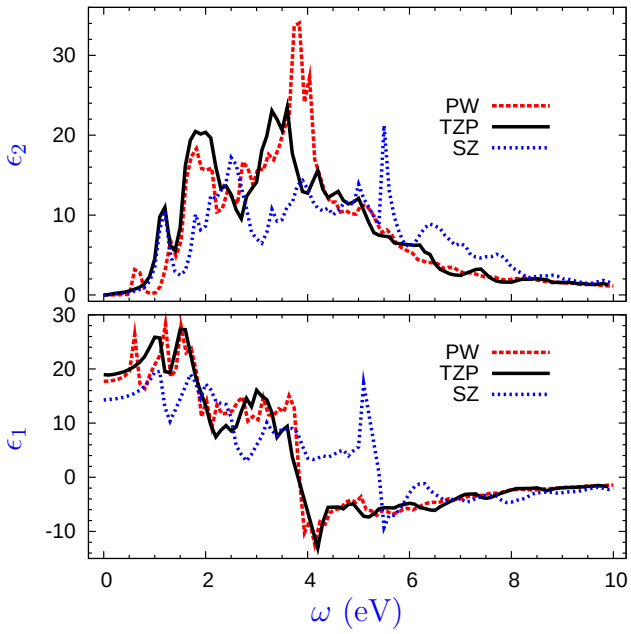

Figure 3.6: Calculated dielectric function of germanium: calculations using the SZ basis (dashed line), the TZP basis (solid line), and the reference planewaves result (dotted line). A Gaussian smearing of width 0.1 eV is used.

Fig. 3.7 shows the wavevector dependence of the dielectric function $\epsilon(\mathbf{q}, \omega = 0)$ for silicon, diamond, and germanium, comparing the performance of the SZ and the TZP basis set. In all cases the wavevector dependence shows the correct behaviour, although the SZ basis yields a smaller dielectric function across the full range of wavevector.

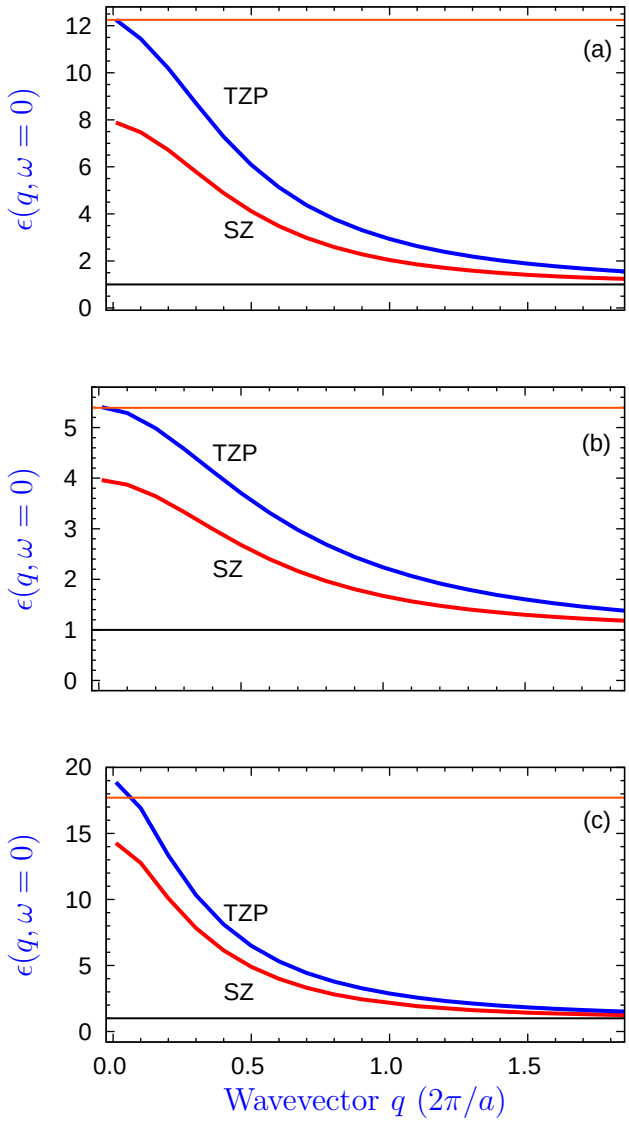

Figure 3.7: Wavevector dependence of the dielectric function of (a) silicon, (b) diamond, and (c) germanium. We compare the performance of the SZ and TZP basis sets. The upper horizontal line in each panel represents the static planewaves value ϵ_0 for $q = 0$, and the lower horizontal line indicates the vacuum dielectric constant ϵ_{vac}

3.7.2 Green function

We perform several tests with the purpose of verifying that we compute the calculation of the Green function correctly. These tests are performed for crystalline silicon as a test system. Fig. 3.8 displays its band structure calculated with SIESTA.

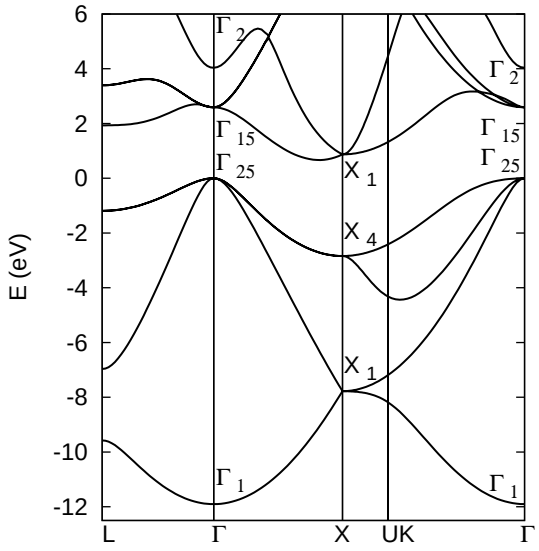

Figure 3.8: Si band structure calculated with SIESTA using the LDA functional and a DZP basis set. The direct and indirect band gap are 2.59 and 0.67 eV, respectively.

We first show the periodicity of the module of the Green function for silicon with $\mathbf{r} = \mathbf{r}'$ calculated for several $\mathbf{k}$ points, keeping ω constant. Fig. 3.9 depicts the module of the Green function for Si (with $\mathbf{r} = \mathbf{r}'$) against $\mathbf{r}$, computed for the irreducible $\mathbf{k}$ points of the first Brillouin zone. We observe that for all $\mathbf{k}$ points (labelled with a number) the Green function has the periodicity of the Si unit cell.

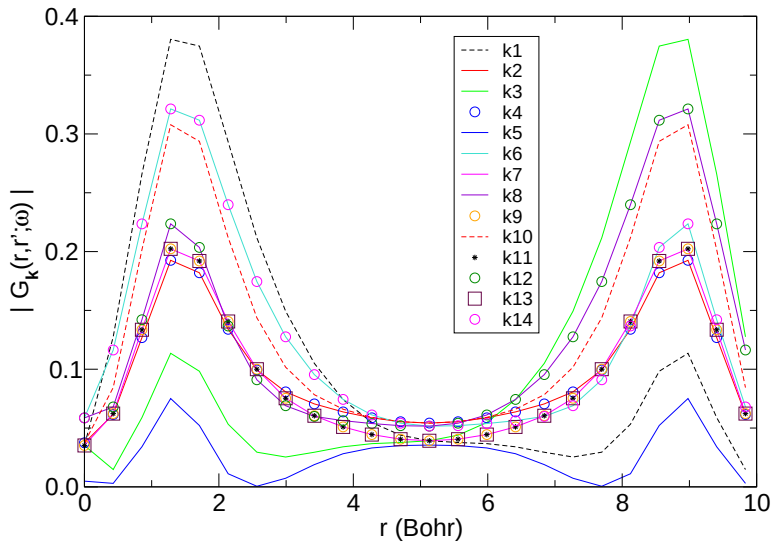

Figure 3.9: Module of Green function for silicon calculated using Eqs. 3.104 and 3.105 (only occupied electronic states required), against $\mathbf{r}$. It is calculated for all the irreducible $\mathbf{k}$ points of the first Brillouin zone of silicon, which are labelled with a number. The module of the Green function was computed along the $\langle 001 \rangle$ direction of the Si unit cell, with $\mathbf{r} = \mathbf{r}'$ and $\omega = 1.0$ eV (which is in the middle of the Si band gap). η is 0.2 eV.

A second test consists in calculating the density of states $D(\omega)$ (DOS) of silicon from the spectral function of the Green function,

$$D(\omega) = \int d\mathbf{r} A(\mathbf{r}, \mathbf{r}; \omega) = \frac{1}{\pi} \int d\mathbf{r} \mathbf{Im} |G(\mathbf{r}, \mathbf{r}; \omega)| \tag{3.109}$$

with $\mathbf{r} = \mathbf{r}'$. Since we approximate G as that of a noninteracting particle system $G = G^0$, $D(\omega)$ can be compared with the density of states from a standard DFT calculation. The Fig. 3.10 we show a representative calculation of the spectral function for Si at Γ point. We show that the projection of the spectral function on the Kohn-Sham orbitals peaks exactly at the position of the Kohn-Sham energies, indicating that the diagonal part of the Green function is calculated correctly.

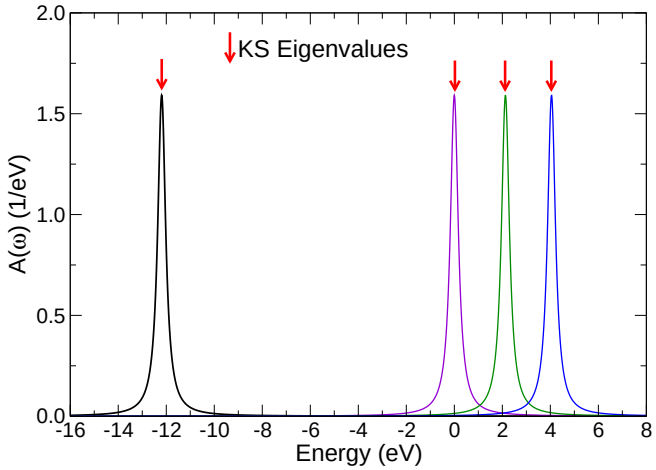

Figure 3.10: Spectral function for Si (solid-line curves) projected on the first lowest energy Kohn-Sham eigenfunctions, at gamma point, that is, $A(\omega) = \langle n|A(\mathbf{r},\mathbf{r};\omega)|n\rangle = (1/\pi)\langle n|ImG(\mathbf{r},\mathbf{r};\omega)|n\rangle$, with $|n\rangle$ being the Kohn-Sham eigenfunction. The Fermi level is set to zero. We use a value of 0.1 for η. The Kohn-Sham eigenvalues are indicated by the red arrows.

As the previous test only allows to verify the diagonal elements of the Green function, to verify all its elements we proceed to calculate the complete Green function matrix using: (i) the equations of its analytical and nonanalytical components (Eqs. 3.104 and 3.105, which only require the occupied electronic states), and (ii) the standard equation that requires to compute over all electronic states (Eq. 3.70), and then comparing both results.
Fig. 3.11 shows the result of comparing the module of the Green function for Si calculated using both methods, where several $\mathbf{k}$ points are considered and with $\mathbf{r} = \mathbf{r}'$. We obtain that both methods yield the same values for the module of the Green function. This confirms that the Green function is correctly computed.

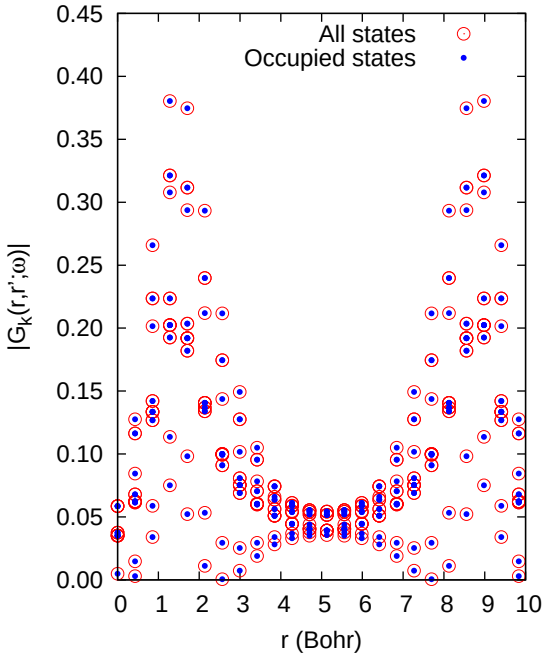

Figure 3.11: Module of Green function for silicon calculated using: (i) all electronic states through Eq. 3.70 (red circles) and (ii) only occupied electronic states through Eqs. 3.104 and 3.105 (blue dots), for the irreducible $\mathbf{k}$ points of the first Brillouin zone of the silicon unit cell (however, the different k points are not distinguished to make the comparison clearer). The module is plotted as a function of $\mathbf{r}$. It was computed along the $\langle 001 \rangle$ direction of the Si unit cell, with $\mathbf{r} = \mathbf{r}'$ and $\omega = -1.0$ eV (which is in the middle of the Si band gap). η is 0.2 eV.

Next, we compare the module of the Green function using $\mathbf{r} \neq \mathbf{r}'$ and $\mathbf{k} \neq (0, 0, 0)$. Fig. 3.12 depicts a representative results where these conditions were met. Both procedures give the same values for the Green function, confirming as in the previous case, that we compute Green function correctly. We also performed several calculations (not shown) fixing $\mathbf{r}'$ at different points and considering different $\mathbf{k}$ points.

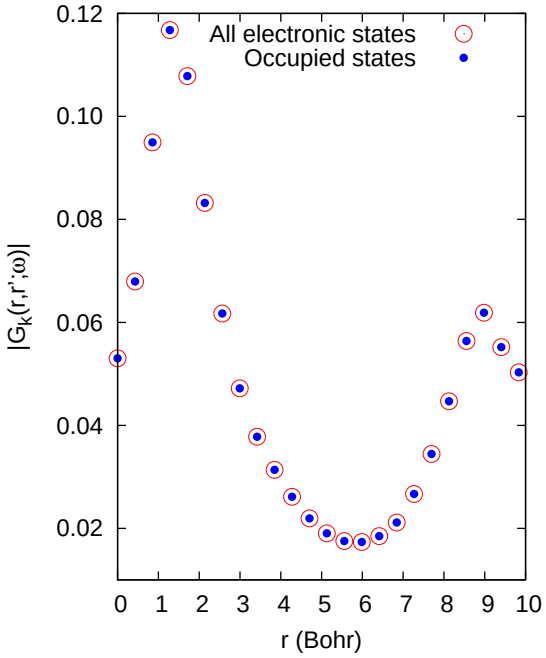

Figure 3.12: Module of the Green function for Si as a function of $\mathbf{r}$ calculated using all electronic states (red circles) and only the occupied electronic states (blue dots). It was calculated along the $\langle 001 \rangle$ direction of the Si unit cell, with $\mathbf{r}'$ fixed at (0,0,0), $\omega = 1.0$ eV, $\mathbf{k} = (0.2, -0.2, 0.2)$ (in cartesian coordinates) and $\eta = 0.2$ eV.

Finally, we investigate the locality of the frequency-dependent Green function in real space. One of the main problems we face with the application of *ab initio* methods, like DFT or the GW approximation, to large system, is the scaling of the number of operations with the system size. For the case of approaches based on DFT, using strictly local orbital basis sets has the advantage that some variables, like the Hamiltonian and the overlap matrices, have a sparsity form (a form of locality), which makes the number of operations needed to compute the approach scale linearly with the size of the system. This is one of the most important features of the SIESTA code. The use of strictly local orbitals could also make the frequency-dependent one-particle Green function to be local, which would enhance the scaling of the GW approximation implemented

in SIESTA. Recently, A. Schindlmayr [54] investigated systematically the locality of the imaginary-time-dependent one-particle Green function built from Wannier orbitals for several system including insulators and metals. Here, we investigate the decay properties of the frequency-space one-particle Green function. For this purpose, we use a Si supercell with size $4 \times 4 \times 4$ and a DZP basis set. Fig. 3.13 shows the decay of the module of the Green function along a symmetric direction in the supercell. We observe that it gradually decays as $|\mathbf{r} - \mathbf{r}'|$ increases, but not sufficiently quickly to be able to neglect it beyond any distance from the origin.

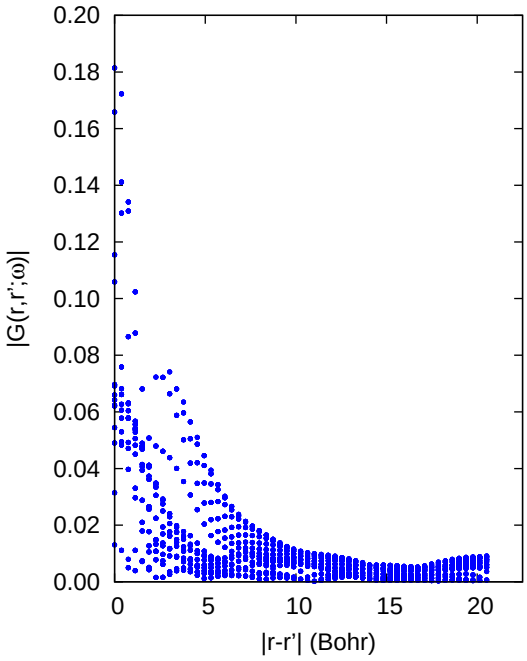

Figure 3.13: Decay of the module of the Green function for a silicon calculated using the linear system, along the $\langle 001 \rangle$ direction of a Si $4 \times 4 \times 4$ supercell, as a function of $|\mathbf{r} - \mathbf{r}'|$. Here, $\mathbf{r}$ and $\mathbf{r}'$ simultaneously run over this direction. Parameters: $\mathbf{k} = 0$, $\omega = 1.0$ eV, and $\eta = 0.2$ eV. To compute the Kohn-Sham eigenvalues and eigenfunction, a DZP basis set was used. The figure only shows the left half of the whole graph (where $|\mathbf{r} - \mathbf{r}'|$ goes from 0 to 40.2 Bohr). The right half is the reflection of the left one.

Fig. 3.14 shows the logarithm of the module of the Green function calculated

for several directions in the Si supercell. In all cases we observe that the Green function decays with distance, but not exponentially.

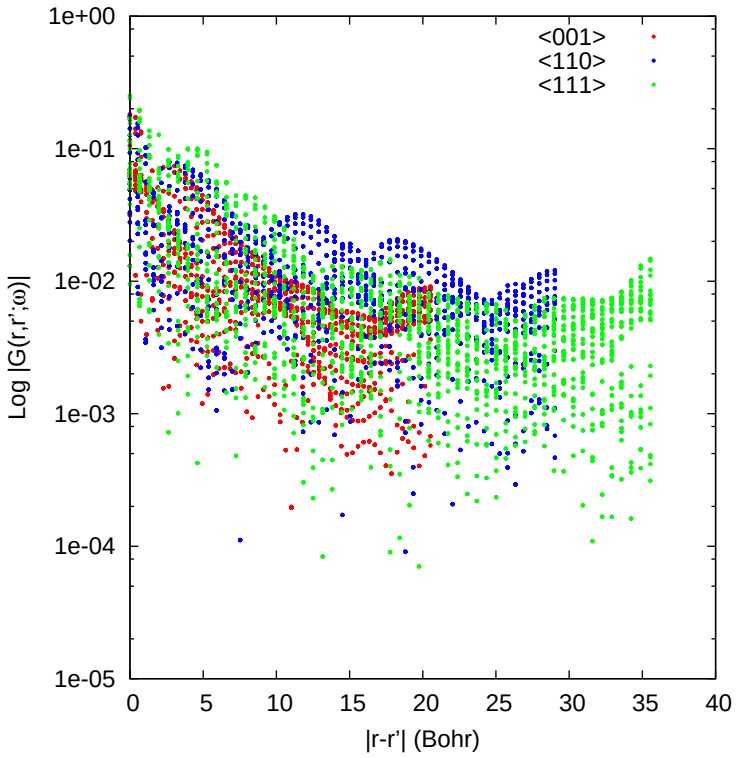

Figure 3.14: Log of the module of the Green function for silicon calculated using the linear system, along the $\langle 001 \rangle$ (red dots), $\langle 110 \rangle$ (blue dots) and $\langle 111 \rangle$ (green dots) directions of a Si $4 \times 4 \times 4$ supercell, as a function of $|\mathbf{r} - \mathbf{r}'|$. Here, $\mathbf{r}$ and $\mathbf{r}'$ simultaneously run over each of these directions. Parameters: $\mathbf{k} = 0$, $\omega = 1.0$ eV, and $\eta = 0.2$ eV. We only show the values of the Log of the Green function obtained with $|\mathbf{r} - \mathbf{r}'|$ between zero and the middle of the length of each direction in the supercell.

For future work, we will proceed to code the subroutine to compute the self-energy operator and evaluate the quasiparticles energies.

Chapter 4

Constrained Density Functional Theory (CDFT)

4.1 Introduction

The two most important methods to study electronic excitations in molecules and periodic systems that lie on density functional theory (DFT) are the time-dependent and the constrained DFT, named TDDFT and CDFT, respectively. In TDDFT, the electronic density and the external potential are time dependent, which allows to reproduce, in principle, the whole electronic spectrum through the linear response of the electronic density with respect to changes of the external potential. Although the formalism of this method is exact, we do not know the exact time-dependent exchange-correlation functional. This is the main drawback of TDDFT method. In practice, one often employs the time-independent exchange-correlation kernel (*i.e* the adiabatic approximation), whether the local density or the generalized gradient approximation. It has been found that TDDFT calculations with this approximation gives excitation energies of low-lying states that agree well with experiments. However, such approximation fails for describing long-range charge-transfer (CT) states because of a self-interaction error in the wave function energies [17]. On the other hand, CDFT has emerged as a powerful method for studying excited electronic states in systems with a constraint on their electronic density, using the basic machinery of Kohn-Sham

self-consistent field procedure. Unlike TDDFT, CDFT is able to determine those excited states that are ground state, i.e. the lowest energy, of an alternative external potential, allowing to deal with problems of electronic excitations for which TDDFT fails, including long-range charge transfers. Also, this method has proven to be successful in describing charge and magnetization fluctuations in solids, parametrizing model Hamiltonians based on DFT calculations and characterizing electron transfer reactions in molecules [4, 5, 6].

To obtain the constrained state in CDFT, we have to find the external potential that has the constrained density as its ground state. Finding this external potential in an efficient way is one of the major challenges in CDFT. One of the earliest techniques was inspection, where one had to explore many potential values until finding the potential that satisfies the constraint condition [4]. This technique is, however, computationally intensive and becomes prohibitive for systems with several constraints. Recently, T. Van Voorhis and Q. Wu [4, 5] have proposed a more efficient method based on the Lagrange multipliers to find efficiently the potential that satisfies the constraint condition. In their method a Lagrange functional is constructed from the Kohn-Sham energy functional with a constraint, which is then maximized. By determining the expressions of the first derivatives of such functional, they found that the maximization can be performed only with respect to Lagrange multiplier (called in what follows as constraining potential), since the electronic density implicitly depends on this potential. They also found, by evaluating the second derivative of the functional with respect to the constraining potential, that the functional is concave, having one maximum. To obtain the constraining potential that maximizes the functional, an optimization technique like the Newton's method should be used. In the present work, we implement and employ the original equations of CDFT method proposed by Van Voorhis et al., but following a different procedure for the maximization of the functional.

This chapter is organized as follows. In Sec. 4.2 the theory of the CDFT approach is given. Then, details of the implementation of this approach in the SIESTA code are discussed in Sec. 4.3. Next, in Sec. 4.4 the qualitative and quantitative tests to verify our approach are discussed along with the obtained results. Finally, we apply our approach to a real problem. The description of the studied system and our results are show and discussed in Sec. 4.5.

4.2 Derivation of the constrained DFT method

Before deriving the equations of the method we implemented, let us derive the standard Kohn-Sham equations as it is an interesting starting point to introduce the concept of Lagrange multipliers within the density functional theory formalism.

To obtain the ground-state total energy of a system with external potential V_{ext}, we minimize the Kohn-Sham energy functional with respect to the electronic density $n(\mathbf{r})$

$$E^{KS} = \min_{n} \left(T_s + \int V_{ext}(\mathbf{r}) n(\mathbf{r}) d\mathbf{r} + E_{Hartree}[n(\mathbf{r})] + E_{xc}[n(\mathbf{r})] \right) \tag{4.1}$$

This minimization is subjected to the orthonormality condition

$$\int \overline{\psi}_i^*(\mathbf{r}) \overline{\psi}_j(\mathbf{r}) d\mathbf{r} = \delta_{ij} \tag{4.2}$$

Thus, the Kohn-Sham energy is minimized using the Lagrange multiplier method, where the Lagrange functional L^{KS} is built, such that its final expression is

$$L^{KS} = E^{KS}[n(\mathbf{r})] + \sum_{kj} \varepsilon_{kj} \left(\delta_{kj} - \int \overline{\psi}_k^*(\mathbf{r}) \overline{\psi_j}(\mathbf{r}) d\mathbf{r} \right) \tag{4.3}$$

with ε_{kj} being the Lagrange multipliers. The stationary equation of L^{KS} with respect to the orbitals $\overline{\psi}$ is obtained by variational differentiation (using the chain rule):

$$\frac{\delta L_{KS}}{\delta \overline{\psi}_i^*(\mathbf{r})} = \frac{\delta T_s}{\delta \overline{\psi}_i^*(\mathbf{r})} + \left[\frac{\delta E_{ext}}{\delta n(\mathbf{r})} + \frac{\delta E_{Hartree}}{\delta n(\mathbf{r})} + \frac{\delta E_{xc}}{\delta n(\mathbf{r})} \right] \frac{\delta n(\mathbf{r})}{\delta \overline{\psi}_i^*(\mathbf{r})} + \sum_j \varepsilon_{ij} \overline{\psi}_j(\mathbf{r}) = 0 \tag{4.4}$$

with

$$\frac{\delta n(\mathbf{r})}{\delta \overline{\psi}_i^*(\mathbf{r})} = \overline{\psi}_i(\mathbf{r}) \tag{4.5}$$

$$\frac{\delta T_s}{\delta \overline{\psi}_i^*(\mathbf{r})} = -\frac{1}{2} \nabla_i^2 \overline{\psi}_i(\mathbf{r}) \tag{4.6}$$

The three terms inside the squared brackets on the right hand side of Eq. 4.4 are the external (V_{ext}), Hartree ($V_{Hartree}$) and exchange-correlation (V_{xc}) potentials, respectively. Inserting Eqs. 4.5 and 4.6 into Eq. 4.4, we get the expression,

$$\left[-\frac{1}{2}\nabla^2 + V_{ext}(\mathbf{r}) + V_{Hartree}(\mathbf{r}) + V_{xc}(\mathbf{r})\right]\overline{\psi}_i(\mathbf{r}) = \sum_j \varepsilon_{ij}\overline{\psi}_j(\mathbf{r}) \tag{4.7}$$

where the terms inside the squared brackets just correspond to the Kohn-Sham Hamiltonian H^{KS}. In principle, this is the equation we need to solve to obtain the ground-state total energy of the system, but it is not directly solved due to the sum over the Lagrange multipliers ε_{ij}. To get a simpler equivalent expression for the above equation that does not include a sum over the Lagrange multipliers ε_{ij}, we introduce an appropriate unitary matrix (called $\mathbf{U}$), so that $\overline{\psi}_j = \sum_i U^+_{ji}\psi_i$ and $\psi_i = \sum_j U_{ij}\overline{\psi}_j$ (with $\mathbf{U}^+$ being the conjugate transpose of $\mathbf{U}$). The result of the basis change, in the matrix representation, is

$$\mathbf{U}\mathbf{H}\mathbf{U}^+\boldsymbol{\psi} = \mathbf{U}\boldsymbol{\varepsilon}\mathbf{U}^+\boldsymbol{\psi} \tag{4.8}$$

where $\boldsymbol{\psi}$ is a vector that contains the ψ_i. The matrix products $\mathbf{U}\boldsymbol{\varepsilon}\mathbf{U}^+$ is diagonal. Thus, for each i we can write

$$H^{KS}\psi_i = \varepsilon_i\psi_i. \tag{4.9}$$

These equations are just the well-known Kohn-Sham equations and they are totally equivalent to the set of equations given by Eq.4.7, but easer to handle as they do not include the sum over Lagrange multipliers. They should be solved self-consistently because the terms of potential in the Kohn-Sham Hamiltonian depend on the electronic density, which is constructed from the Kohn-Sham orbitals ψ_i.

In CDFT, additional constraints are imposed to the electronic density, for instance, to confine the charge of the system within a certain group of atomic or molecular orbitals, or within a certain spatial region of the system, such that the integral of the electronic density $n(\mathbf{r})$ over the constrained orbitals (or volume) of the system must be equal to the desired confined charge. The CDFT method

can be applied to the study of neutral electronic excitations, only if there is full evidence proving that the constrained electronic state corresponds to the electronic excitation we want to describe. Other application of this method include the study of charge and magnetization fluctuations in solids, parametrization of model Hamiltonians based on DFT calculations and characterization of electron transfer reactions. The main advantages of the CDFT method are that it does not require a large amount of computational resources and that its implementation is simple and can be easily coded within any DFT code.
Many interesting problems can be handled using the CDFT method, including charge transfer reactions, localization of charge on impurities including d and f orbitals of metallic atoms, and description of magnetization properties. If we confine a certain charge N_c within a given volume Ω of the system, then

$$\int_{\Omega} n(\mathbf{r})d\mathbf{r} = N_c. \tag{4.10}$$

The net magnetization constraint can be defined as

$$\int_{\Omega} m(\mathbf{r})d\mathbf{r} = M \tag{4.11}$$

where $m(\mathbf{r}) \equiv n^{\alpha}(\mathbf{r}) - n^{\beta}(\mathbf{r})$, with α and β indicating the two components of spin. All the above constraint conditions can be expressed in a more general way as

$$\sum_{\sigma} \int w^{\sigma}(\mathbf{r}) n^{\sigma}(\mathbf{r})d\mathbf{r} = N_c \tag{4.12}$$

where $w^{\sigma}(\mathbf{r})$ is a weight function that defines the region of constraint for each spin of the electronic density, and can be define in several ways (for instance, can be defined as 1 in the constrain region or 0 otherwise.). N_c is the charge in the part of the system (whether a volume, or atomic or molecular orbitals) where the electronic density has been constrained. The integral of the product of the weight function and electronic density must give the constrained charge. The aim is to find the electronic density that satisfies this condition. To achieve it, Q. Wu and T. Van Voorhis [5] use the Lagrange multipliers to construct a new functional from the Kohn-Sham energy functional, containing the constraint condition. To

show the derivation of the method we consider a system with only one constraint, although the method can be easily extended for systems with several constraints, yielding a set of equation having the same form than for the case of using only one constraint.
In the Q. Wu and T. Van Voorhis' method the new functional W is defined as

$$W[n, V_c, \varepsilon_{kj}] = E^{KS}[n(\mathbf{r})] - \sum_{kj} \varepsilon_{kj} \left(\delta_{kj} - \int \psi_k^*(\mathbf{r}) \psi_j(\mathbf{r}) d\mathbf{r} \right) - V_c \left(N_c - \int w(\mathbf{r}) n(\mathbf{r}) \right) \tag{4.13}$$

with V_c being the Lagrange multiplier for the constraint condition. In the above equation we omit the spin dependence for simplicity. Following a similar procedure to that used for the derivation of the Kohn-Sham Hamiltonian, including the change of basis, the stationary equations of the energy functional W with respect to the conjugated orbitals $\overline{\psi_j}^*$ are given by

$$[H^{KS} + V_c w_c(\mathbf{r})] \psi_i(\mathbf{r}) = \varepsilon_i \psi_i(\mathbf{r}) \tag{4.14}$$

This set of equation has the form of the Kohn-Sham equations except for the additional term $V_c w_c(\mathbf{r})$ that resembles a perturbing potential on the unconstrained system. The stationary equation with respect to the Lagrange multiplier V_c (called in what follows constraining potential) is obtained from the total first derivative of the functional with respect to constraining potential given by

$$\frac{dW}{dV_c} = \sum_i \left(\frac{\delta W}{\delta \psi_i^*} \frac{\partial \psi_i^*}{\partial V_c} + c.c. \right) + \frac{\partial W}{\partial V_c} = 0 \tag{4.15}$$

where *c.c.* stands for the complex conjugate. Using the condition $\frac{\delta W}{\delta \psi_{i\sigma}^*} = 0$ of Eq. 4.14 we finally obtain the stationary equation, which is just the constraint condition,

$$\frac{dW}{dV_c} = \int w_c(\mathbf{r}) n(\mathbf{r}) d\mathbf{r} - N_c = 0. \tag{4.16}$$

The constrained state will correspond to the solution of the stationary equations. These equations (Eqs. 4.14 and 4.16) illustrate how the CDFT method operates to find the constrained state. This is done by adding the appropriate constraining potential (which acts as a perturbation) to the Kohn-Sham Hamiltonian (Eq.

4.14), so that the resulting self-consistent electronic density must satisfy the constraint condition (Eq. 4.16). Since the stationary equations are coupled through the electronic density, they have to be solved iteratively using an optimization technique. Note that for an certain value of the constraining potential, Eq. 4.14 gives a unique set of Kohn-Sham wave functions (electronic density) and eigenvalues once self-consistency is reached. This electronic density implicitly depends on the constraint potential and therefore W is a function of the constraining potential only, $W(Vc)$. To find the extrema of this function as a function of V_c, one has to evaluate its second derivative,

$$\frac{d^2W}{dV_c^2} = \frac{d}{dV_c}\left[\int w_c(\mathbf{r})\rho(\mathbf{r})d\mathbf{r} - Nc\right] \tag{4.17}$$

Using the chain rule, it transforms into

$$\frac{d^2W}{dV_c^2} = \sum_{\sigma}\sum_{i}^{N_\sigma}\int w_c(\mathbf{r})\psi_i^*(\mathbf{r})\frac{d\psi_i(\mathbf{r})}{dV_c}d\mathbf{r} + c.c. \tag{4.18}$$

The term $d\psi_i(\mathbf{r})/dV_c$ can be evaluated using the first-order perturbation theory with $V_c w_c$ being the perturbation of the Kohn-Sham Hamiltonian in Eq. 4.14. Therefore we obtain

$$\frac{d^2W}{dV_c^2} = 2\sum_{\sigma}\sum_{i}^{N_\sigma}\sum_{a>N_\sigma}\frac{|\langle\psi_{i\sigma}|w_c^\sigma|\psi_{a\sigma}\rangle|^2}{\varepsilon_{i\sigma} - \varepsilon_{a\sigma}} \tag{4.19}$$

where the second and third sums go over the occupied and unoccupied Kohn-Sham electronic states of the system, respectively. Analysing the components of the right hand side of the second derivative, we observe that the numerator is positive, but the denominator is negative because the eigenvalues are always lower in energy for the occupied states than for the unoccupied states. Consequently, the second derivative is negative, which means that the functional W has one extrema point that is a maximum. Thus, to obtain the total energy E^{ct} of the constraint system, W should be maximized with respect to the constraint

potential and simultaneously minimized with respect to the electronic density,

$$E^{ct}(N_c) = \max_{V_c} \min_{n} W[n, V_c; N_c] \tag{4.20}$$

In this thesis, we implement the CDFT method proposed by Van Voorhis et. al. and test our implementation with the study of charge transfer reactions considering different systems, as this kind of processes has been extensively studied by Van Voorhis et al. In such reactions, a certain charge N_{CT} is transferred from a group of atoms (or orbitals) of a system that acts as an electron donor, to another group of atoms (or orbitals) of the same system that acts as an electron acceptor. To describe the state of the system with the transferred charge N_{CT}, we have to constrain the charge in the donor and acceptor.
To define the N_{CT}, first we have to define how to assign electrons to an atom or group of atoms in a molecule or solid. This is not straightforward as electrons are shared between atoms forming bonds, causing the fundamental problem of deciding what is the extension of an atom in a molecule or solid. Moreover, the charge on an atom is not an observable in quantum mechanism. In fact, there are many prescriptions to partition electrons among the atoms in a system (all of them physically or chemically motivated), including Mulliken and Löwdin populations, Voronoi charges, and Becke's multicenter integration scheme. While some of these techniques are based on partitioning the charge between the orbitals (such as the Mulliken and Löwdin schemes), others assign charge to spatial regions associated to atoms or molecules in a system (this is the case of the Voronoi charges).
In the next section we will describe the charge assignment we use to study the charge transfer reactions.

4.2.1 Mulliken and Löwdin charges and the weigh function

Although there are several prescriptions to perform the charge distribution between the orbitals, atoms or molecules in a system, none of them allows to assign the charge unambiguously. Here, we focus on the Mulliken and Löwdin popula-

tion schemes as we employ these to define the weight function. In these schemes, the charge is partitioned between the atomic orbitals and therefore the charge assigned to a particular group of atoms is the sum of charge contained in the orbitals that belongs to this group. Within the formalism of local atomic orbitals ϕ_μ, the total number of electrons N in a system can be obtained as the trace of the product of the density $\boldsymbol{\rho}$ and overlap $\mathbf{S}$ matrices, that is,

$$N = Tr[\boldsymbol{\rho}\mathbf{S}] = \sum_{\mu\nu} \rho_{\mu\nu} S_{\nu\mu}. \tag{4.21}$$

with $\rho_{\mu\nu} = \sum_i c_{i\mu} c_{i\nu}^*$ and $S_{\mu\nu} = \langle \phi_\mu | \phi_\nu \rangle$. This equation is easily derived from $N = \int \rho(\mathbf{r}) d\mathbf{r}$ using $\rho(\mathbf{r}) = \sum_i^{occ} |\psi_i(\mathbf{r})|^2$ and expanding the Kohn-Sham wave functions ψ_i in the local basis orbitals.
In the Mulliken population analysis, the number of electrons assigned to a particular orbital ϕ_μ is the value of the diagonal element $(\boldsymbol{\rho}\mathbf{S})_{\mu\mu}$. Consequently, the Mulliken number of electrons N^M associated to a group of atoms C in the system is given by

$$N_C^M = \sum_{\mu \in C} (\boldsymbol{\rho}\mathbf{S})_{\mu\mu} \tag{4.22}$$

For the case of Löwdin populations, one starts from a different but equivalent form to obtain the total number of electrons in the system, given in terms of density matrix and the squared root of the overlap matrix, $\mathbf{S}^{1/2}$:

$$N = Tr[\mathbf{S}^{1/2} \boldsymbol{\rho} \mathbf{S}^{1/2}] \tag{4.23}$$

From this equation, the Löwdin number of electrons N^L associated to a particular group of atoms C is

$$N_C^L = \sum_{\mu \in C} (\mathbf{S}^{1/2} \boldsymbol{\rho} \mathbf{S}^{1/2})_{\mu\mu} \tag{4.24}$$

Similarly to the total number of electron or the charge over a group of atoms, we can define the weight function $w(\mathbf{r})$ within the formalism of the local atomic orbitals (that is, its matrix representation $\mathbf{w}$), using the Mulliken or Löwdin scheme. We start by inserting the expression for the electronic density ($n(\mathbf{r}) =$

$\sum_i^{occ} |\psi_i(\mathbf{r})|^2$) into the Eq. 4.12, obtaining

$$N_C = \sum_i^{occ} \int w(\mathbf{r}) \psi_i^*(\mathbf{r}) \psi_i(\mathbf{r}) d\mathbf{r} \tag{4.25}$$

then, we expand the Kohn-Sham wave functions ψ_i in the local orbital basis,

$$N_C = \sum_i \sum_\mu \sum_\nu c_{i\mu}^* c_{i\nu} \int \phi_\mu^*(\mathbf{r}) w(\mathbf{r}) \phi_\nu(\mathbf{r}) d\mathbf{r} \tag{4.26}$$

where the integral is the definition of the matrix element $w_{\mu\nu}$ of the weight function $\mathbf{w}$.
As a further step, rearranging the order of the sums in the latter equation we get

$$N_C = \sum_\mu \sum_\nu \sum_i c_{i\mu}^* c_{i\nu} w_{\mu\nu}. \tag{4.27}$$

In this equation, for each pair of indexes μ and ν the sum over i gives the density matrix element $\rho_{\mu\nu}$, which is equivalent to $\rho_{\nu\mu}$ since the density matrix is hermitian and real, leading to

$$N_C = \sum_\mu \sum_\nu \rho_{\nu\mu} w_{\mu\nu} = Tr[\boldsymbol{\rho}\mathbf{w}] \tag{4.28}$$

This is just the definition of the constraint condition in the formalism of local bases, that is given as the trace of the product of the density and weight function matrix.
Now, we proceed to define the matrix elements of $\mathbf{w}$ within the Mulliken and Löwdin population schemes. For the Mulliken scheme, each matrix element $w_{\mu\nu}^M$ associated to the orbitals μ and ν, adopts one of the three value given below depending on whether the orbital is inside the constraint domain or not,

$$w_{\mu\nu}^M = \begin{cases} S_{\mu\nu}, & \text{if } \mu \in C \text{ and } \nu \in C \\ \frac{1}{2} S_{\mu\nu} & \text{if } \mu \in C \text{ or } \nu \in C \\ 0 & \text{if } \mu \ni C \text{ and } \nu \ni C \end{cases} \tag{4.29}$$

so that $N_c^M = Tr[\boldsymbol{\rho}\mathbf{w}^M] = \sum_{\mu\in C}(\boldsymbol{\rho}\mathbf{S})_{\mu\mu}$.
In the case of Löwdin populations, by expanding the matrix product of Eq. 4.24 and rearranging the order of the components and sums, we obtain a expression that contains the definition of the weight function implicitly,

$$N_c^L = \sum_{\mu\in C}(\mathbf{S}^{1/2}\boldsymbol{\rho}\mathbf{S}^{1/2})_{\mu\mu} \tag{4.30}$$

$$= \sum_{\mu\in C}\sum_{\nu\lambda} S_{\mu\nu}^{1/2}\rho_{\nu\lambda}S_{\lambda\mu}^{1/2} \tag{4.31}$$

$$= \sum_{\nu\lambda}\rho_{\nu\lambda}\sum_{\mu\in C} S_{\lambda\mu}^{1/2}S_{\mu\nu}^{1/2} \tag{4.32}$$

$$= Tr[\boldsymbol{\rho}\mathbf{w}^L] \tag{4.33}$$

where the matrix elements of $\mathbf{w}^L$ is given by

$$w_{\gamma\nu}^L = \sum_{\mu\in C} S_{\gamma\mu}^{1/2}S_{\mu\nu}^{1/2} \tag{4.34}$$

The definitions given above for the weight function are only valid to study finite systems or periodic systems at Γ point. In this thesis, we proceed to extend the definition of the weight function using Mulliken scheme for k points. It is performed using the overlap and density matrix in the real space where the total number of electrons is obtained as

$$N = \sum_{\mu}^{u.c.}\sum_{\nu}^{sc}\rho_{\mu\nu}S_{\mu\nu} \tag{4.35}$$

here, the first sum runs over all orbitals of the reference unit cell, while the second sum runs over those orbitals that belong to the neighbouring cells that overlap with the orbitals of the reference unit cell. From this definition and following a similar procedure than that used with the Mulliken scheme at Γ point, the constraint condition with k points is given by

$$N_c^M = \sum_{\mu}^{u.c.}\sum_{\nu}^{sc}\rho_{\mu\nu}w_{\mu\nu} \tag{4.36}$$

where the matrix elements of the weight function are

$$w^{M}_{\mu\nu(\nu\equiv\nu')} = \begin{cases} S_{\mu\nu}, & \text{if } \mu \in C \text{ and } \nu' \in C \\ \frac{1}{2}S_{\mu\nu} & \text{if } \mu \in C \text{ or } \nu' \in C \\ 0 & \text{if } \mu \ni C \text{ and } \nu' \ni C \end{cases} \tag{4.37}$$

here, $\nu \equiv \nu'$ stands to indicate that ν' is the equivalent orbital of ν in the unitary cell, and C is the constraint domain. Instead of deriving the Eq. 4.37, we demonstrate that it is totally equivalent to the definition of the Mulliken population of a group of atoms C in the unit cell, which is given by

$$N^{M}_{c} = \sum_{\mu\in C}^{u.c.}\sum_{\nu}^{sc} \rho_{\mu\nu}S_{\mu\nu} \tag{4.38}$$

We start by splitting the first sum of Eq. 4.36 in two: one running over the orbital inside the constraint domain C and the other one going over the orbitals outside this domain.

$$N^{M}_{C} = \sum_{\mu\in C}^{u.c.}\sum_{\nu}^{sc} \rho_{\mu\nu}w_{\mu\nu} + \sum_{\mu\ni C}^{u.c.}\sum_{\nu}^{sc} \rho_{\mu\nu}w_{\mu\nu} \tag{4.39}$$

Then, we divide the second sum of each term on the right hand side of the previous equation, into two components: one of them containing all the elements $\rho_{\mu\nu}w_{\mu\nu}$ where the equivalent orbital of ν in the unit cell, which is named as ν', is inside the constraint region. Thus, the other term should contain all the elements $\rho_{\mu\nu}w_{\mu\nu}$ for which the equivalent orbital of ν in the unit cell is outside the constraint domain, this is,

$$N^{M}_{C} = \sum_{\mu\in C}^{u.c.}\{\sum_{\nu'\in C}^{u.c.}\sum_{\nu\equiv\nu'}^{sc} \rho_{\mu\nu}w_{\mu\nu} + \sum_{\nu'\ni C}^{u.c.}\sum_{\nu\equiv\nu'}^{sc} \rho_{\mu\nu}w_{\mu\nu}\} + \sum_{\mu\ni C}^{u.c.}\{\sum_{\nu'\in C}^{u.c.}\sum_{\nu\equiv\nu'}^{sc} \rho_{\mu\nu}w_{\mu\nu} + \sum_{\nu'\ni C}^{u.c.}\sum_{\nu\equiv\nu'}^{sc} \rho_{\mu\nu}w_{\mu\nu}\} \tag{4.40}$$

Now, we insert the suitable definition for the weight function elements, according to the Eq. 4.37, into each term of the previous equation, getting thus

$$N_C^M = \sum_{\mu\in C}^{u.c.}\sum_{\nu'\in C}^{u.c.}\sum_{\nu\equiv\nu'}^{sc}\rho_{\mu\nu}S_{\mu\nu} + 1/2\sum_{\mu\in C}^{u.c.}\sum_{\nu'\ni C}^{u.c.}\sum_{\nu\equiv\nu'}^{sc}\rho_{\mu\nu}S_{\mu\nu} + 1/2\sum_{\mu\ni C}^{u.c.}\sum_{\nu'\in C}^{u.c.}\sum_{\nu\equiv\nu'}^{sc}\rho_{\mu\nu}S_{\mu\nu} \tag{4.41}$$

Since $\rho_{\mu\nu} = \rho^*_{\nu\mu}$ and real (and similarly for $S_{\mu\nu}$), the third term on the right hand side of the Eq. 4.41 (called β) can be transformed into

$$\beta = 1/2\sum_{\mu\ni C}^{u.c.}\sum_{\nu'\in C}^{u.c.}\sum_{\nu\equiv\nu'}^{sc}\rho_{\nu\mu}S_{\nu\mu} \tag{4.42}$$

Using the following relation $\rho_{\nu\mu} \equiv \rho_{\nu''\mu'}$ (with '$\equiv$' meaning 'equivalent by translation') where ν'' is in the unit cell but out of the constraint region, and μ' is an orbital of the supercell so that its equivalent orbital within the unit cell is in the constraint region, we get

$$\beta = 1/2\sum_{\nu''\in C}^{u.c.}\sum_{\mu''\ni C}^{u.c.}\sum_{\mu'\equiv\mu''}^{sc}\rho_{\nu''\mu'}S_{\nu''\mu'} \tag{4.43}$$

Then, we perform a change of indexes, obtaining thus

$$\beta = 1/2\sum_{\mu\in C}^{u.c.}\sum_{\nu'\ni C}^{u.c.}\sum_{\nu\equiv\nu'}^{sc}\rho_{\mu\nu}S_{\mu\nu} \tag{4.44}$$

Finally, substituting the last term of the right hand side of Eq. 4.41 by the expression of the Eq. 4.44 and adding all terms, we get that Eq. 4.36 is totally equivalent to Eq. 4.38,

$$N_c^M = \sum_{\mu\in C}^{u.c.}\sum_{\nu}^{sc}\rho_{\mu\nu}S_{\mu\nu} \tag{4.45}$$

On the other hand, obtaining the expression for the matrix elements of the weight function with k points within the Löwdin population scheme has some difficulties. One of them is that computing the squared root of the overlap matrix in the real or reciprocal space is not trivial.

4.3 Methodology

To find the maximum of the functional $W(Vc)$ we use the Newton's iterative method. In this method, the maximization of any function with continuous derivatives can be performed employing its first and second derivatives, without evaluating the function itself. The analytical expressions for the first and second derivatives of $W(V_c)$ seem straightforward. However, the evaluation of the second derivative could be computationally demanding as it contains a sum over the unoccupied states. For efficiency, we evaluate numerically the second derivative by calculating the first derivative for two values of the constraining potential. To evaluate the derivatives of $W(V_c)$ at a certain value of constraining potential, we first solve the Eq. 4.14 self-consistently for this constraining potential. Then, the resulting electronic density is used to perform the evaluation of the derivatives.

Unlike the computational algorithm implemented by Van Voorhis et al. to perform the maximization of function $W(V_c)$, in this thesis we code an alternative procedure that describes the physics of the CDFT method accurately. In Fig. 4.1, we compare the algorithm coded by us, with the one followed by Van Voorhis et. al. Basically, in our approach we employ two loops: an outer loop to make the maximization of the function $W(Vc)$ using the Newton's method, and an inner loop to solve the Eq 4.14 self-consistently (for a particular value of constraining potential). By contrast, in the T. Van Voorhis et al. approach these loops are inverted, such that the maximization and the self-consistency are performed in the inner and outer loop, respectively. In our algorithm (diagram on the left in the Fig. 4.1), we first declare the initial CDFT variables (apart from those required for a standard DFT calculation) in a input file, including the initial constraint potential V_c, the orbital set of the acceptor and donor, the charge to be transferred between the donor and acceptor (this is defined through N_c as will be discussed in Sec. 4.2.1), the population scheme to compute the weight function w, and the tolerance criteria for the first derivative of W. Optionally, we can declare the step length for the constraint potential to estimate the second derivative (its default value is of 1.0×10^{-4} Ry). Then, SIESTA computes the elements of the weight function matrix $\mathbf{w}_c$. $\mathbf{w}_c$ only depends on $S_{\mu\nu}$, so it can

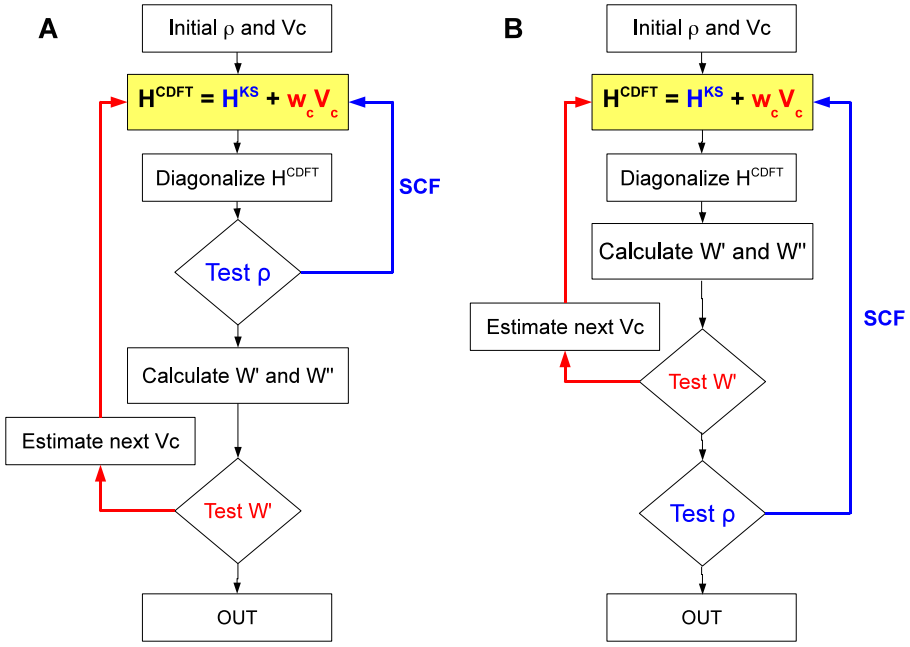

Figure 4.1: Comparing the algorithm implemented by us (A) with the one used by T. Van Voorhis et al. (B). The standard self-consistency loop is indicated by the blue arrow.

be calculated once and kept fixed during the whole CDFT calculation. Next, the outer loop (the maximization of $W(V_c)$) is initialized by adding the elements $V_c w_{ij}$ (where V_c is the initial constraining potential) to the corresponding standard Kohn-Sham Hamiltonian matrix elements H_{ij} calculated previously. The resulting constrained Hamiltonian is solved self consistently (as usual in a standard DFT calculation) in the inner loop until the convergence of the electronic density is reached. During self-consistency the constraining potential V_c remains constant. Once self-consistency is reached, we leave the inner loop and go to the next step of the outer loop that consists in evaluating the first and second derivative of W using the converged electronic density. Then, we compare the value obtained for the first derivative with the predefined tolerance value. If the first derivative does not satisfy the convergence criteria, we estimate a new value for the constraint potential by performing a step of the Newton's method. The new constraint potential together with the last converged density matrix are then

used to reinitialize the outer loop (by constructing a new constrained Kohn-Sham Hamiltonian) and perform the procedure again. We repeat the whole procedure until the first derivative satisfies the convergence criteria, which would mean that the maximum of W has been found. Once the maximum is found, SIESTA computes the charge populations on the donor and acceptor using either the Mulliken or Löwdin population scheme, and the other quantities of a standard DFT calculation: forces, total energy, etc.

This is to be compared with the T. Van Voorhis et al. approach (diagram on the right in the Fig. 4.1), where the loops are inverted and the function $W(V_c)$ is maximized in each step of the self consistency. To be specific, the outer loop is initialized by constructing the constrained Hamiltonian (this is done, as in our case, by adding elements $V_c w_{ij}$ to the standard Kohn-Sham Hamiltonian). Then, we move to the inner loop where this Hamiltonian is diagonalized and with the resulting electronic density the first derivatives of W are evaluated. Next, we test the convergence of the first derivative. If the first derivative does not satisfy the convergence criteria a new value for the constraint potential is estimated. Then, the V_c in the constrained Hamiltonian is replaced by the new estimated value, while the terms of the Hamiltonian that depend on the density matrix are maintained constant. As the next step, the resulting Hamiltonian is diagonalized again. This procedure is repeated several times until the first derivative satisfies the convergence criteria. Once the convergence is reached, we leave the inner loop and go to the next step of the outer loop consisting in testing the convergence of the electronic density obtained in the last diagonalization. If the electronic density does not satisfies the convergence criteria, we proceed to rebuild the constrained Hamiltonian using this electronic density and the last value of constraining potential calculated (in this step all the terms of the Hamiltonian are updated). Then, we reinitialize the outer loop and repeat the procedure again. This is done repeatedly until the convergence of the electronic density is reached.

Comparing both approaches, we observe that the algorithm implemented by T. Van Voorhis et al. is not the most appropriate to perform the maximization of the function $W(V_c)$, because they employ a non-self-consistent solution of the constrained Kohn-Sham Hamiltonian (which is not the correct solution of Eq. 4.14) to compute the derivatives of the function W. They make it in each step

of the inner loop. As stated in the derivation of the method, for a certain value of the constraint potential the correct solution of the stationary equation 4.14 (the constrained Kohn-Sham Hamiltonian) is obtained by self consistency and this is just what we do within our approach. Although the procedure followed by Van Voorhis et al. can lead to a reduction of the computational cost since in each step of this loop they update the constraint potential in the Hamiltonian, but not the terms depending on the electronic density (building these terms is computationally expensive), there is no theoretical justification to do it.
Using our algorithm, the number of steps needed in the outer loop to converge the first derivative of $W(V_c)$ depends on whether or not the initial value of constraint potential is close to the value that gives the constrained state. Similarly, for the inner loop the number of steps required for reaching self-consistency is determined by the input density matrix. Among these critical quantities, the input constraining potential is the most crucial because an initial value too far from the value that gives the maximum yields large fluctuations not only in the constraint potential but also in the electronic density during the maximization.

4.4 Validation of the method

In the present work, we study charge transfer reactions in several systems, ranging from molecules to periodic solids. With the purpose of testing our method, we take some systems studied by Van Voorhis et al. in Refs. [4, 5] where they reported their approach. We compare our results with those obtained by them from a qualitative as well as quantitative perspective.
To study this sort of reactions, instead of using two constraints: one to describe the charge of the donor and the other one to represent the charge of the acceptor, we define only one constraint as the charge difference between the donor and the acceptor, N_C, that is,

$$N_C = \frac{N_A - N_D}{2} \tag{4.46}$$

where N_A and N_D stand for the charge population of the acceptor and donor, respectively.
The first system considered is a nitrogen molecule N_2 where we study the charge

transfer between the nitrogen atoms, using the Mulliken as well as Löwdin population schemes to represent the weight function. One of the nitrogen atoms acts as an electron donor and the other one as an electron acceptor. Initially, each isolated nitrogen atom contributes with 5 valence electrons (with an electronic configuration: $2s^2 2p^3$) to form the molecular nitrogen. Analysing the electron populations in the ground state from mean field in the nitrogen molecule using either the Mulliken or Löwdin population, the distribution of the valence electrons between the atoms is always balanced (that is, 5 electrons in each atom). Starting with this distribution, we proceed to constrain the electronic density to force the charge transfer, in the range of 0 to 1.0 electrons, from one of the nitrogen atoms to the other one. Our results are presented on the left hand side of Fig. 4.2, where we also compare them with those from T. Van Voorhis et al., shown on the hand right side of the same figure. To be able to compare both

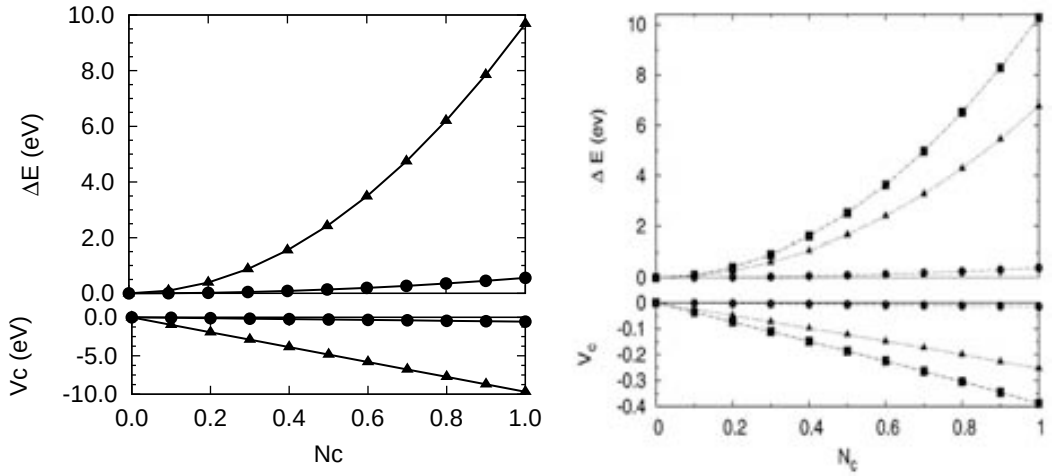

Figure 4.2: Charge transfer in a nitrogen molecule N_2. We compare our results with those obtained by Q. Wu and T. Van Voorhis [5]. The lower graphs shows the constraint potential as a function of the charge transfer, which ranges from 0 to 1.0 electron. The upper graphs presents the energy difference between the charge transfer and DFT ground state energy ($\Delta E = E^{CDFT} - E^{DFT}$), as a function of the charge transfer. Different population schemes to define the weight function w_c were used. Triangles: Mulliken population. Dots: Löwdin population. Q. Wu and T. Van Voorhis additionally used the Becke weights population (squares).

methods, we consider total energy differences because in this way we do not have

the problem of the reference potential. In the upper left panel, we plot the total energy difference between the charge transfer and the ground state, versus the transferred charge, and in the lower left panel we plot the constraining potential that gives the corresponding charge-transfer state. We compute charge populations (either the Löwdin or Mulliken) to evaluate how the charge is distributed between the atoms in the constrained state.

We notice that although our results have a similar behaviour to those obtained by Van Voorhis et al., our values of energy are, in general, larger. This situation is attributed to two aspects: 1) we use the standard PBE functional versus the Becke's hybrid functional employed by Van. Voorhis et al., and 2) our basis sets are built from strictly localized atomic orbitals, whereas they use the basis sets made from Gaussian functions.

We observe that the energy differences with the Mulliken populations do not change too much as the amount of transferred charge increases in comparison with the energy differences obtained using the Löwdin scheme. This unusual behaviour of the Mulliken populations is explained by Van Voorhis et al. considering that they are not defined by a projection operator (sometimes the evaluation of the Mulliken population gives negative values). Notice that the constraining potential that gives the constrained state is too small (acting as a perturbation in the Kohn-Sham Hamiltonian) and therefore it leads to small changes in the excitation energies (defined as the difference between the constrained and ground-state energies).

Using the Löwdin population scheme, we observe large variations in the total energy differences against the fraction of transferred charge. This fact is also reflected in the corresponding values of constraint potential. When one electron is transferred, the energy difference is 9.5 eV (with the corresponding constraint potential being of 9.52 eV), which is 2.5 eV larger than the value obtained by Van Voorhis et al. Unlike Mulliken populations, Löwdin populations seem to give larger excitation energies. This is in good agreement to what Van Voorhis et al. obtained.

To have a picture of the electronic density of the nitrogen molecule with and without the constraint, in Fig. 4.3 we show an isosurface for a) the ground state, n^{DFT}, and b) with the constraint corresponding to the transference of one elec-

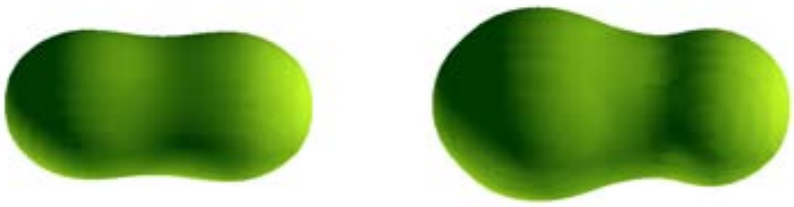

Figure 4.3: Isosurface of the ground and constrained states.

tron, n^{CT}. In the ground state, the electronic density is symmetrically distributed, whereas in the constrained state, the electronic density is displaced towards the atom with the extra electron, indicating that the constraint is correctly imposed. Additionally, we plot the difference between the electronic density of the ground and constrained state, $\Delta n = n^{CT} - n^{DFT}$, see Fig. 4.4, where the blue and red isosurfaces stand for positive and negative differences, respectively, indicating that electron transfer occurs as these coloured isosurfaces are localized on different nitrogen atoms. However, these coloured regions are not completely symmetric to each other, which could seem contradictory at a first moment. The explanation for this effect is that the total potential experienced by the electrons in the constrained system varies from the nitrogen atom acting as electron acceptor to the nitrogen one acting as electron donor because the electronic density in both atoms is different.

To further test our approach, we proceed to consider a larger system, the zincbacteriochlorin-bacteriochlorin (ZnBC-BC) complex, where we investigate the charge transfer between ZnBC and BC parts of the complex, which are linked through a benzene ring as depicted in Fig. 4.5, using again the Mulliken and Lowdin population schemes. Considering that these parts are chemically distinct, we study the electron transfer not only from ZnBC to BC but also in the opposite direction, defining $N = 1.0$ for $(ZnBC)^{1+} - (BC)^{1-}$ and $N = -1.0$ for $(ZnBC)^{1-} - (BC)^{1+}$, with N being the charge transfer. Our results are pre-

Figure 4.4: Charge transfer in a nitrogen molecule N_2. Difference between the charge transfer (n^{CT}) and ground state (n^{DFT}) electronic density. The blue and red isosurfaces indicate a negative and positive difference, respectively.

sented on the right side of Fig. 4.6, together with the results obtained by T. Van Voorhis et al. (shown on the left side). Both results are quite similar, particularly the values of the total energy differences, even though the functionals and kind of basis sets used are also different (see figure caption for details). However, the constraining potential is not comparable. Strictly speaking, they are not expected to be the same, since the Hamiltonians are built using different parameters. These results are good qualitative signs regarding the performance of our approach.

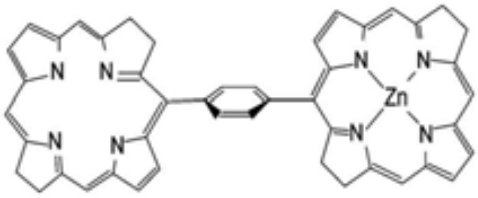

Figure 4.5: ZnBCBC complex.

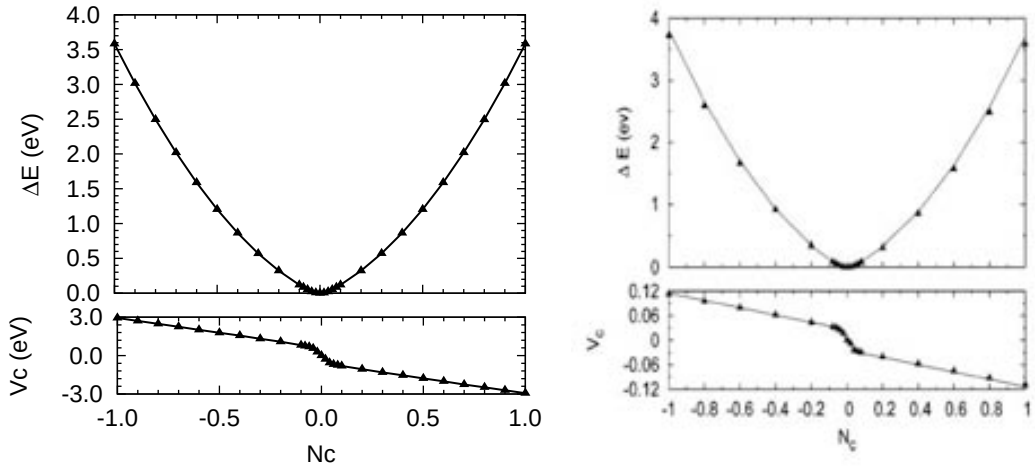

Figure 4.6: Charge transfer in the ZnBC-BC molecule. We compare our results with those obtained by Q. Wu and T. Van Voorhis [5]. The lower graphs shows the constraint potential as a function of the charge transfer, which ranges from 0 to 1.0 electron. The upper graphs presents the energy difference between the charge transfer and DFT ground state energy ($\Delta E = E^{CDFT} - E^{DFT}$), as a function of the charge transfer. We use different population schemes to define the weight function w_c: Mulliken (triangles) and Löwdin (circles) population.

Now, let us discuss some aspects related with the efficiency of our method to find the maximum of the function W. We observe that in general a small number of steps are needed in the outer loop to reach the convergence of the first derivative (typically 4 steps are enough), even when the initial guess value of the constraint potential is quite far from the correct value at which the functional W has the maximum. In the inner loop, we found that the number of steps is similar to that of a standard DFT calculation, even though this loop depends on both the magnitude of the constraining potential added to the Kohn-Sham Hamiltonian and initial electronic density.
The results shown until now prove that our approach can reproduce satisfactorily the results reported by Van Voorhis et al. However, the need of a quantitative test to proof unambiguously that our method works correctly, is still needed. For this, we study the charge transfer between two nitrogen molecules separated by a distance d, such that the N-N bond of the nitrogen molecules is perpendicular

to the separation direction. We employ a tetragonal supercell with $a = b = 20\mathring{A}$ and $c = 30\mathring{A}$, in which the separation between the nitrogen molecules is along the c direction. Thus, we compute the energy $E^{CT}(d)$ of the system with the transferred charge (one electron) for different separation distances d. Then, the resulting energies $E^{CT}(d)$ are adjusted to the following model equation describing the total energy of two opposite charges separated by a distance d,

$$E^{CT}(d) = -\frac{1}{d} + E^{CT}(\infty) \tag{4.47}$$

where $E^{CT}(\infty)$ is the energy of the charge-transfer state where the nitrogen molecules are separated by an infinite distance. Alternatively, the $E^{CT}(\infty)$ can be calculated from a standard DFT calculation since it corresponds to the sum of the total energies of a nitrogen molecule with positive and negative net charge: $E^{CT}(\infty) = E^{DFT}_{N_2^+} + E^{DFT}_{N_2^-}$. Hence, the quantitative test consists in calculating $E^{CT}(\infty)$ using the CDFT and DFT methods and comparing the obtained values to each other.

To obtain $E^{CT}(\infty)$, the total energy of charged molecules is calculated in SIESTA using periodic boundary conditions (PBC) and the convergence of this energy with the size of the cell has to be adequately described. We use a model to obtain the total energy of the charged system in the limit of a infinitely large cell. Basically, the convergence problem arises from the divergence of the Coulomb potential for charged systems due to the pbc and from the resulting interaction between the charged system and its periodic images. To deal with these situations, SIESTA introduces a neutralizing background charge to make the system overall neutral (this procedure was initially introduced by Makov-Payne [55]), however, there are still some interactions between the periodic charges and itself that remains. These interactions become negligible at the limit of a infinitely large cell, however, a fast convergence of the Coulomb energy with the cell dimension L is not guaranteed. Hence, we employ the following equation

$$E(L) = E_0 - \frac{q^2\alpha}{2\varepsilon L} + O(L^{-3}) \tag{4.48}$$

which allows to obtain the DFT total energy of a charged system E_0 in the limit

of an infinitely large supercell ($L \to \infty$). The first correction term contains the charge of the cell q, the Madelung constant α that is dependent of the cell size and shape and the static dielectric constant of the medium ε. Calculations for several system sizes (including the Madelung correction term) allow us to extrapolate to the limit of large cell sizes by fitting the $1/L^3$ dependence, thus minimizing the spurious effect of the neutralizing background.

We obtain E_0 ($\equiv E_{N^{\pm}}^{DFT}$) for the negatively and positively charged nitrogen molecule by making a fit of the DFT total energy $E(L)$ of the charged nitrogen molecule (whether +1 or -1) for different cell dimensions L, to the above equation. As our system is a molecule, we employ a cubic supercell, for which the Madelung constant is well defined in SIESTA. Thus, the value of $E^{CT}(\infty)$ from the DFT is -1084.95 eV.

In the Fig. 4.7, we present the results from CDFT concerning the fit the total energies $E^{CT}(d)$ of the final charge transfer state for different values of d to the Eq. 4.47.

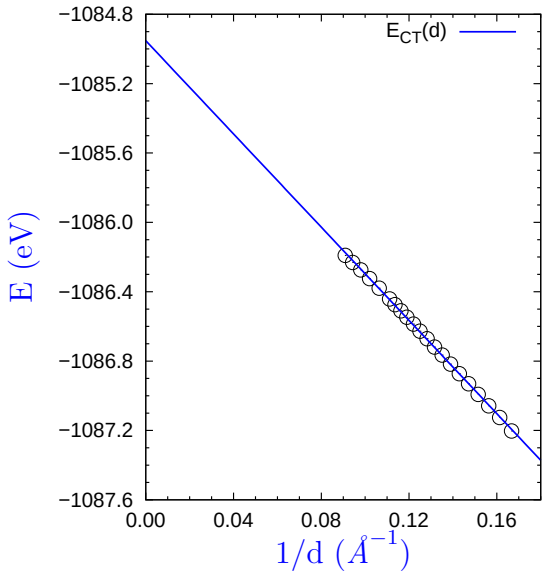

Figure 4.7: Charge transfer of one electron between two nitrogen molecules N_2 separated by a distance d. The total energy $E^{CT}(d)$ (blue circles) of the final charge transfer state for different values of d are plotted against $1/d$. The red line is the fit of the $E^{CT}(d)$ to the Eq. 4.47, where $E^{CT}(\infty)$ has a value of -1084.86 eV

Comparing the values of $E^{CT}(\infty)$ obtained from DFT and CDFT method, we find a difference between them of 0.1 eV. This difference is small enough to conclude that our approach has been well implemented and that it works correctly. Additionally, we think this difference could be decreased for larger supercell in the CFDT method to reduce the interaction between the electric dipoles formed as result of the charge transfer.

4.5 Application: TTF-TCNQ

The good results obtained in the previous section encouraged us to apply our method to a more practical problem. We study the organic charge-transfer salt TTF-TCNQ (a prototypical one-dimensional conductor), which is formed from

segregated chains of stacking TTF and TCNQ molecules. The interesting properties of this material as a conductor are not of a molecular origin but arise from the interaction of adjacent TTF and TCNQ chains in the crystal. Many theoretical and experimental studies have focused in the understanding of the physics behind its unidimensional metallic behaviour. The experimental characterization of its surface with the x-ray photoemission and x-ray absorption near edge spectroscopes (XPS and XANES, respectively), have revealed several features whose origin has not been totally understood [7, 8]. Claessen et al. [8] observed new interesting characteristics in the XPS spectra of this material that were assigned to two coexisting electronic states: the TTF^0-$TCNQ^0$ and TTF^{+1}-$TCNQ^{-1}$. They suggest that these states are originated due to a charge transfer between the TTF and TCNQ chains.

Fig. 4.8 shows the unit cell of the TTF-TCNQ crystal together with a representation of the TTF ($C_6H_4S_4$) and TCNQ ($C_{12}H_4N_4$) molecules. TTF-TCNQ crystallizes in a monoclinic structure (space group $P2_1/c$) with the experimental lattice parameters being $a = 12.298\mathring{A}$, $b = 3.819\mathring{A}$, $c = 18.468\mathring{A}$, and $\beta = 104.46$. The unit cell contains two molecules of TTF and two molecules of TCNQ. In the crystal phase the chains of TTF and TCNQ alternate along the **a** direction, being **b** the stacking direction. The interaction between the TTF and TCNQ chains leads to a partial electron transfer from the TTF to TCNQ molecules (of about 0.49 electrons in mean field) that is observed in our calculated results for the band structure shown in Fig. 4.9. Focusing on the high symmetric directions going from $\mathbf{\Gamma}$ to $\mathbf{Y}$ of the first Brillouin zone, there are four bands (a and b in Fig. 4.9) around the Fermi energy level and two of them cross at a certain point along this direction. The character of the two bands (a) come mainly from the TTF molecules, while the two bands (b) have a strong character from the TCNQ molecules. Thus, the crossing point is due to the partial charge transfer between the TTF and TCNQ molecules. The relation between the transferred charge and the crossing point in the band structure is defined by the fact that each band can be filled with a maximum of two electrons (two opposite spins). Since there is no crossing bands at the Fermi energy level along the other symmetric directions of the first Brillouin zone, this material is classified as an unidimensional conductor.

Figure 4.10 shows XPS spectra of S 2p and N 1s core levels of TTF-TCNQ

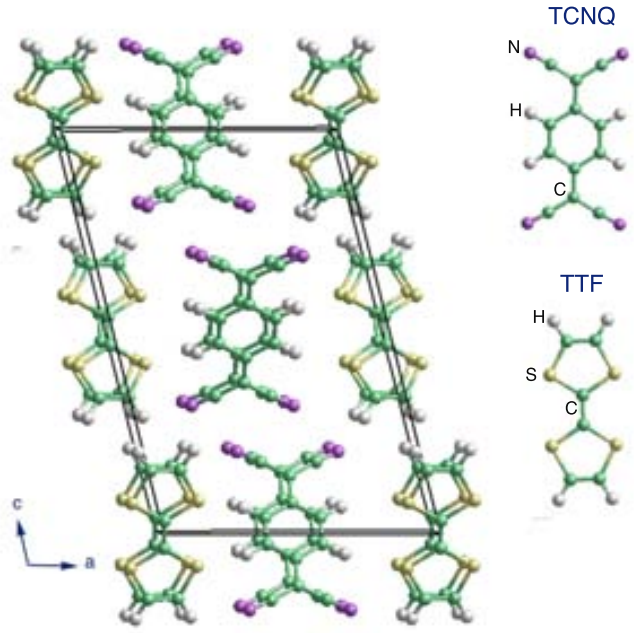

Figure 4.8: Unit cell of the TTF-TCNQ crystal.

crystal measured by Claessen et al. The S and N atoms are specific of TTF and TCNQ molecules, respectively, and therefore their corresponding XPS spectra provide characteristic information concerning the physical and chemical properties for each of these molecules in the crystal. Among the main results obtained by these authors, we mention that: 1) There are clearly two distinct S atoms in the system with S 2p core level binding energies of 163.8 and 164.8 eV (each of them with their corresponding spin-orbit splitting). 2) They also found two types of N atoms with N 1s core level binding energies of 398.0 and 399.5 eV (and they are accompanied by satellites appearing at higher binding energies). 3) The intensity ratios between the lower- and the higher binding energy peaks for the S 2p and N 1s core levels are 0.44:0.56 and 0.65:0.35, respectively. Considering the position of the binding energy peaks and the intensity ratios of the main features observed in the S 2p and N 1s spectra, these authors suggest that charge fluctuations happen in the system (which have smaller lifetimes than the photoemission processes) leaving the TTF and TCNQ molecules in a mixed valence. Moreover,

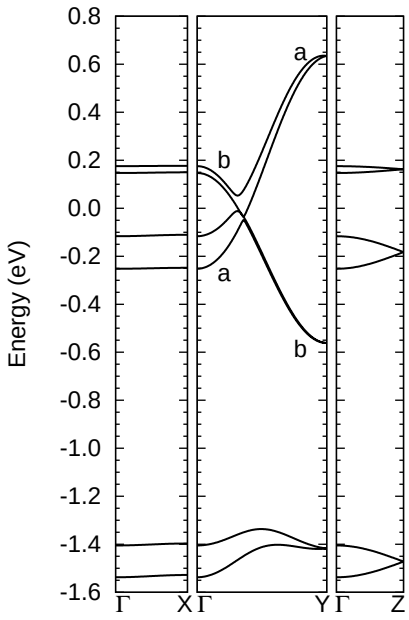

Figure 4.9: Band structure for the room temperature and ambient pressure structure of TTF-TCNQ, calculated using the GGA exchange-correlation functional and the PBE flavour. The Fermi energy level is set to 0 eV. $\Gamma = (0, 0, 0)$, $X = (1/2, 0, 0)$, $Y = (0, 1/2, 0)$, and $Z = (0, 0, 1/2)$ in units of the monoclinic reciprocal lattice vector.

they propose that the charge fluctuations are due to the continuous transition between the $TTF^0 - TCNQ^0$ and $TTF^+ - TCNQ^-$ states. Additionally, they suggest that due to the less effective screening of the core potential, the TTF^+ state should show up in the S 2p spectrum at higher binding energies compared to the neutral chemical state, whereas for the $TCNQ^-$ state and the N 1s line the reverse should happen.

In this thesis, we intend to contribute to the description and characterization of the electronic properties observed at the surface of the TTF-TCNQ system. For that, we use our CDFT approach to create the electronic states proposed by Claessen et al. and study the core level binding energies

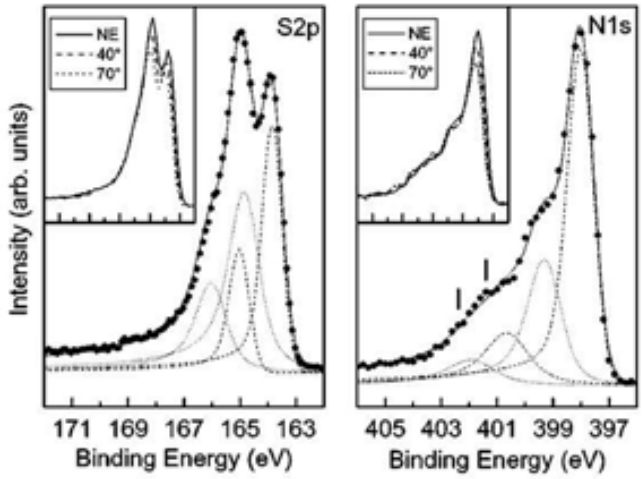

Figure 4.10: XPS spectra of S 2p and N 1s core levels of TTF-TCNQ (dots). The lines represent decompositions unto underlying components obtained by a least-squared fit. For details see the text. Insets: XPS spectra of the S 2p and N 1s core levels as a function of emission angle (NE, 40^o off NE, 70^o). Note that the binding energy scale is the same as in the parent plot.

4.5.1 Results

To study the S 2p and N 1s CLBE shifts in TTF^0-$TCNQ^0$ and TTF^+-$TCNQ^-$, we first apply our CDFT approach with the Mulliken scheme and **k** points to create these states. Then we compute the CLBE shifts for these states with the initial and ΔSCF approximation.

In the ground state calculation (where there is no constraint upon the system), each TCNQ molecule has an extra charge of 0.49 electrons coming from the TTF molecules. We use this state as starting point to obtain the TTF^0-$TCNQ^0$ and TTF^+-$TCNQ^-$ states. For the neutral state, we impose a constraint upon the whole TTF-TCNQ unit cell (which contains four molecules: two of TTF and two of TCNQ) to force the charge transfer (of 0.49 electrons) from each TCNQ to the TTF molecules, so that in the constrained neutral state the Mulliken populations of the TTF and TCNQ molecules are 52.0 and 72.0 electrons, respectively.

We consider three different models to describe the TTF^+ and $TCNQ^-$ states in the TTF-TCNQ unit cell, using the TTF^0-$TCNQ^0$ as the reference system. In

the first model we impose a constraint such that one of the TTF molecules has a positive charge of +1.0 (a Mulliken population of 51.0), and the rest of TTF and TCNQ molecules get a total negative charge of -1.0. That is, we transfer one electron from the TTF molecule to the rest of the system (neighbouring molecules in the unit cell). This model is denoted as TTF^{+}-$(TTF\text{-}2TCNQ)^{-}$. In the second model a constraint is imposed so that one of the TCNQ molecules of the unit cell gets a extra charge of one electron from the rest of TCNQ and TTF molecules. This model is labelled as $TCNQ^{-}$-$(TCNQ\text{-}2TTF)^{+}$. Finally, in the last model, a constraint is applied to transfer a charge of one electron from each TTF molecule to the TCNQ molecules in the unit cell, leading to TTF^{+}-$TCNQ^{-}$ pairs in the whole crystal. This model is denoted as $(2TTF)^{+2}$-$(2TCNQ)^{-2}$ since there are four molecules per unit cell. Also we consider the neutral states: TTF^{0}-$(TTF\text{-}2TCNQ)^{0}$, $TCNQ^{0}$-$(TCNQ\text{-}2TTF)^{0}$ and $(2TTF)^{0}$-$(2TCNQ)^{0}$.
Table 4.1 shows the Mulliken population analysis of the TTF and TCNQ molecules in the different models considered. It also includes the Mulliken population of the ground state and neutral states corresponding to each model. In the models

Table 4.1: Mulliken population analysis of the TTF and TCNQ molecules in the TTF-TCNQ unit cell with different constraints on its electronic density. We use the labels -a and -b to distinguish each of the TTF and TCNQ molecules in the unit cell.

System	TCNQ-a	TCNQ-b	TTF-a	TTF-b
Ground state	72.492	72.492	51.516	51.516
$TCNQ^{0}$-$(TCNQ\text{-}2TTF)^{0}$	72.0	72.512	51.872	51.620
$TCNQ^{-}$-$(TCNQ\text{-}2TTF)^{+}$	73.0	72.464	51.132	51.404
TTF^{0}-$(TTF\text{-}2TCNQ)^{0}$	72.308	72.432	52.004	51.259
TTF^{+}-$(TTF\text{-}2TCNQ)^{-}$	72.679	72.540	51.008	51.778
$(2TTF)^{0}$-$(2TCNQ)^{0}$	72.0	72.0	52.0	52.0
$(2TTF)^{2+}$-$(2TCNQ)^{2-}$	73.002	73.004	51.0	51.0

where we impose a constraint between a molecule of the unit cell, whether TTF or TCNQ, and the rest of the system, the Mulliken population analysis of the TTF or TCNQ molecule gives the correct charge for both the neutral and charge-transfer state. For the rest of molecules the total Mulliken charge population is

the right one, however, the distribution of charge between them follows the mean field solution. We observe that in these molecules the charge populations of the molecules of the same type are slightly different. These variations are due to their proximity to the TTF or TCNQ molecule where we impose a charge of +1 or -1, respectively. In the model where we impose a constraint to transfer charge between all the TTF and TCNQ molecules, the Mulliken population analysis gives the correct charge for each molecule in the unit cell in both the neutral and the charge transfer state. In all cases, the charge transfer occurs mainly between the atoms of the donor and acceptor that are adjacent.

These results confirm that our CDFT approach with the Mulliken scheme performs the constraint correctly as it gives the correct Mulliken populations in the constrained system.

Figure 4.11 depicts the band structure of the TTF-TCNQ unit cell with a constraint on its electronic density such that all TTF and TCNQ molecules are in the neutral state (panel on the left side), and with a constrained electronic density that gives the charge transfer state TTF^{+}-$TCNQ^{-}$ where an electron is transferred from each TTF molecule to its closest neighbouring TCNQ molecule (panel on the right side). Although the Mulliken population analysis gives correct charges for the TTF and TCNQ molecules in the neutral and charged state, no significant differences are observed between the band structures of these states. Moreover, we do not see any charge transfer between the bands that cross the Fermi energy level along the symmetric direction going from $\mathbf{\Gamma}$ to $\mathbf{Y}$ of the first Brillouin zone (FBZ), which remain unchanged. Apparently, the transferred charge between the TTF and TCNQ molecules does not lead to a transfer charge from bands of the HOMO to bands of the LUMO molecular orbital in the system. The constraining potentials that give the constrained and neutral state are found to be quite small, as we also found with the nitrogen molecule. This is a typical problem for the constraints using the Mulliken populations.

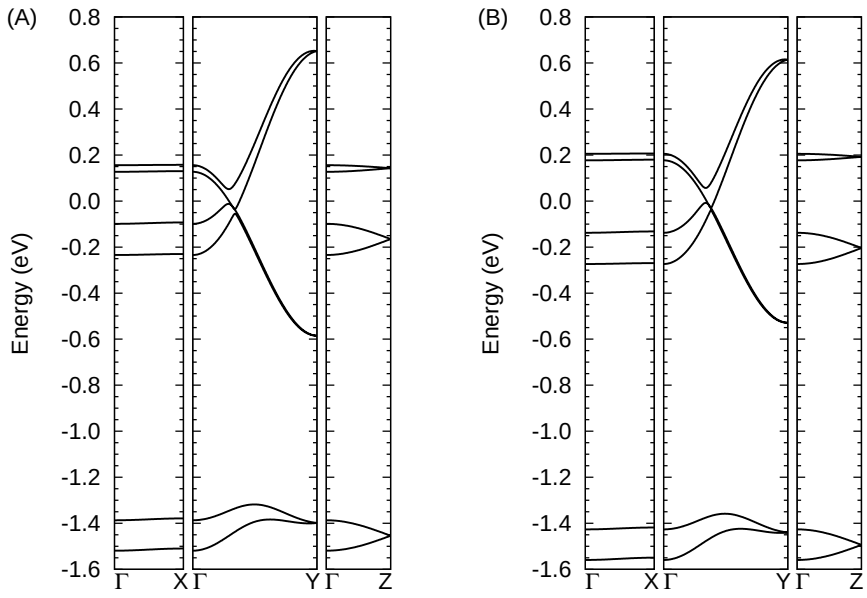

Figure 4.11: Band structure of TTF-TCNQ in the ground (a) and constrained (b) state.

To further ensure that the constrained states are calculated correctly with **k** points, we impose a constraint on the electronic density of a simpler system consisting of TTF and TCNQ chains separated by a large distance, such that the interaction between the TTF and TCNQ molecules is negligible. For this model, our *a priori* assumption is that in the mean field approximation the TTF and TCNQ bands near the Fermi energy level and along the **Γ**-**Y** direction in the FBZ, do not intersect each other. Figure 4.12 shows the band structure from mean field calculation for this model. The Fermi energy level is at zero. Clearly, along the **Γ**-**Y** direction of the FBZ a band appears above the Fermi energy level, while another band is below this level. These bands touch at Γ point. We investigate the character of these bands, finding that the unoccupied band comes from the LUMO of the TCNQ and the occupied band from the HOMO of the TTF molecules. We then proceed to impose a constraint on this system to obtain the charge transfer state where each TTF molecule donates one electron to the TCNQ molecules, creating the charge state TTF^{+}-$TCNQ^{-}$. Figure 4.12 (b) shows the band structure of the system with the constraint. We see that at the Fermi en-

ergy level the TTF and TCNQ bands intercept just in the middle of the distance between **Γ** and **Y** points of the FBZ. Considering that each band accommodates two electrons (we are not considering spin polarization in the calculation), the crossing point of these bands clearly indicates that one electron is transferred from the HOMO band of the TTF molecules to the LUMO band of the TCNQ molecules, resulting in the formation of the TTF^{+}-$TCNQ^{-}$ constrained state. We verify this results by calculating the Mulliken populations. This results confirms that our CDFT approach with **k** points makes the charge separation correctly.

To understand why we do not observe a charge transfer between bands in the

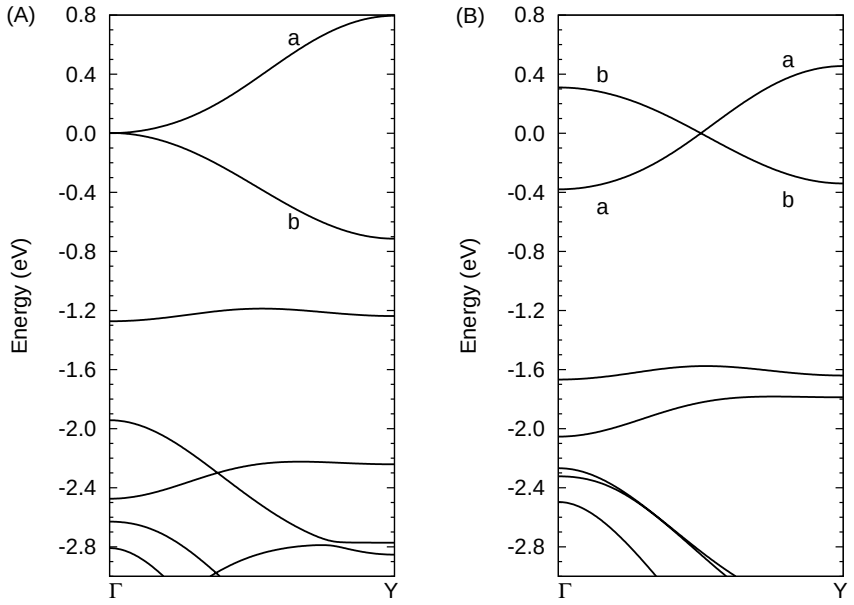

Figure 4.12: (A) Band structure from mean field for model of TTF and TCNQ chains. In this model, the TTF and TCNQ chains alternates along the x-axis (the separation distance between the chains is 20.0 $\mathring{A}$), with the staking direction being the y-axis. The separation distance along the z-axis is 25.0 $\mathring{A}$. All bands are relative to the Fermi energy level set to zero. (B) Band structure for the model of TTF and TCNQ chains with a constraint on its electronic density that gives the charge state TTF^{+}-$TCNQ^{-}$. All bands are relative to the Fermi energy level set to zero.

band structure of the TTF-TCNQ crystal although the Mulliken population indicates that the charge transfer occurs, we analyse the electronic density difference between the neutral and charged state, comparing it with the HOMO and LUMO

orbitals of the isolated TTF and TCNQ molecules, respectively. We make this comparison assuming that the highest energy occupied molecular orbital of the TTF-TCNQ crystal is somewhat similar to the highest molecular orbital of an isolated TTF molecule, and that the lowest energy unoccupied molecular orbital of the crystal is similar to the lowest energy unoccupied molecular orbital of an isolated TCNQ molecule. The difference between the neutral and charged electronic density is displayed on Fig. 4.13.

We observe that the atoms of the TTF molecules closer to the neighbouring TCNQ molecules are the donor of charge: the S atoms and two of the four hydrogen atoms of each TTF molecule. Furthermore, a small contribution comes from the bond formed by two of the C atoms that connect the tiol rings in the TTF molecule. The charge difference around the TTF molecules in the crystal is similar to the charge distribution in the HOMO orbital of the isolated TTF molecule, except for the contributions around the hydrogen atoms. Additionally, there is charge in some C atoms of the HOMO orbital of the isolated molecule that does not appear in the TTF molecules of the crystal.

In the case of charge accepted by the TCNQ molecules, this is mainly distributed between the atoms that are closer to the neighbouring TTF molecules. The atoms are all the hydrogen and nitrogen atoms of each TCNQ molecule (mostly the charge is distributed between the N atoms), but also a fraction of the transferred charge is spread between two of the C atoms that are linked to the aromatic ring and to the -C-N radicals. This charge distribution in the TCNQ molecules is considerably different to the charge distribution in the LUMO orbital of the isolated TCNQ molecule, as shown in the Fig. 4.14.

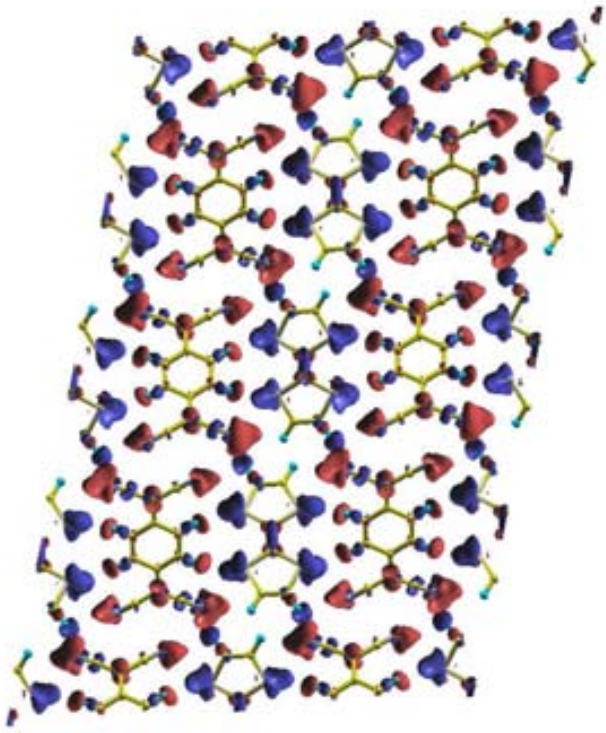

Figure 4.13: Electronic density difference $\Delta\rho$ between the neutral (TTF^0-$TCNQ^0$) and charged state (TTF^+-$TCNQ^-$): $\Delta\rho = \rho(TTF^+ - TCNQ^-) - \rho(TTF^0 - TCNQ^0)$. The picture shows isosurfaces with a positive (red) and negative (blue) difference.

These results show that imposing the constraint on the electronic density through the local basis set (the atomic orbitals of the atoms) leads to a charge transfer between the TTF and TCNQ molecules. However, this charge transfer does not take place from the highest occupied to lowest unoccupied band, because these bands do not experience a noticeable change when the constraint is applied. This is not what we expected. Our hypothesis to explain how the electronic state are formed is that the charge transfer between the TTF and TCNQ molecules occurs between the TTF and TCNQ bands next to the Fermi energy. Instead, that there is a small variation in the character of the whole set of occupied bands, so that this leads to the TTF^+-$TCNQ^-$ state. Therefore, our approach

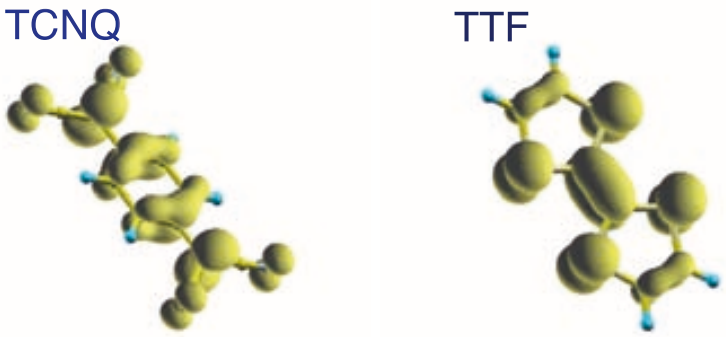

Figure 4.14: Isosurface of the electronic density of the LUMO orbital of a isolated TCNQ. Isosurface of the electronic density of the HOMO orbital of a isolated TTF molecule.

consisting in imposing the constraint through the atomic orbitals to describe the charge-transfer state is not the most adequate. A different approach to describe the charge transfer based on imposing a constraint through the molecular wave functions of the highest occupied and lowest unoccupied bands to force the direct charge transfer between these bands could be needed.

Chapter 5

Anatase

5.1 Introduction

In the last years (TiO_2) anatase has been extensively studied both theoretically and experimentally because of its promising applications in semiconductor-based photocatalysis for the degradation of organic molecules in water and air purification, and solar cells and photovoltaic devices [9, 10, 11, 56]. Its main advantages over similar materials are its high resistance to photo- and chemical corrosion and high oxidizing power. However, its main drawback is its large band gap of 3.0-3.2 eV which falls in the ultraviolet region of the electromagnetic spectrum. In order to improve its electronic properties, a large number of attempts have been focused to lower its band gap and turn it active under visible light ($\lambda > 380$ nm). The reduction of the optical threshold energy is expected to have tremendous implications on the technological applications of this system. Doping TiO_2 with transition metals results in thermal instability, an increase of carrier-recombination centers and the requirement of an expensive ion-implantation facility [57]. In 2001 R. Asahi et al. [58] showed that a more successful approach can be obtained by N, S and C doping. A large number of experimental works on nonmetallic doping appeared, mostly regarding nitrogen doping [56, 59, 60]. Most of these works show that nitrogen in the TiO_2 matrix improves absorption in the visible region and leads to increased photocatalytic activity. There are several chemical and physical methods to implant nitrogen in the anatase matrix, among them

we find the sol-gel synthesis, chemical treatment of the bare oxide, oxidation of titanium nitride, ion implantation and magnetron sputtering [59, 61, 62, 63]. However, the role that nitrogen impurities and native defects such as oxygen vacancies, play in enhancement of photocatalytic properties is still under debate. This situation arises because experimental characterization of these impurities is not straightforward. While some groups propose the presence of NO_x [64] or NH_x [65, 66, 67, 68] interstitial species and even interstitial N [58, 59, 67], others attribute enhancement of the photocatalytic activity to substitutional nitrogen. This variety of proposed species is due to the different methods used in the implantation of N [59].

In order to manipulate the gap of this material while maintaining its beneficial photocatalytic activity, one has to understand how impurities modify the TiO_2 properties. The first requirement is characterizing the electronic, structural and vibrational properties of these impurities experimental and theoretically. Although it is well accepted that the optical absorption of anatase shifts to the visible region when it is doped with N, there is no a consensus on the character of the electronic states that leads to this shift [58, 59, 69]. While some authors say that interstitial and substitutional nitrogen cause the formation of localized electronic states just above the valence band border, others say that these electronic states overlap with the valence band, narrowing the gap. K. Yang et al. [70] suggests that the overlap take place only at high doping concentrations. In relation to the interaction of nitrogen impurities with point defects, Selloni et al. [59] found that the presence of nitrogen impurities, specially substitutional nitrogen, considerably decreases the formation energy of oxygen vacancies. They also found that the formation of nitrogen clusters does not take place, even at high nitrogen concentration.

Other aspect to be considered is the charge state of defects since it is well known that charged defects form easily in metallic oxide semiconductors, affecting the electrochemical properties of the material. There are few theoretical works on the thermodynamic of native defects in anatase with different charge states as a function of oxygen chemical potential. At present, it is well accepted that oxygen vacancies and interstitial titanium with charges +2 and +4, respectively, are the most easily formed defects in pristine anatase. However, there are few works on

formation energies of charged nitrogen impurities [60]. Hence, additional studies that contribute to complete the stability diagrams of these species and to the understanding of the relation between the thermodynamic and photocatalytic properties, are required.

One of the experimental techniques that is used for the characterization of the N impurities is X-ray photoemission spectroscopy (XPS). This technique allows to distinguish atoms embedded in different chemical environments by measuring the binding energy of the core level electrons (CLBE). The surrounding of the atom, that is, the structural configuration, charge state and hybridization, is one of the factors that determines the binding energy of the core level. In N-doped anatase, the assignment of the peaks observed in the N 1s XPS spectra is still under debate. Two peaks usually appear, at 396 eV and 400 eV, but an additional peak at 402 eV emerges depending of the preparation method. While some authors [58, 59, 61] suggest that the lowest binding energy peak corresponds to substitutional nitrogen and the peak appearing at 400 eV to interstitial nitrogen, other authors suggest the opposite [62]. The extra peak at 402 eV is usually associated to nitrogen species absorbed on the surface, such as N_2 and NH_4. Selloni et al [59] calculated the relative position of the binding energies of interstitial and substitutional nitrogen, and found that the binding energy of interstitial nitrogen is larger than that of substitutional nitrogen, $CLBE[N_{(i)}] > CLBE[N_{(s)}]$, the difference being of ≈ 1.5 eV.

On the other hand, new features are observed for the O 1s XPS spectra in N-doped anatase. In pristine anatase, the O 1s binding energy is measured at 530 eV. Some authors report a shoulder at 532 eV over the tail of O 1s peak when nitrogen is incorporated. This new feature has not been characterized yet. This scenario motivates the theoretical study of the core level binding energies of these species, aiming at a better understanding and characterization of nitrogen impurities in XPS experiments.

Other experimental methods that are frequently used for characterizing pristine anatase as well as N-doped anatase are Raman and IR spectroscopies. IR spectroscopy has been mainly focused for characterization of organic molecules absorbed on anatase surfaces. Recently, Guillaume et al. [**] reported a blue shift to higher frequencies, and spreading of the lowest-wave-number Raman mode E_{1g}

(145 cm^{-1}) in N-doped polycrystalline anatase grown by pulsed laser deposition (PLD) as a function of doping concentration. The experimental Raman spectra of anatase with different concentrations of N impurities, 0-2.9 at.% (atomic percent) are shown in Fig. 5.1. The concentration was measured by electron photoemission spectroscopy (EPS). The maximum of the intensity of this Raman peak moves to higher frequencies as N-doping concentration increases. The implantation of nitrogen also spreads and decreases the intensity of the peak. The largest shift observed is of 7 cm^{-1} and corresponds to 2.9 at.% of implanted nitrogen. Such blue shift could be due to the implanted nitrogen impurities, but also to native defects formed during doping, as a similar shift was reported in non-stoichiometric anatase [71, 72]. To our knowledge, there is no theoretical reports on the lattice dynamic of anatase with point defects and charge states. In this work, we study the electronic and structural properties and thermodynamic stability of the most stable native defects (oxygen vacancies and interstitial titanium) and nitrogen impurities (substitutional and interstitial nitrogen) with several charge states in anatase TiO_2. We perform phonon calculations to know how the point defects affect the vibration modes of pristine anatase and what new features associated to these defects appear. We also calculate the core level binding energy shifts (CLBES) of 1s N, 1s O and 2p Ti core levels, as a way to characterize the impurities as a function of its chemical environment.

We start presenting results of pristine anatase as it is our reference system, and then we move to discuss results of point defects: first, oxygen vacancies and interstitial titanium (the most relevant native defects), and then substitutional and interstitial nitrogen impurities. We follow the next order: electronic properties, geometrical aspects, thermodynamic stability, vibrational properties and binding energy shifts.

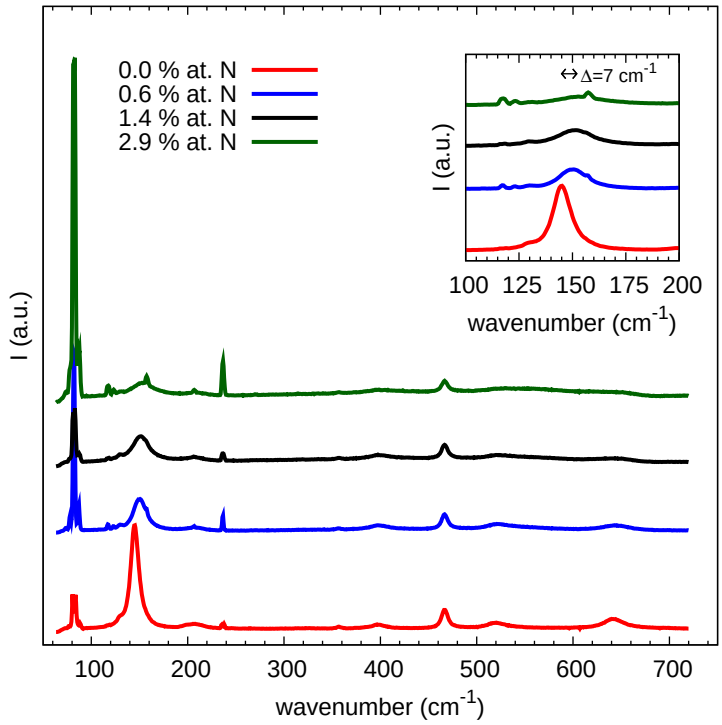

Figure 5.1: Experimental Raman spectrum of N-doped anatase obtained by Guillaume et al. The nitrogen content in the samples was measured by XPS spectroscopy. A shift of the $E_g(1)$ phonon mode towards higher frequencies is observed when nitrogen is incorporated in the sample. The maximum shift is of 7 cm^{-1} and corresponds to a nitrogen content of 2.9 % at. N.

5.2 Methodology

5.2.1 Defect energetics

The formation energy E_{form} of a defect in a charge state q is evaluated according to the general formula:

$$E_{form} = E_{tot}[D^q] - E_{tot}[0] + \sum \Delta n_X \mu_X + q\mu_e \tag{5.1}$$

where $E_{tot}[D^q]$ is the total energy of supercell with the defect D in the charge state q; $E_{tot}[0]$ is the total energy of the defect-free supercell; Δn is the number of

atoms of the chemical specie X (=Ti,O,N) being either removed (Δn is positive) or incorporated (Δn is negative) into the supercell from/to its respective reservoir with chemical potential μ_X; μ_e is the electronic chemical potential. The stability condition of TiO_2 is

$$\mu_{Ti} + 2\mu_O = \Delta E_{form}(TiO_2) \tag{5.2}$$

where $\Delta E_{form}(TiO_2)$ is the formation energy of TiO_2 from its constituent. If we set $\mu_X = 0$ for the respective natural phases of Ti and O, the limits of the values of the chemical potential for O and Ti that cause the precipitation of the phase anatase are

$$\mu_{Ti} \leq 0 \tag{5.3}$$

$$\mu_O \leq 0 \tag{5.4}$$

Notice that from Eq. 5.2 the chemical potential of Ti and O are related, so that we can write the chemical potential of Ti as a function of the chemical potential of the oxygen, obtaining thus the values of chemical potential for which the precipitation of the anatase phase is favoured. In this work we study the formation energy of anatase with point defects as a function of the chemical potential of the oxygen. We also study the formation energy of charged point defects as a function of the electronic chemical potential taking the valence band edge of defect-free system as reference,

$$\mu_e = E_f + \mu_{e'} \tag{5.5}$$

5.2.2 Computational details

All calculations are performed within the density functional theory (DFT) formalism as implemented in the SIESTA code. The main features of this code have been discussed previously in the chapter 2. We use the generalized gradient approximation (GGA) with the Perdew-Burke-Ernzerhof (PBE) parametrization for the exchange-correlation functional. The Troullier-Martins pseudopotentials with core correction are calculated with the ATOM program and DZP-type basis set are optimized with the SIMPLEX algorithm under a fictitious basis pressure of 0.1 GPa [30]. The real-grid mesh cut-off is set at 450 Ry and the k-point sampling for Brillouin zone integration is defined through a $5 \times 5 \times 2$ Monkhorst-Pack

block [73] for the anatase unit cell. All structures were relaxed using the conjugated gradient algorithm (CG) until the maximum force on any atom is smaller than 0.01 eV/$\AA$. Spin polarization is used to study possible magnetic effects.
Our calculated cell parameters of bulk anatase TiO_2 are $a = 3.83$ $\AA$ and $c = 9.72$ $\AA$, which are in good agreement with those reported by other theoretical groups [59, 74, 75]. Using these relaxed lattice parameters and atomic coordinates, we build a $2\sqrt{2} \times 2\sqrt{2} \times 1$ supercell containing 96 atoms to study the point defects. The Monkhorst-Pack block used for these defective supercells is $4 \times 4 \times 4$.
Nitrogen impurities are placed either in substitutional positions (N_{subs}) by replacing oxygen atoms or in interstitial positions (N_{int}). In the case of native point defects, oxygen atoms are removed from the supercell to create oxygen vacancies (V_O) and titanium atoms were placed in interstitial positions (Ti_{int}). For the oxygen vacancies, ghost orbitals are used to give a better representation of the electronic states of the vacancy. The point defects are studied with different charge states. For the native defects we considered only positive charge states, namely $(0, 1+, 2+)$ and $(0, 1+, 2+, 3+, 4+)$ for V_O and Ti_{int}, respectively. For nitrogen impurities we considerer positive as well negative charge estates, namely $(-3, ..., 0, ..., 3+)$ and $(-2, ..., 0, ..., 3+)$ for N_s and N_{int}, respectively.
Since we do not observe large changes in the lattice parameters of the relaxed defective supercells from those of the pristine supercell, for the phonon calculations we build again the defective supercells using the lattice parameters of the relaxed pristine anatase unit cell, relaxing only their atomic coordinates (fixed cell parameters). Then, we calculate the phonon modes for the resulting supercells. This allows us to compare phonon modes from different systems.
To calculate the phonon modes, a fine mesh cutoff of 450 Ry is used to ensure that so-called egg-box effects are negligible. We compute the force constant matrix and Born charge tensors using numerical derivatives with atomic displacements of 0.02 Bohr. To obtain the phonon frequencies we use the VIBRA program. It computes the phonon frequencies through solving the secular equation (2.28) for Γ-point. For the LO-TO splitting we use the experimental dielectric constant tensor of the anatase phase whose diagonal elements are 5.82, 5.82 and 5.41. The non-diagonal elements are zero for the tetragonal Bravais lattice used in this work. The sum upon the reciprocal lattice vector of Eq. (2.29) is done up to a

maximum radius of 20 Bohr.

To investigate the effects of the point defects on the lattice dynamic of pristine anatase, we study how these point defects affect E_{1g} Raman active phonon mode and what new features appear in the IR spectrum. Experimentally, the $E_g(1)$ peak was observed to shift to higher frequencies under nitrogen doping. To understand the behaviour of the $E_g(1)$ phonon mode when there is a point defect in the anatase matrix, we follow the next methodology. First, we characterize unambiguously the E_{1g} phonon mode in pristine anatase unit cell by applying the appropriate symmetry operations (indicated in the crystallographic table of anatase, which is the No. 141, $I4_1/amd$), over the whole set of phonon modes, and comparing the obtained elements with the character table associated to the anatase symmetry (shown in the Table (5.1)).

Table 5.1: Character table of the point group D_{4h}

D_{4h}	E	$2C_4$	C_2	$2C_2'$	$2C_2''$	i	$2S_4$	σ_h	$2\sigma_v$	$2\sigma_d$
A_{1g}	1	1	1	1	1	1	1	1	1	1
A_{2g}	1	1	1	-1	-1	1	1	1	-1	-1
B_{1g}	1	-1	1	1	-1	1	-1	1	1	-1
B_{2g}	1	-1	1	-1	1	1	-1	1	-1	1
E_g	2	0	-2	0	0	2	0	-2	0	0
A_{1u}	1	1	1	1	1	-1	-1	-1	-1	-1
A_{2u}	1	1	1	-1	-1	-1	-1	-1	1	1
B_{1u}	1	-1	1	1	-1	-1	1	-1	-1	1
B_{2u}	1	-1	1	-1	1	-1	1	-1	1	-1
E_u	2	0	-2	0	0	-2	0	2	0	0

Then, we identify the phonon mode equivalent to E_{1g} in the supercell, which is used to track phonon modes resembling E_{1g} symmetry among the defective anatase supercell vibrational modes. The evolution of the phonon mode $E_g(1)$ is followed by projecting the eigenvectors $\overrightarrow{U}_{per}$ of the defective system on the

pristine E_{1g} eigenvector $\overrightarrow{U}_{ref}$, according to the simple equation

$$pw = \frac{\overrightarrow{U}_{ref} \cdot \overrightarrow{U}_{per}}{|\overrightarrow{U}_{ref}|} \tag{5.6}$$

where pw is the projection weight. As the original phonon modes are normalized, large values for the pw indicate that the projected phonon is symmetrically similar to E_{1g} pristine phonon mode. For this study, the defective supercells have only one point defect, because a high concentration of defects introduces strong structural distortions and, as a consequence, we can not describe properly the evolution of $E_g(1)$ phonon mode.

To investigate new features arising from the point defects that could be IR active, we identify the phonon modes strongly localized around the impurities. Then, we calculate the IR intensity of those vibrational modes showing a symmetry that could lead to the formation of an electric dipole. The intensity of the peaks is scaled to the value of the TiO_2 IR peak $E_u(2)$.

We compute the core level binding energy shifts for N 1s, O 1s, and Ti 2p core levels within the initial and final approximation discussed in chapter 2. In the final state, we impose a net charge of +1.0 upon the anatase supercell containing any defect, to remove the extra electron that is added to build the Kohn-Sham Hamiltonian correctly (see chapter 2 for details). The electron must be removed because the TiO_2 anatase phase is a semiconductor material, and therefore there is not free electrons in the system to screen the hole core created by the photoemission process. We take the Ti 2p and O 1s core level binding energy of Ti and O atoms, far enough from the point defect as references. For the nitrogen impurities, we determine the relative shift of the N 1s core level binding energies of the different nitrogen species: substitutional (N_s), interstitial (N_i) and molecular nitrogen (N_2). Since the cell used to study the isolated nitrogen molecule is different to the cells used for the substitutional and interstitial nitrogen, we take the total potential of the isolated nitrogen molecule at the vacuum as reference. We compute the total potential at the vacuum for the pristine anatase using a slab of this material perpendicular to the (101) direction of its tetragonal unit cell (because the (101) surface is the most thermodynamically stable for anatase).

We then align this potential with the reference potential. At the same time, we align the value of total potential at the bulk of the slab, with the value of the total potential of the cell with the defect, calculated at a point far from the impurity.

5.3 Results and discussion

This section is devoted to show and discuss our theoretical results. In the first subsection, we show and discuss the electronic, structural and vibrational properties of pristine anatase. Then, we proceed to discuss the properties for the point defects considered, comparing them with experimental data obtained from XPS and Raman spectroscopies and with other theoretical works.

5.3.1 Features of pristine Anatase

Anatase TiO_2 crystallizes in the tetragonal Bravais lattice with spatial symmetry $I4_1/amd$ (see Fig. 5.2), D_{4h}^{19}. The optimized cell parameters are $a = 3.83$ $\mathring{A}$ and $b = 9.72$ $\mathring{A}$, which are in good agreement with those calculated by other groups using the same exchange-correlation functional [59]. In anatase structure, each oxygen atom is connected to three titanium atoms through two equivalent equatorial bonds and one axial bond, whose lengths are 1.73 and 1.90 $\mathring{A}$, respectively. On the other hand, each titanium atom is bonded to 6 oxygen atoms; with four equatorial bonds and two axial bonds. The octahedron around the titanium atoms are significantly distorted. Our theoretical result for the direct band gap of this material is 2.1 eV to be compared to the experimental value of 3.2 eV. It is well known that the band gap is underestimated within the density functional theory formalism. Our result is comparable to those obtained by other groups [59]. Figure 5.3.1 represents the anatase band structure using the tetragonal Brillouin zone [76], sketched at the top of the same figure. From now on, all band structures will be shown setting the Fermi level at the top of the valence band. The character of the valence bands are mainly O 2p, while the conduction bands have a Ti 2p character.

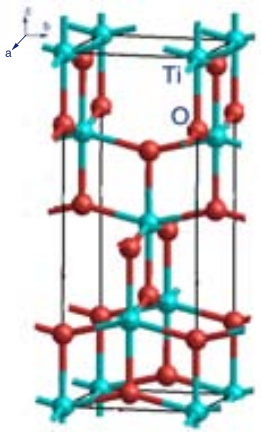

Figure 5.2: Anatase unit cell.

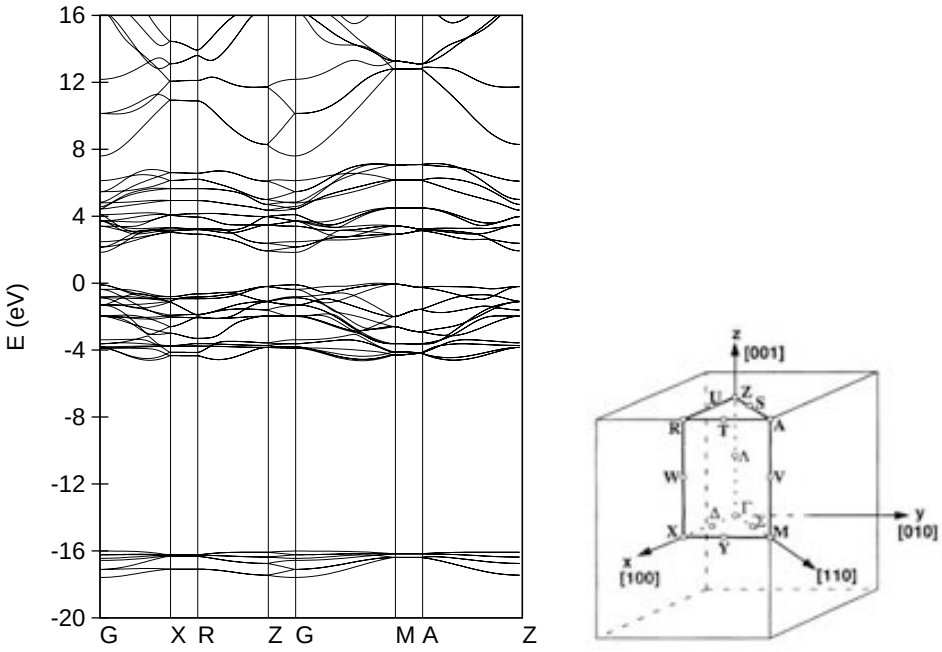

Figure 5.3: Band structure of anatase calculated with SIESTA using the GGA approximation (left side) and the tetragonal Brillouin zone (right side).

We calculate the diagonal Born effective charge tensors. These elements are summarized in Table 5.2 and they are in good agreement with the values reported

in Refs. [74, 75]. The effective charges of Ti are larger than the nominal ionic charge of Ti ($Z = +4$). These anomalous effective charges that are also observed in TiO_2 rutile and perovskite Ti compounds, can be explained in view of mixed ionic-covalent bonding [74]. On the other hand, the effective charges of oxygen exhibit a strong anisotropy. The component along the a lattice vector is much smaller than the nominal ionic charge ($Z = -2$). A similar trend is observed in TiO_2 rutile [77, 78], and perovskite Ti compounds [79].

Since there are six atoms in the anatase unit cell, there are fifteen optical and

Table 5.2: Born effective charge tensors of anatase phase. The directions $i = 1, 2, 3$ are along a, b, and c axis in the conventional unit cell, respectively. The born effective charge tensors are diagonalized.

	Anatase			
	This work		Ref. [74]	
i	$Z_i^*(Ti)$	$Z_i^*(O)$	$Z_i^*(Ti)$	$Z_i^*(O)$
1	+6.630	-1.218	+6.678	-1.161
2	+6.630	-5.414	+6.678	-5.517
3	+5.863	-2.923	+5.713	-2.856

three acoustic modes. The irreducible representation of the optical modes at Γ point is

$$\Gamma_{opt} = A_{1g} + A_{2u} + 2B_{1g} + B_{2u} + 3E_g + 2E_u \tag{5.7}$$

The modes A_{2u} and E_u are IR active, whereas the modes A_{1g}, B_{1g} and E_g are Raman active. The mode B_{2u} is a silent mode. The E modes are doublets (doubly degenerate) and perpendicular to the c axis of the conventional unit cell, along either $\langle 110 \rangle$ or $\langle 1\bar{1}0 \rangle$ direction, while the other modes are singlet and parallel to the c axis. Table 5.3 summarizes our results of phonon frequencies and compares them with theoretical results and experimental data reported in the literature, including LO-TO splits of the IR active vibrational modes. For a quantitative comparison of our results with the experimental data, we calculate the root-square-mean deviation (RSMD), obtaining a value of 25.78 cm^{-1} and a normalized RSMD of 3.52 %. Our results are comparable with the theoretical values reported in Ref. [74], and included in the Table (5.3). In this work, we focus on the lowest-frequency $E_g(1)$ Raman active mode that was experimentally observed to shift

towards higher frequencies and to spread and decrease in intensity when nitrogen impurities are implanted in the anatase matrix. The calculated frequency of this phonon mode $E_g(1)$ is larger in comparison to the experimental value reported in Ref. [80] and even with other theoretical values [74].

Table 5.3: The wave numbers of phonon eigenmodes for anatase at Γ (cm^{-1})

		Theory			Experiment	
Mode		This work	Ref. [74]	Ref. [81]	Ref. [80]	Ref. [81]
Raman						
$\mathbf{E_g}(1)$		**162.8**	**145.6**	**152**	**144**	
$E_g(2)$		189.1	171.1	307	197	
$B_{1g}(1)$		401.3	398.4	400	399	
$B_{1g}(2)$		552.6	518.4	515	519	
A_{1g}		531.7	535.9	519	513	
$E_g(3)$		664.7	662.1	640	639	
Infrared						
$E_u(1)$	TO	259.8	248.6	329		262
	LO	325.2	340.6	428		366
$A_{2u}(1)$	TO	383.7	375.3	566		367
	LO	775.6	743.1	844		755
$E_u(2)$	TO	492.7	479.9	644		435
	LO	881.4	892.2	855		876
Silent						
B_{2u}		542.7	564.6	435		

5.3.2 Point defects

Figure 5.4 shows the geometrical configuration of the most easily formed point defects and Table 5.4 summarizes the values of the structural parameters. The concentration of defects in the cell is of ∼ 1.03 at. %. This concentration is within the range of values measured experimentally by Guillaume et al. and at the same time it is sufficiently small for the electrostatic interaction between the charged defect and its periodic images to be negligible. In all cases, we observe that cell

parameters are unchanged due to the presence of the defect. Moreover, we obtain the same result when we incorporate more than one defect per supercell, up to $\sim$ 3.0 and $\sim$ 2.1 at. %. of nitrogen (interstitial and substitutional) and oxygen vacancies, respectively. We observe that structural changes are localized around the defects.

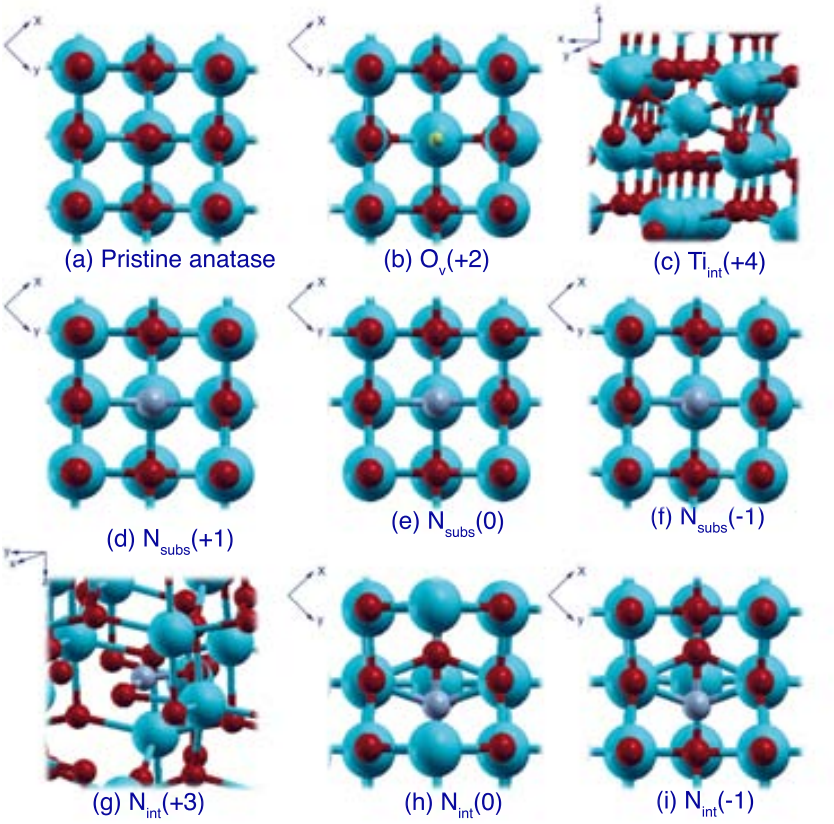

Figure 5.4: structural configuration of the point defects.

Table 5.4: Structural parameters of the point defects: bond lengths and angles.

Interstitial-Ti				
charge	Ti_{int}-O_{ap}	Ti_{int}-O_{eq}	$\angle$(O_{ap}-Ti_{int}-O_{eq})	$\angle$(O_{ap}-Ti_{int}-O_{eq})
0	1.98	2.07	92.9	87.1
+1	1.98	2.06	92.9	87.1
+2	1.97	2.05	92.6	87.4
+3	1.95	2.05	92.6	87.4
+4	1.90	2.01	92.0	88.0
Oxygen vacancy				
charge				
+2	2.23	2.21	153.73	103.13
+1	2.23	2.22	153.58	103.21
0	2.22	2.23	153.53	103.23
Substitutional-nitrogen				
charge	N-Ti_{ax}	N-Ti_{eq}	$\angle$(Ti_{eq}-N-Ti_{eq})	$\angle$(Ti_{ax}-N-Ti_{eq})
-3	1.93	1.90	158.4	100.8
-2	1.93	1.90	157.7	101.1
-1	1.93	1.90	157.1	101.4
0	2.07	1.98	159.2	100.4
+1	2.51	2.05	169.7	95.2
+2	2.53	2.07	170.2	94.9
+3	2.55	2.14	171.7	94.1
Interstitial-nitrogen				
charge	N-O	N-Ti(1)	N-Ti(2)	
-2	1.47	2.07	2.04	
-1	1.46	2.07	2.04	
0	1.37	2.38	2.09	
+1	1.32	2.23	2.49	
+2	1.42	2.85	2.63	
+3	1.30	3.05	2.92	

Oxygen vacancy

When an oxygen vacancy is created, the neighbouring titanium atoms of the vacancy move slightly away from it. The largest displacement occurs for the vacancy having a charge state +2. All these structural distortions are localized around the vacancy.

We find that the formation energy of the neutral state (4.8 eV) under oxygen-rich conditions is comparable to the value reported for the same state by Selloni et al. [59] using plane waves and a hybrid functional (4.2 eV). We observe that new electronic states associated to the vacancy appear in the conduction band for all charge states. However, electron paramagnetic resonance (EPR) experiments shows new electronic states associated to oxygen vacancies slightly below the conduction band edge (0.8 eV from the conduction band edge), and assigned to Ti^{+3} 3d states [56, 67]. Several author suggest that a good description of these electronic states requires the use of hybrid functionals or DFT+U [59, 82]. Analysing the formation energy diagram of the oxygen vacancies for several charge states obtained using standard DFT (showed in Fig. 5.5), we observe that the charge state with the lowest formation energy in the allowed electronic chemical potential range is +2. In this charge state, the electronic levels associated to the oxygen vacancy appearing in the conduction band are empty, which means that this charge state could be correctly described using DFT with standard functionals (LDA and GGA). The oxygen vacancy in this charge state is more easily formed at low electronic chemical potentials. This result is in good agreement with previous theoretical reports [59, 83]. Figure 5.6 shows the projection weights of the phonon modes of the anatase supercell containing an oxygen vacancy defect onto one of the degenerate phonon modes $E_g(1)$ of the pristine anatase against the frequency of the phonon modes. It also shows the fit to a Lorentzian function (red curve), yielding a media value of 135.4 cm^{-1} (a shift of -4.4 cm^{-1}) and a width of 7.5 cm^{-1}. The main contribution to the peak comes from the phonon with frequency of 133.5 cm^{-1} and weight of 0.7. The Lorentzian distribution is used since our data points are much better described (the correlation coefficients are closer to 1.0) than with the Gaussian distribution. A similar result is obtained for the projection upon the other degenerate phonon mode. The average

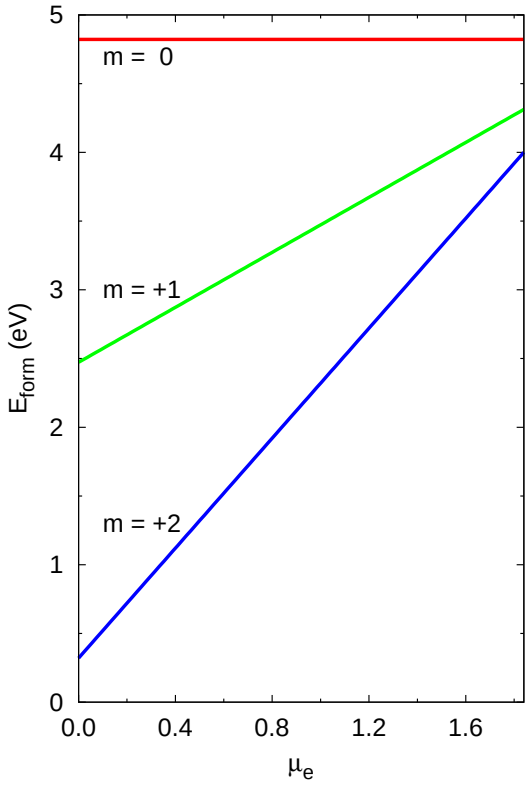

Figure 5.5: Formation energy E_{form} of the oxygen vacancies with charge m ($m = +2, +1, 0$), as a function of the electronic chemical potential μ'_e relative to Fermi energy level, which is set at the valence band edge.

shift value of the degenerate modes is -5.8 cm^{-1}. Thus, the formation of oxygen vacancies in the anatase matrix leads to a shift of the $E_g(1)$ peak towards lower frequencies and that this shift is followed by a small spread of the peak. This result is in contradiction to what several authors have observed in nanostructured nonstoichiometric TiO_2, that the $E_g(1)$ peak moves towards higher frequencies as the concentration of oxygen vacancies increases [71, 72]. Our hypothesis is that other factors apart from the concentration of oxygen vacancies, like the particle size, are responsible for this shift. Using the DFT machinery to simulate clusters containing thousands of atoms is extremely expensive and beyond the scope of this work.

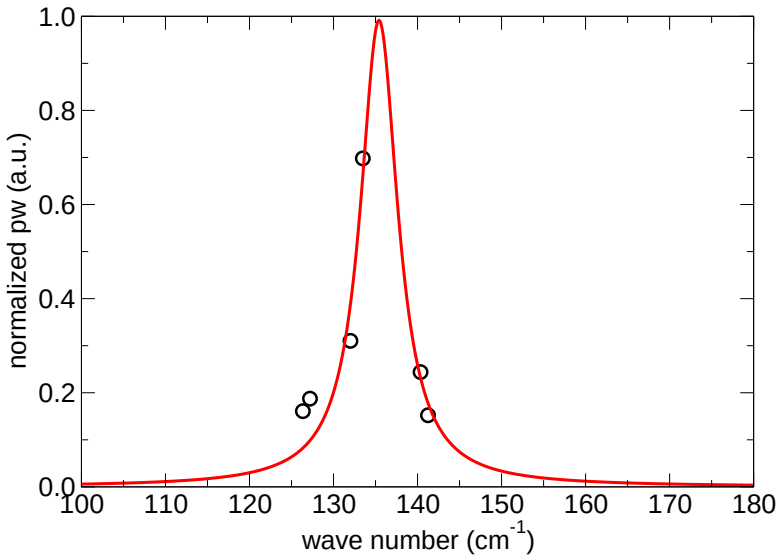

Figure 5.6: Normalized weights (black circles) from the projection of the phonon modes of the anatase supercell containing a oxygen vacancy onto one of the doublet $E_g(1)$ modes of the pristine anatase. The red curve indicates the resulting fit of the normalized weights to a Lorentzian function: media = 135.4 cm^{-1}, weight = 0.99 and width = 7.5 cm^{-1} (corr. coeff. = 0.98).

Interstitial titanium

The interstitial titanium (Ti_{int}) in the neutral charge state has a distorted-octahedron configuration (slightly elongated along one of its axis) than those in the anatase matrix. The four equatorial oxygen atoms are in the plane perpendicular to the apical axis (which is along the (110) direction), forming angles of about 90^o with the interstitial titanium and each of the apical oxygen atoms, and the Ti_{int}-O lengths are larger than in the pristine anatase: the equatorial and axial Ti-O lengths are of 2.06 $\AA$ and 1.97 $\AA$, respectively. These lengths do not change noticeably for the positive charge states studied (the largest variation is of 0.08 $\AA$).

New electronic states associated to the interstitial titanium appear slightly above

the conduction band edge as well as just below it, not showing a large dispersion. The occupation of these electronic levels depends on the net charge on the system. Analysing the formation energy diagram for these systems, depicted in Fig. 5.7, we observe that the interstitial titanium with a net charge of +4 has the lowest formation energy in the whole range of allowed electronic chemical potential. In this charge state all electronic levels above the middle of the band gap are empty, which means that, as in the case of the oxygen vacancy, the properties of the system are correctly described with GGA. The electronic states below the conduction band edge are mainly of Ti 3d character of Ti_{int}.

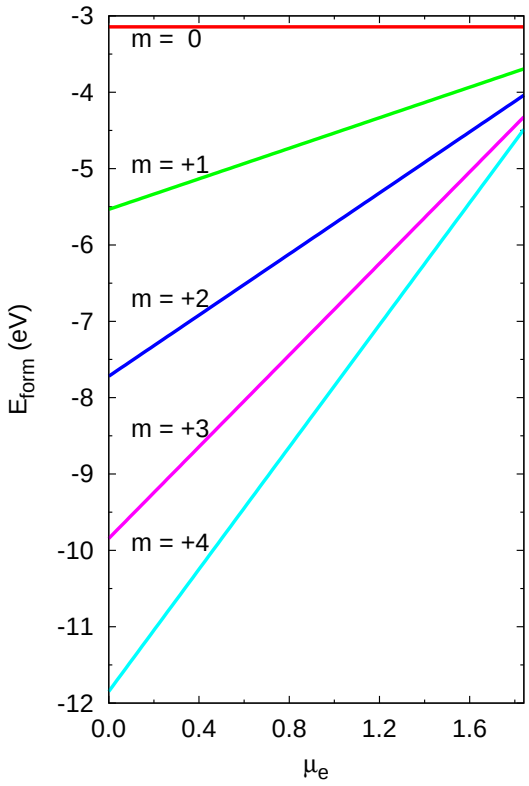

Figure 5.7: Formation energy of interstitial titanium with charge m ($m = 0, +1, +2, +3, +4$), against the electronic chemical potential relative to the Fermi energy level, which is set at the valence band edge.

Next, we calculate the phonon modes of the anatase supercell containing an interstitial titanium atom with a net charge of +4, and project them onto the $E_g(1)$ phonon mode of the pristine anatase. After an intensive review of the literature concerning to anatase TiO_2 with titanium native defects, we did not find any previous theoretical or experimental report studying the lattice dynamics. Fig. 5.8 shows the projection weights onto one of the degenerate $E_g(1)$ phonon modes of pristine anatase against the frequency (a similar behaviour is obtained for the projection onto the other degenerate $E_g(1)$ phonon mode). Fitting the projection weight values from each of the degenerate $E_g(1)$ phonon modes to a Lorentzian function, we obtain an average value for the media of 157.5 cm^{-1}. Unlike the case of oxygen vacancies, the inclusion of titanium atoms in interstitial positions leads to a shift of $E_g(1)$ peak towards higher frequencies, with an average shift of +17.8 cm^{-1}. As in the case of oxygen vacancies, the interstitial titanium does not give a significantly large spread of the peak (average width of 22 cm^{-1}). The shift obtained for the interstitial titanium is larger than the value measured experimentally in N-doped anatase by Guillaume et al. (of about +5 cm^{-1}). This result suggests the experimental conditions used by Guillaume et al. do not result in a significant concentration of interstitial titanium.

In order to investigate what new features arise from the interstitial titanium, we determine the weight of this impurity for each phonon vector and plot it against the phonon frequency as shown in the Fig. 5.9. We observe two low-frequency phonon modes (with frequencies of 74.0 and 83.8 cm^{-1}) that are localised around the defect. However, their calculated IR intensities (0.001 and 0.002, respectively) are too small relative to the largest theoretical IR intensity of pristine anatase (intensity of 1.0), which corresponds to the longitudinal optical $E_u(2)$ phonon mode (881.4 cm^{-1}).

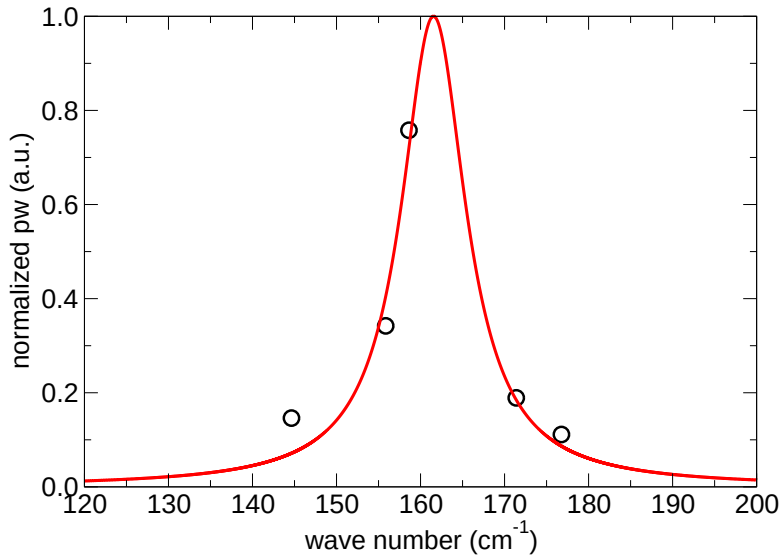

Figure 5.8: Normalized weight projections obtained from projecting the phonon modes of the anatase supercell containing an interstitial titanium with a net charge +4, onto the $E_g(1)$ phonon modes of the pristine anatase. Statistical results: media = 161.5, weight = 0.99 and width = 21.9 cm^{-1} (corr. coef. = 0.98).

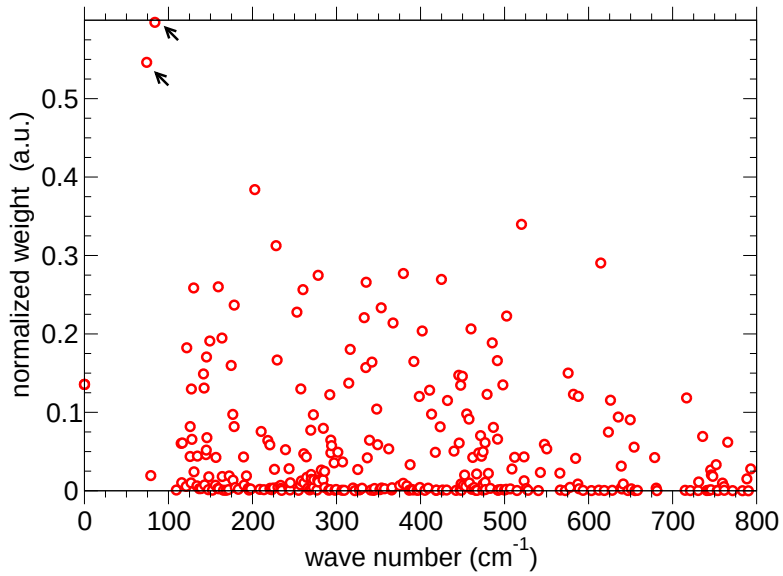

Figure 5.9: Normalized weight of the interstitial titanium for each phonon mode vector against frequency.

Nitrogen impurities

In the case of nitrogen impurities we studied both interstitial and substitutional nitrogen, with negative and positive charge states. In the former case, an oxygen atom of the anatase supercell is replaced by a nitrogen atom leading to nitrogen impurities having the same connectivity and configuration as the oxygen removed. In the neutral charge state, the Ti-N bonds are slightly longer than the Ti-O ones. When a net charge is imposed on the supercell, we observe that for negative charge states, the Ti-N bonds become shorter than those of the neutral state, while for positive charge states, the Ti-N bonds are longer. On the other hand, neutral interstitial nitrogen forms a strong bond with an oxygen atom of the anatase matrix, having a N-O length of 1.37 $\AA$, in agreement with the value reported in Ref. [59]. The lowest energy configuration of the N-O specie is shown in Fig. 5.4. N-O interacts with the equatorial titanium atoms through π bonds and with the axial titanium through a σ_p bond. In negatively charged configurations, this σ_p bond is shorter than in the neutral state. This increases the π bonds by 0.09 $\AA$. Larger changes occurs for the interstitial-N configuration when positive charges are imposed, specially in the charge state +3. Here, the nitrogen impurity is bonded to two oxygen atoms in a configuration shown in Fig 5.4, with N-O lengths of 1.30 $\AA$.

When anatase is doped with nitrogen impurities (both interstitial and substitutional), partially-occupied localized electronic states are induced slightly above the valence band edge. For the lowest doping concentration studied (of about 1.03 at. %), the lowest edge of these states appear 0.14 and 0.73 eV above the top valence band edge for substitutional and interstitial nitrogen, respectively. The character of these electronic states is N 2p for substitutional and, N and O 2p for interstitial. As concentration of doping increases, these localized states become closer to the valence band edge, overlapping with it in the case of substitutional nitrogen. This overlap has also been observed by K. Yang et al. [70], who characterized the electronic properties of anatase in terms of the substitutional-N doping concentration. Thus, the band gap narrowing observed experimentally for N-doped anatase could be attributed to the localized electronic levels of nitrogen just above the valence band and overlapping with it.

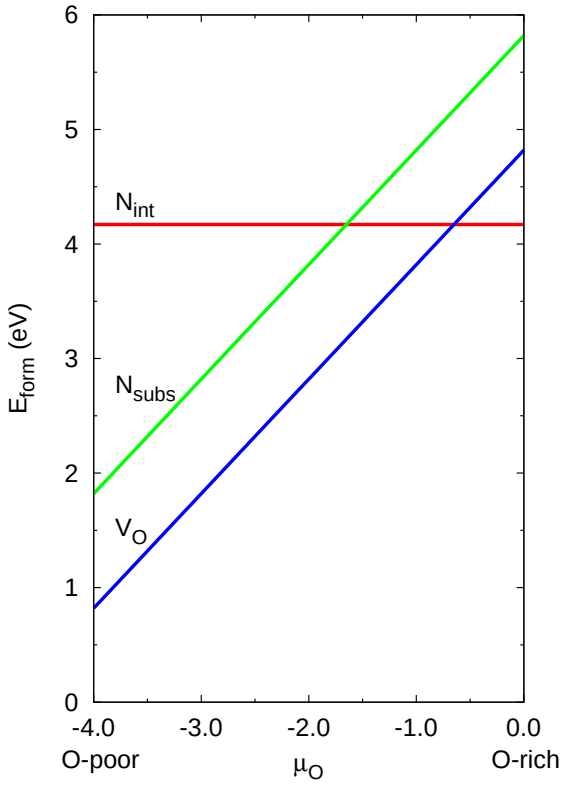

Figure 5.10: Formation energy curves of neutral nitrogen impurities and oxygen vacancies against of the oxygen chemical potential that corresponds to a oxygen-rich environment.

Figure 5.10 shows formation energies of the nitrogen impurities and oxygen vacancy in the neutral state, as a function of oxygen chemical potential. For oxygen-rich conditions (a high oxygen partial pressure), the calculated formation energies of the impurities are 5.8 and 4.2 eV for substitutional and interstitial nitrogen, respectively, indicating that for these conditions interstitial nitrogen is most easily formed. These values are comparable to those obtained by Selloni et al. [59], 5.8 and 4.3 eV, respectively. The formation energy of substitutional nitrogen decreases when the oxygen chemical potential becomes smaller. For oxygen chemical potentials lower than -1.65 eV, the formation energy is always smaller for the substitutional nitrogen than for the interstitial one. On the other hand, the formation of the oxygen vacancies is favoured for oxygen-poor condi-

tions (low oxygen pressures).

The formation energy diagrams for charged substitutional and interstitial nitrogen impurities are shown in the Figs. 5.11 and 5.12). These figures were calculated with $\mu_O = 1/2E_{O_2}$ and $\mu_N = 1/2E_{N_2}$ (oxygen- and nitrogen-rich conditions). We observe that positive as well as negative charge states are possible. Each of these charge states dominate within a certain range of the electronic chemical potential. These ranges are delimited by electron capture processes in which the defect traps one or more electrons from the environment as the electronic chemical potential increases.

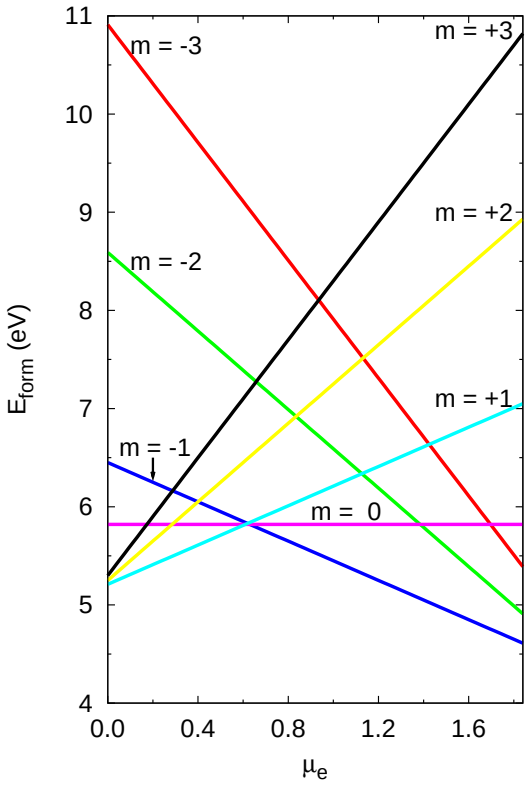

Figure 5.11: Formation energy diagram of substitutional nitrogen with a net charge m ($m = -3, ..., 0, ..., +3$), as a function of the electronic chemical potential measured from the Fermi energy level set at the valence band edge.

The charge states +1, 0 and -1 are the most easily formed for substitutional nitrogen, having always positive formation energies for the chemical potential of nitrogen and oxygen considered. At 0.6 eV from the valence band edge the substitutional nitrogen with charge +1 traps one electron from the environment, reaching the neutral state. At 0.62 eV the neutral substitutional nitrogen traps another electron, becoming negatively charged (-1). These transitions are not followed by a drastic structural rearrangement, only small changes are found in the bond lengths as indicated in Table 5.4. Note that the stability region of the neutral state is quite narrow (of about 0.02 eV), but it enables a continuous transition between the different charge states allowed.

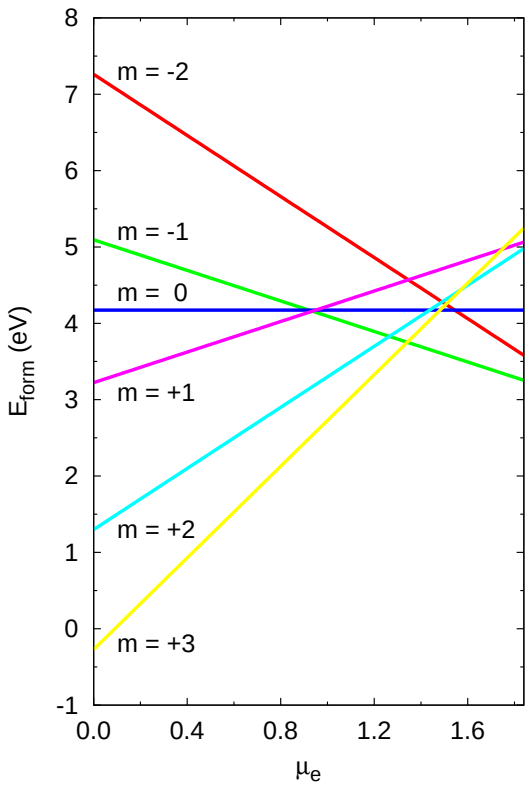

Figure 5.12: Formation energy diagram of interstitial nitrogen with a net charge m ($m = -2, ..., 0, ..., +3$), as a function of the electronic chemical potential measured from the Fermi energy level set at the valence band edge.

For interstitial nitrogen the formation energy diagram shows that the most easily formed charge states are +3 and -1. In the transition point between these charge states, at 1.4 eV from the valence band edge, the system with charge +3 traps four electrons, leading to a drastic change of the configuration around the defect. While in the state -1 the configuration of nitrogen is similar to that of the neutral state where the nitrogen is linked to an oxygen atom of the anatase matrix, in the state +3 the nitrogen is significantly closer to two oxygen atoms, adopting the configuration shown in Fig. 5.4. This charge state is most stable for a broader range of electronic chemical potential.

Comparing the stability diagrams of substitutional and interstitial nitrogen, we notice that for the chemical potential of the oxygen and nitrogen used (an oxygen- and nitrogen-rich environment) the interstitial nitrogen is more easily formed than substitutional. However, for low μ_O (that corresponds to oxygen-poor environment), the charged substitutional nitrogen (-1) becomes the most stable at high and low electronic chemical potential, respectively. The formation of substitutional nitrogen charged negatively would be favoured by the presence of oxygen vacancies or interstitial titanium, because these defects are electron donors, shifting μ_e to higher values close to the conduction band. Since each oxygen vacancy donates two electrons, two interstitial nitrogens would be needed to compensate each oxygen vacancy. For the interstitial titanium case, four nitrogen impurities would be required.

Table 5.5 shows the results of the statistical analysis of the projection of the phonon modes of the N-doped anatase (with the nitrogen impurities in either interstitial or substitutional position), on the doubly degenerate phonon modes $E_g(1)$ of the pristine anatase. For both interstitial and substitutional nitrogen, we consider the charge states with the lowest possible formation energies: -1, 0 and +1 for substitutional nitrogen, and -1 and +3 for interstitial nitrogen.

Let us start by discussing the results for substitutional nitrogen. In the neutral charge state, although one of the phonon modes shows a relatively large width their frequencies are unchanged with respect to the frequency of the $E_g(1)$ phonon in pristine anatase (139.8 cm^{-1}). However, we observe that in both charge states -1 and +1 one of the degenerate $E_g(1)$ phonon modes shifts to higher frequencies (+3.4 and +4.4 cm^{-1}, respectively). For both +1 and -1 charge states the width

Table 5.5: Results of the Lorentzian fitting of the phonon projection for N-doped anatase TiO_2. Phonon modes of the N-doped anatase are projected onto the degenerate $E_g(1)$ phonon mode of pristine anatase, whose frequency is 139.7 cm^{-1}. We consider the charge states of the impurity with the lowest formation energies within the allowed electronic chemical potential.

Charge state	media (cm^{-1})	projection weight ($a.u.$)	width (cm^{-1})	shift (cm^{-1})
Substitutional-N				
-1	143.2	0.68	30.2	+3.4
	138.5	0.92	2.0	-1.3
0	138.9	0.48	25.3	-0.9
	140.8	0.76	2.9	+1.0
+1	144.2	0.92	67.6	+4.4
	139.5	0.76	14.6	-0.3
Interstitial-N				
-1	110.2	0.64	10.6	-29.6
	112.6	0.86	3.2	-27.2
0	108.5	0.63	50.8	-31.3
	114.5	0.68	47.1	-25.3
+3	110.8	0.99	28.7	-29.0
	111.3	0.54	3.4	-28.5

of the shifted phonon modes is larger than that of the phonon modes that remain practically unshifted.

For the interstitial nitrogen, in both charge states with the lowest formation energy (-1 and +3) we observe a shift towards lower frequencies of the two components of the degenerate $E_g(1)$ phonon mode relative to their frequency in pristine anatase, with one of its components showing a large spread. The average shift is of about -28 cm^{-1}. The phonon mode amplitudes for these charge states are very similar. We additionally consider the neutral interstitial nitrogen, though its formation energy is always larger in comparison with charge states +3 and -1. We observe a similar shift towards lower frequencies of about -28 cm^{-1} for the two components of the $E_g(1)$ phonon mode, but showing a larger spread than in the former cases.

Comparing the results of the phonon projections obtained for the interstitial and substitutional nitrogen with the experimental data from Guillaume et al. we arrive at the conclusion that the shift of the $E_g(1)$ Raman peak towards higher frequencies under the nitrogen doping, could be due to the formation of negatively or positively charged substitutional nitrogen. However, considering that in the preparation method they use an oxygen-poor atmosphere to force the implantation of nitrogen impurities, favouring also the formation of oxygen vacancies (electron donors), the formation of the charged substitutional nitrogen (-1) is likely more favoured. The substitutional nitrogen shows a shift toward higher frequencies of the order of the experimentally measured shift, while interstitial nitrogen shows a shift to the opposite direction.

As in the case of interstitial titanium, we look for new features that arise from the nitrogen impurities and are IR active. Table 5.6 summarizes our results. For the charged substitutional and interstitial nitrogen, we observe several features that shows an IR activity. However, their IR intensities are found to be too small relative to the intensity of the highest IR active lattice vibration (TO $E_u(1)$) of the anatase matrix, except for the phonon mode with frequency 878.4 cm^{-1} in the charge state -1, for which the calculated relative intensity is 0.14. Since the frequency of this feature with high IR intensity is close to the TO $E_u(1)$ peak, it could lead to a broadening of this peak.

Several new features emerge for the interstitial nitrogen, but all with too small IR intensities in comparison with the TO $E_u(1)$ lattice vibration of the anatase matrix. We think that the features appearing at a higher or lower frequency far from the IR region of pristine anatase could be experimentally detected as they do not overlap with the peaks coming from the pristine anatase, in particular the stretching mode of the N-O bond with a high frequency of 1165.6 cm^{-1}. The experimental detection of these features could be used as a way to characterize the interstitial nitrogen.

5.3.3 Core level binding energies (CLBE) of point defects

We proceed to discuss our results for the core level binding energies (CLBE) shifts, which are summarized in the Table 5.7. For O 1s and Ti 2p core levels

Table 5.6: IR active phonon modes arisen from the charged and neutral nitrogen impurities, whether interstitial or substitutional, in the anatase matrix. We only consider the charge states with the lowest formation energies within the allowable electronic chemical potential discussed above. Normalized weight refers to the contribution of the nitrogen impurity to the phonon mode.

Charge state	Frequency (cm^{-1})	Normalized weight ($a.u.$)	IR intensity ($a.u.$)	
Interstitial-Ti				
+4	74.0	0.55	0.09	
	83.8	0.60	0.14	
Interstitial-N				
-1	868.9	0.7	0.5	N-O stretching
	710.0	0.4	0.0	
+3	53.2	0.7	0.2	
	1165.6	0.8	0.2	N-O stretching
	1208.1	0.8	0.1	N-O stretching
Substitutional-N				
-1	298.4	0.4	0.4	
	878.4	0.8	11.2	
0	276.4	0.4	0.1	
+1	613.4	0.7	0.0	

we calculate the shifts by computing the CLBE for two atoms of the same specie (oxygen or titanium) in the anatase matrix, one of them localized near the point defect or being the point defect itself (this is the case of having interstitial titanium), and the other one being far away from the point defect to be considered as the reference. We assume the CLBE calculated for the atom far from the point defect is the expected CLBE for the same atom in the pristine anatase. In fact, we perform some calculations using the pristine anatase cell and we obtain the same results for the shifts. To do this, we align the total electrostatic potential of the cells with and without the point defect as the reference potential. In the case of the N 1s core level the shifts of the interstitial and isolated molecular nitrogen are relative to the CLBE of the substitutional nitrogen (which is taken as the

reference).
The CLBE shifts are calculated using the initial and ΔSCF state approximation, except for the case of the isolated molecular nitrogen where to perform the ΔSCF approximation we have to converge the total energy of the ionized system $E(N_2^+)$ with respect to the size of the cell. We observe that both the initial and final approximations give the same shift directions (except for the O 1s CLBE shift of one of the oxygen atoms close to oxygen vacancy), and that, in general, the final approximation gives smaller values than the initial approximation.
For the Ti 2p core level, the CLBE shifts obtained for the oxygen vacancy and the substitutional and interstitial nitrogen are small and, in most cases, similar to each other within each approximation. This makes difficult the differentiation between these point defects. However, for the interstitial titanium we observe a large shift of about -1.85 eV from the initial approximation (-1.10 from the final approximation) that can be used to identify clearly the presence of interstitial titanium.
For the O 1s core level, we observe a small CLBE shift for substitutional nitrogen that goes towards the opposite direction (negative shift) in comparison to the shifts obtained for the other defects. Among the defects with a positive shift, the interstitial nitrogen shows the largest shift (of about 2.99 and 2.70 eV for the initial and final approximation, respectively), which is ∼2.4 eV greater than the shifts obtained for the native defects. This feature of interstitial nitrogen would allow to identify it from substitutional nitrogen and native defects.
Finally, for the N 1s, the relative position of the CLBE for the interstitial and substitutional nitrogen and the isolated molecular nitrogen (the latter is included only in the initial approximation) is $CLBE(N_2) > CLBE(N_{int}) > CLBE(N_{subs})$. The difference between the substitutional and interstitial nitrogen is of 2.51 eV in the final approximation (and 1.96 in the initial approximation). In both approximations this difference is large enough to enable a distinction between these species. However, from the initial approximation we observe that the difference between the interstitial and isolated molecular nitrogen is very small (of about 0.1 eV).
Considering the results obtained from both approximations we can conclude that substitutional nitrogen can be clearly distinguished from interstitial and molecu-

lar nitrogen by determining the N 1s CLBE shift, while the interstitial nitrogen can be fully distinguished from the substitutional and isolated molecular nitrogen by characterizing the O 1s CLBE shift. Finally, the interstitial titanium is clearly characterized by determined the Ti 2p CLBE shift.

We compare our results with XPS experimental data for N-doped anatase re-

Table 5.7: CLBE shifts for the oxygen vacancies, interstitial titanium (Ti_{int}), and substitutional (N_{subs}) and interstitial (N_{int}) nitrogen. The shifts were calculated within the initial and ΔSCF state approximation. For the Ti 2p core level we compute the shifts for the axial and equatorial titanium atoms, namely Ti_{ax} and Ti_{eq}, respectively. In the cases where we compute the shifts for the first and second neighbours of the defect, they are indicated after the chemical symbol of the atom by the labels (1) and (2).

System	Reference	Core level	Sample atom	Shift (eV) Initial Approx.	Shift (eV) ΔSCF Approx.
N_{subs}-TiO_2	pure-TiO_2	Ti 2p	Ti_{eq}-N_{subs}	-0.32	-0.35
			Ti_{ax}-N_{subs}	-0.07	-0.19
	pure-TiO_2	O 1s	O-Ti-N_{subs}	-0.17	-0.09
	N_{subs}	N 1s	N_2	2.06	
N_{int}-TiO_2	pure-TiO_2	Ti 2p	Ti_{eq}-(N_{int}-O)	-0.43	-0.24
			Ti_{ax}-(N_{int}-O)	-0.18	-0.13
	pure-TiO_2	O 1s	O-N_{int}	2.99	2.70
	N_{int}	N 1s	N_2	0.10	
N_{int}-TiO_2	N_{subs}-TiO_2	N 1s	N_{int}	1.96	2.51
$[Ov\text{-}TiO_2]^{2+}$	pure-TiO_2	Ti 2p	Ti_{eq}-Ov	-0.47	-0.03
			Ti_{ax}-Ov	-0.34	-0.02
	pure-TiO_2	O 1s	O(1)-Ov	-0.45	0.58
			O(2)-Ov	0.66	0.10
Ti_{int}-TiO_2	pure-TiO_2	Ti 2p	Ti_{int}	-1.85	-1.10
			Ti(1)-Ti_{int}	-0.78	-0.20
	pure-TiO_2	O 1s	O(1)-Ti_{int}	0.50	0.09
			O(2)-Ti_{int}	0.61	0.42

ported by different groups [58, 59, 62, 64, 84, 85, 86, 87]. Several new features have been observed in the O 1s, N 1s and Ti 2p XPS spectra of N-doped anatase. It has been found that the set of new features depends on the chemical or physical

method used to dope the anatase. Figure 5.13 shows all the features observed in the O 1s, N 1s and Ti 2p XPS spectra. The experimental O 1s and Ti 2p CLBE peaks for pristine anatase appear at 530.0 and 459.0 eV, respectively. In N-doped anatase it has been measured a small shift towards lower binding energies for the Ti 2p core level (-0.8 eV), for which we compute a shift (whether for interstitial or substitutional nitrogen) of -0.32 eV and -0.35 eV with the initial and ΔSCF approximation, respectively.

For the same system, a new feature (a shoulder) appearing at higher energies in

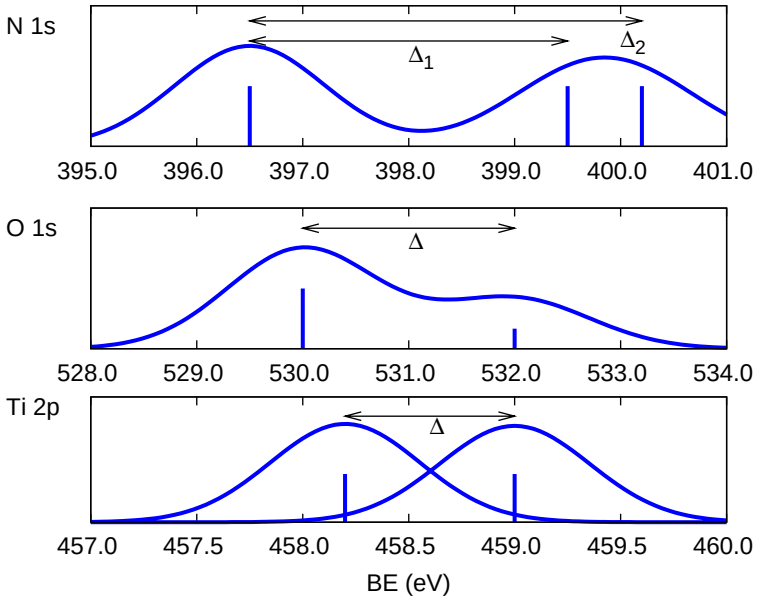

Figure 5.13: Experimental binding energies for the N 1s, O 1s and Ti 2p core levels of N-doped anatase. The blue bars indicate the position of the core level binding energies observed experimentally for the different species. Gaussian functions are used to simulate the N 1s, O 1s and 2p Ti XPS signals. The theoretical FWHM (the full at half maximum) used are 1.17, 1.67 and 1.17 eV for 2p Ti, O 1s and N 1s.

the O 1s XPS signal (about 532.0 eV) have been measured (see Fig. 5.13). The relative position of this feature with respect to the O 1s peak for pristine anatase is in good agreement with our calculated O 1s CLBE shift for the case of having interstitial nitrogen, which is of +3.0 eV (or +2.70 eV) using the initial (or Δ)

approximation. The theoretical O 1s CLBE shift for substitutional nitrogen is small and negative (-0.15 eV), which could result in a overlap of the experimental XPS characteristic of this impurity with the O 1s peak of pristine anatase. Since the theoretical O 1s CLBE shift for interstitial nitrogen is clearly larger than the shifts for the oxygen vacancies and interstitial titanium, the new feature in the O 1s signal can be assigned to the presence of interstitial nitrogen in the sample. it would be great if the sample in those experiments were grown under oxygen-rich conditions. Finally, three new features have been observed in the N 1s XPS signal. They have been measured at about 396.5, 399.5 and 400.2 eV. If we take the lowest binding energy as reference, the relative position of the other ones are +3.0 (399.5 eV) and +3.7 eV (400.2 eV). Our results for the N 1s CLBE shifts for the interstitial nitrogen and isolated molecular nitrogen, taking the substitutional nitrogen as reference, are +1.96 and +2.06 eV, respectively, with the initial state approximation. Our computed shift for the interstitial nitrogen is larger than the value obtained by Selloni et al. [59] (+1.6 eV) using the same approximation. In the ΔSCF approximation the shift between the interstitial and substitutional nitrogen with the latter as reference is of +2.51 eV. Our theoretical result for the shift of the interstitial nitrogen relative to the substitutional one is comparable to the experimental shift between the peak with the lowest binding energy and the peak appearing at 399.5 eV. Therefore we can assign the feature with lowest binding energy to the formation of substitutional nitrogen and the other one having a binding energy of 399.5 eV to the presence of interstitial nitrogen. The peak with the highest binding energy observed experimentally is +0.7 eV from the peak assigned to interstitial nitrogen. This shift is larger than the theoretical shift for the isolated molecular nitrogen with respect to the interstitial nitrogen (+0.1 eV). However, our result suggests that the feature of isolated molecular nitrogen should appear at higher binding energies.

We can conclude that our theoretical CLBE shifts describes in good agreement the XPS experimental data of N-doped anatase and therefore these results can contribute to the full characterization of the nitrogen impurities, and to the understanding of the role that these impurities could play in the enhancement of the photocatalytic activity of anatase.

Chapter 6

Conclusions

We have introduced and implemented two ab initio methods for the study of electronic excitations in molecules and extended solids: the GW approximation and the constrained density functional theory (CDFT). These methods were implemented in the SIESTA code within the strictly localized basis formalism, opening the possibility of studying systems containing thousands of atoms.
We coded the GW approximation following the approach proposed by F. Giustino et al. [3], initially implemented with plane waves, that only requires the Kohn-Sham occupied electronic states to compute both the screened Coulomb potential and the one-particle Green function. The screened Coulomb potential is evaluated using the self-consistent Sternheimer equation and the one-particle Green function is calculated through an inhomogeneous linear system. To do this we first rewrote carefully the set of equations of this approach within the local basis formalism as used in SIESTA, obtaining expressions that use only two-center integrals. Using local basis sets the GW approach scales as $O(N^3)$ (where N is the number of atoms in the system), which is smaller in comparison to plane waves, where this approach scales as $O(N^4)$. Hence, the GW approach with local bases would allow the study of larger and more complex systems than possible with plane waves. The dielectric screening of extended systems, including silicon, diamond, LiCl and Germanium, from the screened Coulomb potential evaluated through the self-consistent Sternheimer equation with local bases, was investigated, comparing our results with plane waves calculations. The use of our method does not require the explicit inversion of the dielectric matrix. We found

that performing an efficient optimization of the local basis we can obtain an accuracy comparable to that of plane waves calculations. This accuracy as well as the monotonic convergence with basis size are very encouraging in view of more efficient excited-state calculations requiring the evaluation of the dielectric matrices. Evaluating the one-particle Green function using either the occupied electronic states only, with the inhomogeneous linear system, or all the electronic states always gives the same results, proving that the Green function is calculated correctly because both procedures are totally equivalent. The maxima of the peaks of the spectral function of the Green function for a particle system obeying the Kohn-Sham Hamiltonian, appear at the Kohn-Sham eigenvalues, also indicating that the Green function is well computed. As the final step in the implementation of the GW approximation in SIESTA, we are now coding the subroutine to evaluate the self-energy operator and quasiparticle excitation energies, and initializing the parallelization of the code.

Our modified version of the CDFT approach proposed by Q. Wu and T. Van Voorhis based on maximizing the energy functional W to efficiently find the potential that gives the constrained state, was successfully implemented in SIESTA with the Mulliken and Löwdin schemes to define the weight function, and extended to periodic solids with the Mulliken scheme. Our CDFT method does not require more complexity than standard DFT, when the potential V_c that gives the constrained state is found efficiently. This allows us the study of electronic excitations in large systems with a low computational cost. In our implementation we perform the maximization of the energy functional $W(V_c)$ to find the constraining potential following a procedure that is different to that used by Q. Wu and T. Van Voorhis, but that is fully theoretically justified. We use two loops to find the constraining potential efficiently. An inner loop is used to solve the constrained Kohn-Sham Hamiltonian self-consistently, while an outer loop is used to perform the maximization of the energy functional $W(V_c)$. Q. Wu and T. Van Voorhis perform the maximization in each step of self consistency of the constrained Kohn-Sham Hamiltonian, not using the correct solution of the constrained Hamiltonian to evaluate the first derivatives of the energy functional $W(V_c)$. The number of steps required to compute the self-consistency of the constrained Hamiltonian using our implementation is similar to that required in a standard DFT calculation

and to perform the maximization the number of steps needed is too small (usually four steps). We applied our implementation to the study of the charge transfer between the TTF and TCNQ molecules in TTF-TCNQ one-dimensional conductor. We found that imposing the constraint through the atomic orbitals of the TTF and TCNQ molecules, using the Mulliken population schemes, do not lead to a direct charge transfer between the lowest occupied and highest unoccupied band associated to the TTF and TCNQ molecules, respectively, likely due to a rehybridization of all the bands of the system. Hence, other approaches to define the constraint domain should be explored. In this line, we believe that imposing the constraint through the molecular orbitals of the highest unoccupied and lowest occupied band is a better model to describe the charge transfer between the TTF and TCNQ molecules. However, this idea will be studied in the future.

Our implemented methods can be use to rationalize and understand the electronic processes that take place in the solar cells and photovoltaic devices based on semiconductor materials for the efficient design of such devices. The most extensively used material in the fabrication of these devices is the TiO_2 anatase whether doped with nitrogen impurities or sensitized with dye molecules adsorbed on its surface. We investigated the electronic, structural, thermodynamic and vibrational properties and core level binding energies shift of TiO_2 anatase with charged point defects, including native defects and nitrogen impurities, using the DFT method. In the characterization of the point defects in the anatase matrix, we determined the most easily formed charge states of the point defects in the allowed electronic chemical potential and found that for the native defects the oxygen vacancy +2 and interstitial titanium +4 have the lowest formation energies. The charge state with the lowest formation energy for the substitutional nitrogen were -1, 0 and +1, while for the interstitial nitrogen, the charge state -1 and +3 were the most easily formed. Of all these defects only the interstitial nitrogen charged whether +3 or -1 change considerably the structural configuration of its neighbouring atoms. New electronic states appear above the valence band edge of the anatase for the interstitial and substitutional nitrogen, while for the oxygen vacancy and interstitial titanium new electronic states appear below the conduction band edge. These electronic state are empty or fully occupied depending on the charge state of the system. We investigated the effect of the

most easily formed point defects on the degenerate $E_g(1)$ Raman active phonon mode of the pristine anatase and found that oxygen vacancy makes $E_g(1)$ shift towards lower frequency (-5.0 cm^{-1}), while the interstitial titanium shifts the $E_g(1)$ mode to higher frequencies (+17.8 cm^{-1}). Similarly to the oxygen vacancies, for interstitial nitrogen we observed a shift towards lower frequencies, but the magnitude of the shift is larger (of about -29 cm^{-1}). For the substitutional nitrogen we observed that the degenerate $E_g(1)$ modes shift in opposite directions, however, the shift to higher frequencies is larger than the one to lower frequencies, and is closer to the shift observed experimentally in N-doped anatase samples, particularly in the charge states -1 and +1. New vibrational features showing a stretching symmetry associated to the interstitial and substitutional nitrogen were found, however, their theoretical IR intensities are too small to be detected experimentally. Our CLBE shift results show that both the initial and ΔSCF approximation give similar shift values, not only in the order of magnitude of the shifts but also in their direction. According to our CLBE shift results it is be possible to distinguish between interstitial and substitutional nitrogen from their N 1s and O 1s XPS signals. The N 1s binding energies of the interstitial nitrogen and molecular nitrogen are at higher energies (1.96 and 2.06 eV, respectively, within the initial approximation) relative to the position of the binding energy associated to substitutional nitrogen, and a new feature appear at +2.70 eV from the O 1s binding energy of the pristine anatase for interstitial nitrogen only. Comparing our results with experimental data we found that our results describe satisfactorily the shifts observed experimentally in the N 1s, O 1s and Ti 2p XPS signals of N-doped anatase. Hence, we assign the peak observed at 396.5 eV to substitutional nitrogen, while the peaks observed at higher energies can be assigned whether interstitial nitrogen or molecular nitrogen physically adsorbed on the surface of the sample. The shoulder observed in the O 1s signal is assigned to the presence of interstitial nitrogen in the sample.

References

[1] José M Soler, Emilio Artacho, Julian D Gale, Alberto García, Javier Junquera, Pablo Ordejón, and Daniel Sánchez-Portal. The SIESTA method for ab initio order- n materials simulation. *Journal of Physics: Condensed Matter*, 14(11):2745–2779, March 2002. v, 13, 14, 15, 17

[2] Pablo Ordejón, Emilio Artacho, and José M. Soler. Self-consistent order-n density-functional calculations for very large systems. *Physical Review B*, 53(16):R10441–R10444, April 1996. v

[3] Feliciano Giustino, Marvin L. Cohen, and Steven G. Louie. GW method with the self-consistent sternheimer equation. *Physical Review B*, 81(11):115105, March 2010. iii, v, 4, 26, 39, 139

[4] Qin Wu and Troy Van Voorhis. Direct optimization method to study constrained systems within density-functional theory. *Physical Review A*, 72(2), August 2005. iii, vi, 3, 71, 86

[5] Qin Wu and Troy Van Voorhis. Constrained density functional theory and its application in long-range electron transfer. *Journal of Chemical Theory and Computation*, 2(3):765–774, May 2006. vi, xiii, 3, 71, 74, 86, 87, 91

[6] Benjamin Kaduk, Tim Kowalczyk, and Troy Van Voorhis. Constrained density functional theory. *Chemical Reviews*, 112(1):321–370, January 2012. vi, 71

[7] J. Fraxedas, Y. J. Lee, I. Jiménez, R. Gago, R. M. Nieminen, P. Ordejón, and E. Canadell. Characterization of the unoccupied and partially occupied

states of TTF-TCNQ by XANES and first-principles calculations. *Physical Review B*, 68(19):195115, November 2003. vi, 95

[8] M. Sing, U. Schwingenschlgl, R. Claessen, M. Dressel, and C. S. Jacobsen. Surface characterization and surface electronic structure of organic quasi-one-dimensional charge transfer salts. *Physical Review B*, 67(12):125402, March 2003. vi, 95

[9] Michael Grätzel. Applied physics: Solar cells to dye for. *Nature*, 421(6923):586–587, February 2003. vi, 106

[10] Michael Grätzel. Photoelectrochemical cells. *Nature*, 414(6861):338–344, November 2001. vi, 106

[11] Monica Lira-Cantu and Frederik C. Krebs. Hybrid solar cells based on MEH-PPV and thin film semiconductor oxides (TiO2, Nb2O5, ZnO, CeO2 and CeO2TiO2): performance improvement during long-time irradiation. *Solar Energy Materials and Solar Cells*, 90(14):2076–2086, September 2006. vi, 106

[12] Fabien Tran and Peter Blaha. Accurate band gaps of semiconductors and insulators with a semilocal exchange-correlation potential. *Physical Review Letters*, 102(22):226401, June 2009. ix, 2

[13] Levine. *Quantum Chemistry 6th (sixth) edition BYLevine*. Prentice Hall;, 6th (sixth) edition edition, 2008. 1

[14] J. F. Janak. Proof that E/n_i= in density-functional theory. *Physical Review B*, 18(12):7165–7168, December 1978. 1, 28

[15] Irmgard Frank, Jürg Hutter, Dominik Marx, and Michele Parrinello. Molecular dynamics in low-spin excited states. *The Journal of Chemical Physics*, 108(10):4060–4069, March 1998. 1

[16] Erich Runge and E. K. U. Gross. Density-functional theory for time-dependent systems. *Physical Review Letters*, 52(12):997–1000, March 1984. 2

[17] Andreas Dreuw and Martin Head-Gordon. Failure of time-dependent density functional theory for long-range charge-transfer excited states: The Zincbacteriochlorin–Bacteriochlorin and Bacteriochlorophyll–Spheroidene complexes. *Journal of the American Chemical Society*, 126(12):4007–4016, March 2004. 3, 70

[18] Lars Hedin. New method for calculating the One-Particle green's function with application to the Electron-Gas problem. *Physical Review*, 139(3A):A796–A823, 1965. 4, 28, 35

[19] Mark S. Hybertsen and Steven G. Louie. Electron correlation in semiconductors and insulators: Band gaps and quasiparticle energies. *Physical Review B*, 34(8):5390–5413, October 1986. 4, 28, 37

[20] Richard M. Martin. *Electronic Structure: Basic Theory and Practical Methods*. Cambridge University Press, 1 edition, October 2008. 7, 10, 17

[21] J. C. Slater. Note on hartree's method. *Physical Review*, 35(2):210–211, January 1930. 9

[22] S. F. Boys. Electronic wave functions. i. a general method of calculation for the stationary states of any molecular system. *Proceedings of the Royal Society of London. Series A. Mathematical and Physical Sciences*, 200(1063):542–554, February 1950. 9

[23] J. C. Slater. A simplification of the Hartree-Fock method. *Physical Review*, 81(3):385–390, February 1951. 9

[24] J. C. Slater. Magnetic effects and the Hartree-Fock equation. *Physical Review*, 82(4):538–541, May 1951. 9

[25] P. Hohenberg and W. Kohn. Inhomogeneous electron gas. *Physical Review*, 136(3B):B864–B871, November 1964. 9

[26] W. Kohn. Nobel lecture: Electronic structure of matterwave functions and density functionals. *Reviews of Modern Physics*, 71(5):1253–1266, October 1999. 9

[27] W. Kohn and L. J. Sham. Self-Consistent equations including exchange and correlation effects. *Physical Review*, 140(4A):A1133–A1138, November 1965. 10

[28] John P. Perdew, Kieron Burke, and Yue Wang. Generalized gradient approximation for the exchange-correlation hole of a many-electron system. *Physical Review B*, 54(23):16533–16539, December 1996. 12

[29] John P. Perdew, Kieron Burke, and Matthias Ernzerhof. Generalized gradient approximation made simple. *Physical Review Letters*, 77(18):3865–3868, October 1996. 12

[30] Eduardo Anglada, José M. Soler, Javier Junquera, and Emilio Artacho. Systematic generation of finite-range atomic basis sets for linear-scaling calculations. *Physical Review B*, 66(20):205101, November 2002. 14, 111

[31] J. Junquera, O. Paz, D. Sánchez-Portal, and E. Artacho. Numerical atomic orbitals for linear-scaling calculations. *Physical Review B*, 64(23):235111, November 2001. 14, 15

[32] E. Artacho, D. Sánchez-Portal, P. Ordejón, A. García, and J. M. Soler. Linear-scaling ab-initio calculations for large and complex systems. *physica status solidi (b)*, 215(1):809817, 1999. 14

[33] Otto F. Sankey and David J. Niklewski. Ab initio multicenter tight-binding model for molecular-dynamics simulations and other applications in covalent systems. *Physical Review B*, 40(6):3979–3995, 1989. 15

[34] D. R. Hamann, M. Schlüter, and C. Chiang. Norm-Conserving pseudopotentials. *Physical Review Letters*, 43(20):1494–1497, November 1979. 16

[35] N. Troullier and José Luriaas Martins. Efficient pseudopotentials for plane-wave calculations. *Physical Review B*, 43(3):1993–2006, January 1991. 17

[36] Leonard Kleinman and D. M. Bylander. Efficacious form for model pseudopotentials. *Physical Review Letters*, 48(20):1425–1428, May 1982. 17

[37] P. Pulay. Improved SCF convergence acceleration. *Journal of Computational Chemistry*, 3(4):556560, 1982. 18

[38] Péter Pulay. Convergence acceleration of iterative sequences. the case of scf iteration. *Chemical Physics Letters*, 73(2):393–398, July 1980. 18

[39] S. García-Gil, A. García, and P. Ordejón. Calculation of core level shifts within DFT using pseudopotentials and localized basis sets. *The European Physical Journal B*, 85(7), July 2012. 20, 24

[40] E. Pehlke and M. Scheffler. Evidence for site-sensitive screening of core holes at the si and ge (001) surface. *Physical Review Letters*, 71(14):2338–2341, October 1993. 21

[41] D. Foerster, P. Koval, and D. Sánchez-Portal. An O(N3) implementation of hedin's GW approximation for molecules. *The Journal of Chemical Physics*, 135(7):074105–074105–15, August 2011. 26

[42] Giovanni Onida, Lucia Reining, and Angel Rubio. Electronic excitations: density-functional versus many-body greens-function approaches. *Reviews of Modern Physics*, 74(2):601–659, June 2002. 26

[43] Giovanni Onida, Lucia Reining, R. W. Godby, R. Del Sole, and Wanda Andreoni. Ab initio calculations of the quasiparticle and absorption spectra of clusters: The sodium tetramer. *Physical Review Letters*, 75(5):818–821, July 1995. 26

[44] Michael Rohlfing and Steven G. Louie. Electron-hole excitations in semiconductors and insulators. *Physical Review Letters*, 81(11):2312–2315, September 1998. 26

[45] F Aryasetiawan and O Gunnarsson. The GW method. *Reports on Progress in Physics*, 61(3):237–312, March 1998. 28

[46] J. Hubbard. Electron correlations in narrow energy bands. *Proceedings of the Royal Society of London. Series A. Mathematical and Physical Sciences*, 276(1365):238–257, November 1963. 35

[47] X. Blase, C. Attaccalite, and V. Olevano. First-principles GW calculations for fullerenes, porphyrins, phtalocyanine, and other molecules of interest for organic photovoltaic applications. *Physical Review B*, 83(11):115103, March 2011. 39

[48] Michael Rohlfing, Peter Krger, and Johannes Pollmann. Quasiparticle band-structure calculations for c, si, ge, GaAs, and SiC using gaussian-orbital basis sets. *Physical Review B*, 48(24):17791–17805, December 1993. 39

[49] P. Umari, Geoffrey Stenuit, and Stefano Baroni. GW quasiparticle spectra from occupied states only. *Physical Review B*, 81(11):115104, March 2010. 39

[50] X. Gonze, B. Amadon, P.-M. Anglade, J.-M. Beuken, F. Bottin, P. Boulanger, F. Bruneval, D. Caliste, R. Caracas, M. Coté, T. Deutsch, L. Genovese, Ph. Ghosez, M. Giantomassi, S. Goedecker, D.R. Hamann, P. Hermet, F. Jollet, G. Jomard, S. Leroux, M. Mancini, S. Mazevet, M.J.T. Oliveira, G. Onida, Y. Pouillon, T. Rangel, G.-M. Rignanese, D. Sangalli, R. Shaltaf, M. Torrent, M.J. Verstraete, G. Zerah, and J.W. Zwanziger. ABINIT: first-principles approach to material and nanosystem properties. *Computer Physics Communications*, 180(12):2582–2615, December 2009. 52

[51] Andrea Marini, Conor Hogan, Myrta Grning, and Daniele Varsano. yambo: An ab initio tool for excited state calculations. *Computer Physics Communications*, 180(8):1392–1403, August 2009. 52

[52] Stephen L. Adler. Quantum theory of the dielectric constant in real solids. *Physical Review*, 126(2):413–420, April 1962. 52

[53] Nathan Wiser. Dielectric constant with local field effects included. *Physical Review*, 129(1):62–69, January 1963. 52

[54] Arno Schindlmayr. Decay properties of the one-particle green function in real space and imaginary time. *Physical Review B*, 62(19):12573–12576, November 2000. 68

[55] G. Makov and M. C. Payne. Periodic boundary conditions in ab initio calculations. *Physical Review B*, 51(7):4014–4022, February 1995. 92

[56] Deanna C. Hurum, Alexander G. Agrios, Kimberly A. Gray, Tijana Rajh, and Marion C. Thurnauer. Explaining the enhanced photocatalytic activity of degussa p25 Mixed-Phase TiO2 using EPR. *J. Phys. Chem. B*, 107(19):4545–4549, 2003. 106, 121

[57] Wonyong Choi, Andreas Termin, and Michael R. Hoffmann. The role of metal ion dopants in Quantum-Sized TiO2: correlation between photoreactivity and charge carrier recombination dynamics. *J. Phys. Chem.*, 98(51):13669–13679, 1994. 106

[58] R. Asahi, T. Morikawa, T. Ohwaki, K. Aoki, and Y. Taga. Visible-Light photocatalysis in Nitrogen-Doped titanium oxides. *Science*, 293(5528):269–271, July 2001. 106, 107, 108, 136

[59] Cristiana Di Valentin, Emanuele Finazzi, Gianfranco Pacchioni, Annabella Selloni, Stefano Livraghi, Maria Cristina Paganini, and Elio Giamello. N-doped TiO2: theory and experiment. *Chemical Physics*, 339(13):44–56, October 2007. 106, 107, 108, 112, 115, 121, 127, 128, 136, 138

[60] J. B. Varley, A. Janotti, and C. G. Van de Walle. Mechanism of Visible-Light photocatalysis in Nitrogen-Doped TiO2. *Advanced Materials*, 23(20):23432347, 2011. 106, 108

[61] Zheshuai Lin, Alexander Orlov, Richard M. Lambert, and Michael C. Payne. New insights into the origin of visible light photocatalytic activity of Nitrogen-Doped and Oxygen-Deficient anatase TiO2. *J. Phys. Chem. B*, 109(44):20948–20952, 2005. 107, 108

[62] Ye Cong, Jinlong Zhang, Feng Chen, and Masakazu Anpo. Synthesis and characterization of Nitrogen-Doped TiO2 nanophotocatalyst with high visible light activity. *J. Phys. Chem. C*, 111(19):6976–6982, 2007. 107, 108, 136

[63] Hsin-Hsi Lo, Neeruganti O. Gopal, and Shyue-Chu Ke. Origin of photoactivity of oxygen-deficient TiO2 under visible light. *Applied Physics Letters*, 95(8):083126–083126–3, August 2009. 107

[64] Shanmugasundaram Sakthivel, Marcin Janczarek, and Horst Kisch. Visible light activity and photoelectrochemical properties of Nitrogen-Doped TiO2. *J. Phys. Chem. B*, 108(50):19384–19387, 2004. 107, 136

[65] Lan Mi, Yu Zhang, and Pei-Nan Wang. First-principles study of the hydrogen doping influence on the geometric and electronic structures of n-doped TiO2. *Chemical Physics Letters*, 458(46):341–345, June 2008. 107

[66] T. Berger, M. Sterrer, O. Diwald, E. Knözinger, D. Panayotov, T. L. Thompson, and J. T. Yates. Light-Induced charge separation in anatase TiO2 particles. *J. Phys. Chem. B*, 109(13):6061–6068, 2005. 107

[67] Oliver Diwald, Tracy L. Thompson, Ed G. Goralski, Scott D. Walck, and John T. Yates. The effect of nitrogen ion implantation on the photoactivity of TiO2 rutile single crystals. *J. Phys. Chem. B*, 108(1):52–57, 2003. 107, 121

[68] Shinri Sato, Ryuhei Nakamura, and Shinji Abe. Visible-light sensitization of TiO2 photocatalysts by wet-method n doping. *Applied Catalysis A: General*, 284(12):131–137, April 2005. 107

[69] Yoshitaka Nakano, Takeshi Morikawa, Takeshi Ohwaki, and Yasunori Taga. Deep-level optical spectroscopy investigation of n-doped TiO2 films. *Applied Physics Letters*, 86(13):132104–132104–3, March 2005. 107

[70] Kesong Yang, Ying Dai, and Baibiao Huang. Study of the nitrogen concentration influence on N-Doped TiO2 anatase from First-Principles calculations. *J. Phys. Chem. C*, 111(32):12086–12090, 2007. 107, 127

[71] J. C. Parker and R. W. Siegel. Calibration of the raman spectrum to the oxygen stoichiometry of nanophase TiO2. *Applied Physics Letters*, 57(9):943–945, August 1990. 109, 122

[72] J. C. Parker and R. W. Siegel. Raman microprobe study of nanophase TiO2 and oxidation-induced spectral changes. *Journal of Materials Research*, 5(06):1246–1252, 1990. 109, 122

[73] Hendrik J. Monkhorst and James D. Pack. Special points for brillouin-zone integrations. *Physical Review B*, 13(12):5188–5192, June 1976. 112

[74] Masayoshi Mikami, Shinichiro Nakamura, Osamu Kitao, and Hironori Arakawa. Lattice dynamics and dielectric properties of TiO_2 anatase: A first-principles study. *Physical Review B*, 66(15):155213, October 2002. 112, 117, 118

[75] R. J. Gonzalez, R. Zallen, and H. Berger. Infrared reflectivity and lattice fundamentals in anatase TiO_2s. *Physical Review B*, 55(11):7014–7017, March 1997. 112, 117

[76] Keith M. Glassford and James R. Chelikowsky. Structural and electronic properties of titanium dioxide. *Physical Review B*, 46(3):1284–1298, July 1992. 115

[77] Changyol Lee, Philippe Ghosez, and Xavier Gonze. Lattice dynamics and dielectric properties of incipient ferroelectric TiO_2 rutile. *Physical Review B*, 50(18):13379–13387, November 1994. 117

[78] Changyol Lee and Xavier Gonze. Dielectric constants and born effective charges of TiO_2 rutile. *Physical Review B*, 49(20):14730–14731, May 1994. 117

[79] Ph. Ghosez, J.-P. Michenaud, and X. Gonze. Dynamical atomic charges: The case of ABO_3 compounds. *Physical Review B*, 58(10):6224–6240, 1998. 117

[80] Toshiaki Ohsaka, Fujio Izumi, and Yoshinori Fujiki. Raman spectrum of anatase, TiO2. *Journal of Raman Spectroscopy*, 7(6):321324, 1978. 118

[81] J. N. Krishnamurthy and T. M. Haridasan. Lattice vibrations in the anatase phase of titanium dioxide. *Indian J. Pure Appl. Phys.*, 17:67–72, 1979. 118

[82] Cristiana Di Valentin, Gianfranco Pacchioni, and Annabella Selloni. Origin of the different photoactivity of n-doped anatase and rutile TiO_2. *Physical Review B*, 70(8):085116, 2004. 121

[83] I. Justicia, P. Ordejón, G. Canto, J.l. Mozos, J. Fraxedas, G.a. Battiston, R. Gerbasi, and A. Figueras. Designed Self-Doped titanium oxide thin films for efficient Visible-Light photocatalysis. *Advanced Materials*, 14(19):13991402, 2002. 121

[84] E. György, A. Pérez del Pino, P. Serra, and J.L. Morenza. Depth profiling characterisation of the surface layer obtained by pulsed Nd:YAG laser irradiation of titanium in nitrogen. *Surface and Coatings Technology*, 173(23):265–270, August 2003. 136

[85] Xiaobo Chen and Clemens Burda. Photoelectron spectroscopic investigation of Nitrogen-Doped titania nanoparticles. *J. Phys. Chem. B*, 108(40):15446–15449, 2004. 136

[86] M. Sathish, B. Viswanathan, R. P. Viswanath, and Chinnakonda S. Gopinath. Synthesis, characterization, electronic structure, and photocatalytic activity of nitrogen-doped TiO2 nanocatalyst. *Chemistry of Materials*, 17(25):6349–6353, December 2005. 136

[87] Di Li, Hajime Haneda, Shunichi Hishita, and Naoki Ohashi. Visible-light-driven NFCodoped TiO2 photocatalysts. 2. optical characterization, photocatalysis, and potential application to air purification. *Chemistry of Materials*, 17(10):2596–2602, May 2005. 136